UNIVERSITY OF CALIFORNIA
RIVERSIDE

Low-Frequency Noise Spectroscopy of Advanced Electronic Materials and Devices

A Dissertation submitted in partial satisfaction
of the requirements for the degree of

Doctor of Philosophy

in

Electrical Engineering

by

Subhajit Ghosh

December 2022

Dissertation Committee:
        Dr. Alexander A. Balandin, Chairperson
        Dr. Roger Lake
        Dr. Fariborz Kargar

The Dissertation of Subhajit Ghosh is approved:

_____

_____

_____
                                    Committee Chairperson

University of California, Riverside

Acknowledgments

I would like to start by thanking my doctoral advisor, Prof. Alexander A. Balandin for allowing me to conduct state-of-the-art research under his supervision. I have spent the best 4 years of my life in his research group at UC Riverside and have been able to use my creative mind to the best of my ability. His sincere guidance has helped me to survive and thrive as a researcher in a highly competitive research field like "Electronic Materials and Devices". I would be indebted to him for the rest of my life for shaping my career in a way I never imagined I would be able to achieve. Lastly, let me take this opportunity to show my sincere gratitude to him for financially supporting me during my graduate studies.

I would also like to thank Prof. Fariborz Kargar, Assistant adjunct professor at UC Riverside and the manager of our research center. Prof. Kargar has been extremely helpful during my research, and, without his sincere guidance, it would have been impossible for me to complete my research on time. Another person who was instrumental in helping me to do reliable data analysis of my projects was Prof. Sergey Rumyantsev from the Institute of High-Pressure Physics of the Polish Academy of Sciences, Warsaw. I learned a lot from him about "electronic noise", which has been the core of my dissertation research.

Let me also take this space to thank Prof. Roger Lake from UC Riverside who was kind enough to agree to serve as a committee member for my dissertation defense. I took four

of his courses at the early stage of my doctoral studies and learned a lot from his lectures, which eventually solved a lot of the theoretical riddles in my research projects.

I have been fortunate to be able to work on several collaborative projects with research groups from other esteemed US institutes. In this regard, I would like to acknowledge Prof. Yuji Zhao's research group from Rice University, where the GaN PIN diodes were fabricated for one of my dissertation projects; Prof. Robert Nemanich from Arizona State University, who provided us with Diamond diodes for noise reliability tests; and Prof. Tina T. Salguero's group at University of Georgia, who synthesized the Quasi 1D Weyl semimetal $(TaSe_4)_2I$ bulk crystal for us.

I would like to take the names of two people who helped me a lot in learning device fabrication at UCR cleanroom, Dr. AmirMahdi MohammadZadeh, who was my senior colleague for three years, and Dr. Dong Yang, the manager at UCR cleanroom. Besides, I would like to thank all my ex and present co-workers who helped me at different points in time, namely, Dr. Zahra Barani, Dr. Saba Baraghani, Maedeh, Sriharsha, Dylan, Erick, Jonas, Zahra Jr., Tekwam, and Lokesh.

The acknowledgment section cannot be complete without mentioning the names of my master's thesis advisor, Prof. Zhang Yang, Assistant Professor at the University of Illinois at Chicago, and my senior colleague, Dr. Bo Hsu. My quest to learn the unknown started at that very place.

Lastly, I would like to remember my family, without whom I would not be able to survive a challenging and stressful Ph.D. life.

The text and figures of this dissertation, in part or in full, are a reprint of the material as it appears in the following journals and/or proceedings:

Chapter 2: S. Ghosh, K. Fu, F. Kargar, S. Rumyantsev, Y. Zhao, and A. A. Balandin, "Low-frequency noise characteristics of GaN vertical PIN diodes—Effects of design, current, and temperature", Appl. Phys. Lett., 119, 243505, 202. https://doi.org/10.1063/5.0075498. Reprinted with permission, Copyright © 2021 AIP Publishing.

Chapter 3: S. Ghosh, H. Surdi, F. Kargar, F. Koeck, S. Rumyantsev, S. Goodnick, R. J. Nemanich, and A. A. Balandin, "Excess noise in high-current diamond diodes", Appl. Phys. Lett., 120, 062103, 2022. https://doi.org/10.1063/5.0083383. Reprinted with permission, Copyright © 2022 AIP Publishing.

Chapter 4: S. Ghosh, F. Kargar, A. Mohammadzadeh, S. Rumyantsev, and A. A. Balandin, "Low-frequency electronic noise spectroscopy of quasi-2D van der Waals antiferromagnetic semiconductors," Adv. Electron. Mater., 2100408, 2021. https://doi.org/10.1002/aelm.202100408. Reprinted with permission, Copyright © 2021, Wiley-VCH GmbH.

ABSTRACT OF THE DISSERTATION

Low-Frequency Noise Spectroscopy of Advanced Electronic Materials and Devices

by

Subhajit Ghosh

Doctor of Philosophy, Graduate Program in Electrical Engineering
University of California, Riverside, December 2022
Dr. Alexander A. Balandin, Chairperson

Low-frequency electronic noise, also referred to as excess noise, is present in almost all electronic materials and devices. It is usually desirable to reduce this noise type since it directly contributes to the phase noise of electronic devices and communications systems. However, measurements of the low-frequency noise can also provide valuable information on the material quality and electron transport. In this dissertation research, we developed approaches for electronic noise spectroscopy and applied them to a range of electronic materials and devices, including GaN and diamond high-current diodes, antiferromagnetic semiconductors, and Weyl semimetal nanowires. The excess noise includes the $1/f$ and generation-recombination (G-R) noise with a Lorentzian type spectrum (f is the frequency). The $1/f$ noise can be an early indicator of electromigration damage and provide insight into the nature of reliability-limiting defects in materials and devices. The noise in most of the tested GaN devices had a characteristic $1/f$ spectrum at high and moderate currents, while some devices revealed G-R bulges at low currents. Temperature, current, and frequency

dependences of noise suggest that the noise mechanism in GaN diodes is of recombination origin. We argue that the noise measurements at low currents can be used to efficiently assess the quality of GaN diodes. The G-R bulges are characteristic of diamond diodes with lower turn-on voltages. The characteristic trap time constants, extracted from the noise data, show a uniquely strong dependence on current. The noise spectral density of FePS$_3$ was of the $1/f$-type over most of the examined temperature range but revealed well-defined Lorentzian bulges, and increased strongly near the Néel temperature T_N=118 K. The noise attained its minimum at temperature T~200 K, which was attributed to an interplay of two opposite trends in noise scaling – one for semiconductors and another for materials with phase transitions. The obtained results are important for proposed applications of antiferromagnetic semiconductors in spintronic devices.

Table of Contents

List of Figures

components as function of the applied bias voltage measured at different temperatures. Note the strong dependence of the corner frequency on temperature and bias voltage. Reprinted with permission from S. Ghosh et al., Advanced Electronic Materials. **2021**, 7, 2100408, Copyright © 2021, Wiley-VCH GmbH..................... 64

List of Tables

1. Introduction to the Electronic Noise

1.1 Introduction

Noise is an unwanted signal which can interfere with the true electrical signal (current and voltage) of any electronic system and affect its performance [1-4]. In theory, the DC signal of any electronic system is time-invariant. However, the presence of noise can significantly perturb the DC signal which in turn can fluctuate in its amplitude with time even without any external interference. The nature of such perturbation is random and therefore it is difficult to completely get rid of such noise from any electronic system [1,2]. Electronic noise which originates from external sources such as AC power lines, acoustic and photonic vibrations, and electromagnetic interference can significantly alter the operational quality of the system. However, noise caused by such external factors can be greatly reduced with a proper experimental setup [2]. On the other hand, electronic noise can also be originated internally from any electronic material and device due to random fluctuation in electronic transport phenomena [5-9]. The random nature of such noise originating intrinsically in the system due to perturbation of physical processes can make it difficult to eliminate it. In this chapter, we will discuss such internal electronic noise especially noise in the low-frequency regime ($f \leq 100$ kHz, f is the frequency) called low-frequency noise [8]. Low-frequency noise, present in every electronic and communication system can interfere with the system performance [10-12]. Although mostly present in the lower

frequency regime, such noise can upconvert to phase noise and degrade the performance of high-frequency applications [12]. Therefore, it can limit the operating range of any communication system. However, measurements of the low-frequency noise can also provide valuable information on the material quality and electron transport. Low-frequency noise has been extensively used to study the reliability of electronic devices [13-15]. Besides, it has also been used to study the phase change of materials [16-18].

1.2   Type of Electronic Noise

The intrinsic electronic noise can be categorized into four main types:

1)   Thermal Noise: Thermal noise also named Nyquist or Johnson noise is present in every electronic system. In 1926 John B. Johnson discovered this type of noise at Bell Laboratories and H. Nyquist published the theoretical interpretation of thermal noise after 2 years in 1928 [19]. The origin of such noise is due to the thermal motion of the charge carrier (electron) within an electronic material [8]. Thermal noise is unavoidable as the electron can be thermally excited and its motion becomes random. Consequently, such random motion of electrons can result in a net flow of small current without any external bias owing to the deviation in carrier concentrations between two regions. In the frequency domain, the noise spectral density of thermal noise is independent of the corresponding frequencies and remains constant. For this reason, this type of noise is also called white

noise. The spectral density of thermal noise for any resistance R at a non-zero temperature T can be expressed as [2,8]

$$S_V = 4KTR \text{ or } S_I = {4KT}/{R}$$

Where K = Boltzmann's constant

2)   Shot Noise: Shot noise can originate in any electronic device with a potential barrier (such as semiconductor pn junction diode) due to the discrete nature of charge carriers [20,21]. The electron can pass through the potential barrier randomly. Shot noise was discovered by W. Schottky in 1918 [21]. Like thermal noise, shot noise also shows white noise behavior since its spectral density is frequency independent. The spectral density of shot noise of a charge q flowing through a barrier with average DC current I can be expressed as [2,8]

$$S_I = 2q <I>$$

3)   Generation-Recombination Noise: In semiconductor material band structure, trap states exist in the forbidden gap between valence and conduction bands due to the presence of impurities or defects. The transition of charge carriers (electrons and holes) between valance and conduction bands can be hindered by these trap levels which can capture the charge carriers randomly and then release them. Such random capture and emission by the trap states can give rise to fluctuation in electronic transport in the form of noise. This type of noise is called generation-recombination (GR) noise [22,23]. The fluctuation governing GR noise can emerge due to changes in carrier number, carrier mobility, electric field etc

[22,23]. It is important to note that not all trap levels within the forbidden gap can produce GR noise through random carrier capture-emission. To generate GR type noise, the trap state should be closer to the Fermi level [2]. The power spectral density of GR noise is Lorentzian in shape and can be expressed as [8]:

$$S_I = {S_0}\Big/{[1 + (2\pi f \tau)^2]}$$

Where S_0 = frequency-independent part of the spectral density when $f < (2\pi\tau)^{-1}$ and $\tau =$ the time constant for a specific trap state.

Random telegraph noise (RTS), also known as popcorn or burst noise is a special type of GR noise with similar Lorentzian shape in the frequency spectrum [24,25]. In this type of noise, telegraphic waveforms with randomly oriented pulses can be observed in the time domain. RTS noise can occur if the noise is generated by a few trap states with a similar time constant creating a two-level system with random capture and emission between the states which generate pulses in the transient response [25]. RTS noise can only be distinguished from corresponding GR noise from the time domain response.

4) *1/f* Noise: *1/f* noise which is also popularly known as flicker or excess noise is one of the common types of low-frequency noise which can be found in almost all semiconductor materials and devices [1-10, 26,27]. The *1/f* noise was discovered by J. B. Johnson while he was attempting to experimentally prove the shot noise phenomenon as theorized by W. Schottky [26]. Unlike shot noise, the observed noise in his experiment was not frequency-

independent white noise. The spectral density of *1/f* noise follows the equation [8]

$$S_I(f) \sim 1/f^\gamma \qquad \text{Where } \gamma \approx 1$$

The *1/f* noise spectra in the lower frequency regime follow the power law (power inversely proportional to the x-axis). Thus, *1/f* noise is also called pink noise. *1/f* type power spectra have been observed in many diverse fields such as physics, biology, economics, geology etc.

The origin of *1/f* type noise in semiconductor materials and devices is still a debatable topic with many theories trying to explain the possible noise origin [28]. In general, the current (*I*) in an electronic system can be expressed as [4,5]:

$$I = qN\mu \text{ where } N = \text{no of carriers and } \mu = \text{carrier mobility}$$

Therefore, current fluctuations (*ΔI*) can be written as:

$$\Delta I = q(\Delta N)\mu + qN(\Delta\mu)$$

Therefore, the current fluctuation can be described either by the carrier no fluctuations or carrier mobility fluctuations. One theory for the possible origin of *1/f* noise is explained as the consequence of carrier fluctuations. In this case, *1/f* noise is generated when a large no of trap levels with distinct time constants creates individual GR type Lorentzian spectrum which superimposes together to create a *1/f* envelope over a range of frequencies. The distribution of trap level time constants can be explained as [2]:

$$g(\tau) = {1}\Big/{\ln\left(\frac{\tau_2}{\tau_1}\right)\tau} \text{ when } \tau_1 < \tau < \tau_2 \text{ and } g(\tau) = 0 \text{ otherwise.}$$

Here, the spectral density becomes,

$$S_I \approx {B}\Big/{4\ln\left(\frac{\tau_2}{\tau_1}\right)f} \text{ when } 1/2\pi\tau_1 \ll f \ll 1/2\pi\tau_1$$
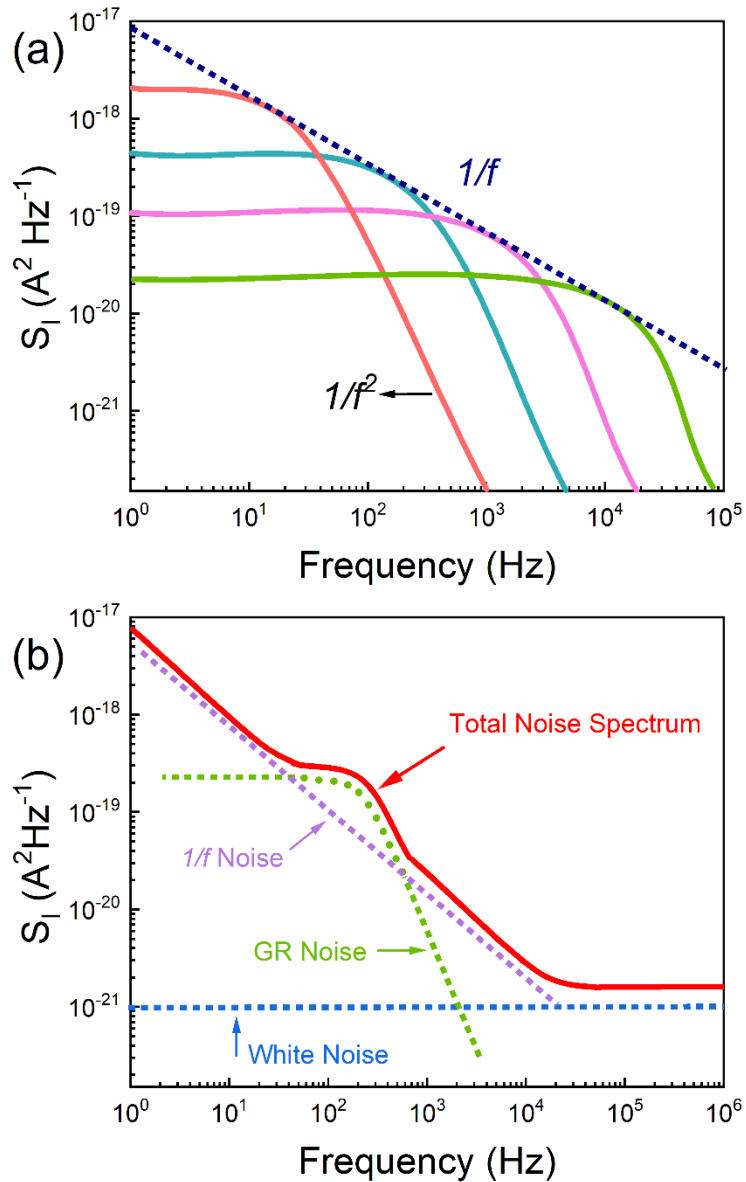
Figure 1-1: Schematics representation of electronic noise. (a) The power spectral density of 4 Lorentzian-shaped generation-recombination (GR) noise with varying time constants. The tale of each Lorentzian curve follows *1/f²* dependence. The superposition of the GR noise spectra creates *1/f* type noise at the frequency ranges. (b) The power spectral density of a typical noise spectrum consists of low-frequency noise (*1/f* noise, GR noise) and white noise (thermal noise) floor at higher frequencies.

The superposition of the GR noise spectrum of several distinct trap levels as the origin of *1/f* noise was explained by McWhorther's model for field effect transistor (FET) [29]. Another established empirical model to explain the origin of *1/f* noise was created by Hooge from the notion of mobility fluctuation [5]. Hooge's formula is as follows

$$\frac{S_R}{R^2} = \frac{\alpha_H}{fN}$$

Where α_H = Hooge parameter and $\dfrac{S_R}{R^2} = \dfrac{S_I}{I^2} = \dfrac{S_V}{V^2}$

The schematic representations of different types of electronic noises are shown in Figures 1-1.

1.3   The Home-Built Noise Measurement System

Owning to its high sensitivity, the low-frequency noise measurements were conducted inside a specially designed laboratory room to avoid any potential external interference (such as electromagnetic interference, acoustic vibrations etc.). The noise measurements were done by using a home-built noise system consisting of separate instruments such as DC batteries, a low-noise preamplifier (SR 560), a dynamic signal analyzer (Photon+ Bruel and Kjaer), and a semiconductor analyzer (Agilent B1500) for additional electrical testing. The device under test (DUT) was kept inside a cryogenic probe station (Lakeshore TTPX) which shielded the DUT from any additional electromagnetic (EM) radiation from the outside environment. The DUT inside the cryogenic probe station was connected in a two-

terminal (2T) configuration and the probe station stage was used to control the temperature of the DUT (between 77 K -475 K) as required.

The noise measurement circuit resembles a typical voltage divider circuit consisting of two resistors (a load resistor and the DUT) (refer to Figure 1-2). An additional potentiometer (POT) was connected to the DC battery source to control the voltage drop across the circuit. The resistance of the POT was selected to be at least several orders lower than the DUT. On the other hand, the load resistor was picked up having comparable resistance to the DUT in general. However, for very high resistive DUT noise measurements, the R_L values were kept under 50 KΩ. In our noise circuit, either the DUT or the load resistor was grounded depending upon the nature of the noise measurements. In the case of the circuit biasing, the DC batteries were used instead of any DC power supply to reduce the 60 Hz AC signal and its harmonics. The AC signal interference was further reduced by disconnecting the other instruments (preamplifier, signal analyzer etc.) from the AC power line at the time of noise studies. During the noise measurements, the POT controlled the voltage drop across the load resistor (R_L) and the DUT (R_D) and the output voltage fluctuations of the circuit were transferred to the low-noise preamplifier (SR 560). The amplified signal was then sent to the dynamic signal analyzer. The signal analyzer connected to a computer converted the time domain voltage response to its corresponding frequency domain response using Fourier transform. The amplified transient response (V vs T) of the output and its corresponding frequency (f) response in the form of voltage spectral density (S_V) were displayed simultaneously on a graphical user interface (GUI) on

the computer screen. The obtained voltage spectral density (S_V) was then converted to its

corresponding current spectral density (S_I) by using the equation below:

$$S_I = S_V \times [(R_L + R_D)/(R_L \times R_D)]^2/ G^2$$

where G is the amplification of the low-noise amplifier.
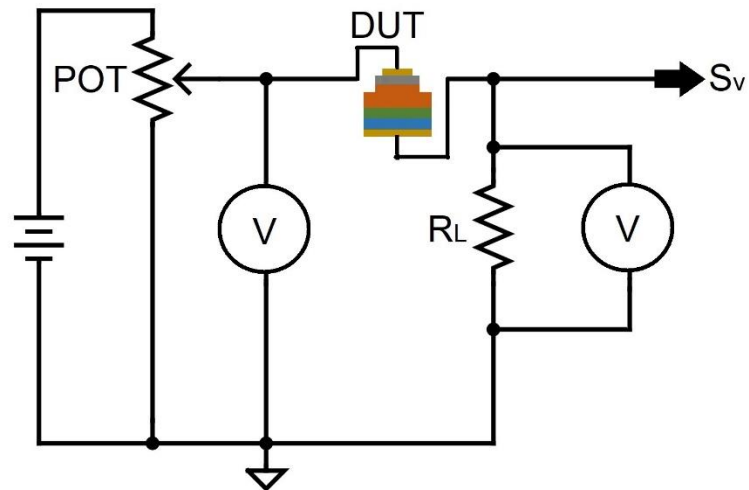
Figure 1-2: Schematic of a low-frequency noise measurement circuit for a vertical device. The circuit contains DC batteries, a potentiometer (POT), a device under test (DUT) and, a load resistor (R_L). Two multimeters connected to the system measure the voltage drops across the circuit and at the output.

1.4 Summary

In the chapter, the different types of electronic noise have been described with particular

emphasis on the low-frequency noise ($1/f$ and GR noise). Also, the setup and operational

principle of the home-built low-frequency noise measurement system have been discussed.

9

In the following four chapters, we will explain the useful properties of low-frequency noise as spectroscopy tools to study electronic materials and devices. Chapters 2 and 3 will deal with the usage of low-frequency noise as a reliability tool to study advanced semiconductor devices such as Diodes. In chapter 3, the reliability test has been done on an already existed technology, GaN-based PIN diodes. In chapter 4, the low-frequency noise reliability test results on the diamond diodes have been discussed, which is a new technology in its infancy and currently being investigated heavily for potential high-power applications. Chapters 4 and 5 will go through the capability of low-frequency noise to study the intrinsic properties of the advanced materials. In summary, our low-frequency noise technique in chapters 2 and 3 is focused on the device properties. On the other hand, Chapters 4 and 5 will deal with the viability of using the low-frequency noise system to verify intrinsic material properties (such as phase change properties of advanced materials).

References

1. A. A. Balandin Noise and Fluctuations Control in Electronic Devices, *American Scientific Publishers* **2002**, 258.

2. M. V. Haartman, M. Östling, Low-Frequency Noise in Advanced MOS Devices, *Springer* **2007**.

3. S. Kogan, Electronic Noise and Fluctuations in Solids, *Cambridge University Press* **1996**.

4. P. Dutta and P.M. Horn, *Reviews of Modern Physics* **1981**, 53, 497.

5. F.N. Hooge, T.G.M. Kleinpenning, and L. K. J. Vandamme, L. K. J, *Reports on Progress in Physics.* **1981**, 44, 479.

6. S. M. Kogan, *Soviet Physics Uspekhi* **1985**, 145, 285.

7. L.K.J. Vandamme, *IEEE Transactions on Electron Devices* **1994**, 41, 2176.

8. A. A. Balandin, *Nature Nanotechnology* **2013**, *8*, 549.

9. A.K. Raychaudhuri, *Current Opinion in Solid State and Materials Science* **2002**, 6, 67.

10. A. Hajimiri, and T.H. Lee, *IEEE J. Solid-State Circuits* **1998**, 33, 179.

11. B. Razavi, *IEEE Journal of Solid-State Circuits* **1996**, 31, 331.

12. G. Cibiel, L. Escotte, and O. Llopis, IEEE Transactions on Microwave **2004**, 52, 183.

13. Y. Dai, *Microelectronics Reliability* **1991**, 31, 75.

14. D.M. Fleetwood, S. Beyne, R. Jiang, S.E. Zhao, P. Wang, S. Bonaldo, M.W. McCurdy, Z. Tokei, I. Dewolf, K. Croes, E.X. Zhang, M.L. Alles, R.D. Schrimpf, R.A. Reed, and D. Linten, *Applied Physics Letters* **2019**, 114, 203501.

15. X.Y. Chen, A. Pedersen, and A.D. van Rheenen, *Microelectronics Reliability* **2001**, 41, 105.

16. K. Geremew, S. Rumyantsev, F. Kargar, B. Debnath, A. Nosek, M. A. Bloodgood, M. Bockrath, T. T. Salguero, R. K. Lake, A. A. Balandin, *ACS Nano* **2019**, *13*, 7231.

17. G. Liu, S. Rumyantsev, M. A. Bloodgood, T. T. Salguero, A. A. Balandin, *Nano Letters* **2018**, *18*, 3630.

18. R. Salgado, A. Mohammadzadeh, F. Kargar, A. Geremew, C. Y. Huang, M. A. Bloodgood, S. Rumyantsev, T. T. Salguero, A. A. Balandin, *Applied Physics Express* **2019**, *12*, 037001.

19. D.R. White, R. Galleano, A. Actis, H. Brixy, and M. D. Groot, *Metrologia* **1996**, 33 325.

20. J. Tworzydło, B. Trauzettel, M. Titov, A. Rycerz, and C. W. J. Beenakker, *Phys. Rev. Lett.* **2006**, 96, 246802.

21. R. Landauer, *Phys. Rev. B* **1993**, 47, 16427.

22. V. Mitin, L. Regianni, L. Varani, Generation- recombination noise in semiconductors; Balandin, A. A.; Noise and Fluctuations Control in Electronic Devices; American Scientific Publishers Los Angeles, 2002; pp. 12 – 31.

23. R. Müller, Noise in Physical Systems, *Springer* **1978**.

24. Y. Yuzhelevski, M. Yuzhelevski, and G. Jung, *Review of Scientific Instruments* **2000**, 71, 1681.

25. J. P. Campbell, J. Qin, K. P. Cheung, L. C. Yu, J. S. Suehle, A. Oates, K. Sheng, *IEEE International Reliability Physics Symposium Proceedings* **2009**, 382.

26. J. B. Johnson, *Physical Review* **1925**, *26*, 71.

27. M. Surdin, *Journal de Physique et le Radium* **1939**, *10*, 188.

28. F. N. Hooge, *IEEE Trans Electron Devices* **1994**, *41*, 1926.

29. L. K. J. Vandamme, F. N. Hooge, *Physica B Condens Matter* **2005**, *357*, 507.

2. Low-Frequency Noise Characteristics of GaN Vertical PIN Diodes

2.1 Introduction

Development of the next generation of GaN PIN diodes for high-power electronics requires effective methods for assessing materials and device quality. Low-frequency noise measurements have been widely used for the characterization of defects in various semiconductor devices, and for testing their reliability [1-14]. The noise level and its current or gate voltage dependence in the field-effect transistors can be used to compare the quality of the device structures. Temperature dependence of the low-frequency noise is often used to determine its origin and physical mechanism. Accurate knowledge of the specific semiconductor devices' noise characteristics is also required for circuit level modeling. The information on the low-frequency noise characteristics of GaN PIN diodes is limited [15]. No direct comparison between different technologies is available. There are no detailed studies of how chemical treatment and etching, used in device fabrication, affect the noise level of GaN PIN diodes.

Selective-area doping is a key to the fabrication of high-performance advanced GaN power devices [16]. Epitaxial regrowth is the preferable method for GaN PIN diodes fabrication compared to diffusion and ion implantation for selective-area doping [16-19]. Selective *p*-doping by regrowth technologies that included dry etching before the regrowth were previously reported [16-18]. Optimization of the etch-then-regrow process is important for further development of GaN high-power electronics. The regrowth often results in a high concentration of impurities, including silicon, carbon, and oxygen; the dry etching process can also introduce surface damage [16-18]. The impurity atoms and surface defects can act as trapping and recombination centers, potentially leading to a substantial increase in low-frequency noise. In this dissertation chapter, we report an investigation of noise characteristics of GaN PIN diodes and demonstrate that the low-frequency noise at low currents is a convenient and useful figure-of-merit for the quality of GaN PIN diodes.

2.2 Vertical PIN Diode Device Fabrications

The GaN vertical PIN diode devices were prepared by Prof. Yuji Zhao's research group at Rice University, USA. First, the GaN layer were grown on c-plane n-GaN free-standing conducting substrates by metalorganic chemical vapor deposition (MOCVD). Several different technologies have been considered: the etch-then-regrow structures with relatively high interface quality obtained by the low RF power etching and UV-Ozone and chemical treatment (Type I); etch-then-regrow structures with lower interface quality

14

obtained without the UV-Ozone or chemical treatment (Type II); as-grown devices with the guard rings (Type III). In Type I devices, the low-power RF dry etching along with UV-Ozone and chemical treatments were used to form high-quality regrowth interfaces. The Type II devices have the same regrown structure as Type I but were fabricated using a higher etching RF power (70 W) without the surface treatment. The Type III devices were based on as-grown structures without a regrowth interface. A guard ring structure was made on Type III devices to improve the breakdown voltage [19]. Metal contacts were
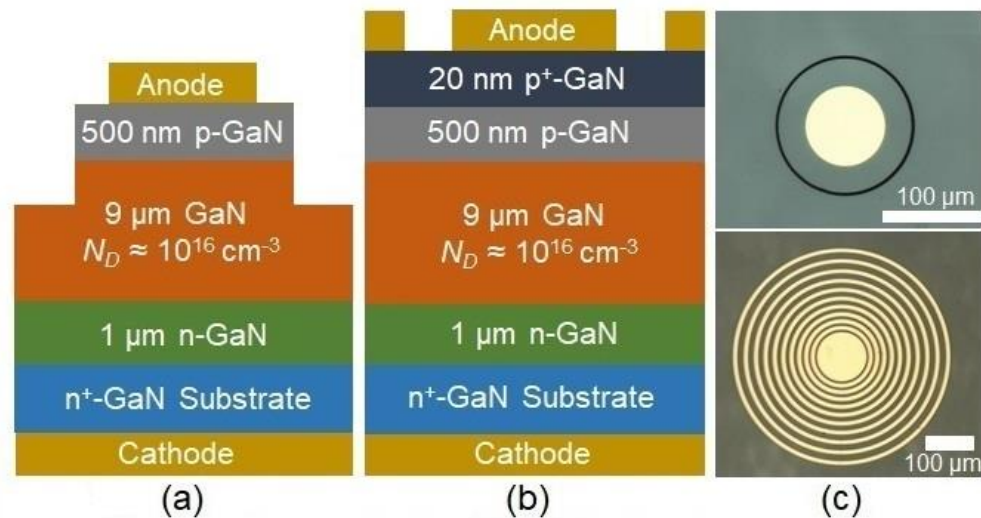
Figure 2-1: Schematics of the GaN PIN diode structures. (a) The layered structure of the regrown devices of Type I, II, and IV. Type I is the regrown devices with the low RF power dry etching and UV chemical treatments; Type II is the regrown devices with the high RF power dry etching without any chemical treatment; Type IV is the regrown device without chemical treatment with a relatively large leakage current, intentionally selected as a reference structure. (b) The layered structure of the Type III as-grown devices with guard rings. (c) Optical microscopy images of a regrown Type II device with a mesa (top) and as-grown Type III device (bottom). Reprinted with permission from S. Ghosh et al., Applied Physics Letters. **2021**, 119, 243505, Copyright © 2021 AIP Publishing.

deposited using electron-beam evaporation to form the anode and cathode contacts for all the devices. Additional details of the fabrication process, including the geometry of the etched regions, chemical treatment recipes, have been reported elsewhere [16-19]. In order to better correlate the noise level with the leakage current, we selected an additional regrown device, fabricated without etching or chemical treatment, which had relatively large leakage current. We refer to this reference device as Type IV. The layered structures for studied devices are shown in Figure 2-1.

2.3 Room Temperature Electrical and Noise Characterizations

The current-voltage (I-V) and low-frequency noise characteristics for all types of the PIN diodes were measured at room temperature in vacuum (Agilent B1500; Lake Shore TTPX). The noise spectra were acquired with a dynamic signal analyzer (Stanford Research 785). The signal analyzer was used to measure the absolute voltage-referred noise spectral density, S_V, on a load resistor, R_L, in series with the device under test, R_D. The load resistor was grounded in our configuration. A potentiometer was used to control the voltage supplied with a low noise battery. During the noise measurements, the voltage fluctuations were transferred to a low-noise preamplifier; then the amplified time domain signal was transformed to its corresponding frequency domain using a dynamic signal analyzer. The spectral density, S_V, was recalculated to the current spectral density S_I, and then normalized by the current squared, I^2, and the cross-section area of the PIN diodes. Details of the noise

measurements procedures, in the context of other material systems, have been reported by our research group elsewhere [20-23].

We start by comparing I-V and noise characteristics of different PIN diodes belonging to the same type. Figure 2-2 (a) shows I-Vs for three representative devices of Type I. At the forward voltage, V_F, in the range 3 V$>V_F>$2.5 V the I-V characteristics are exponential with the ideality factor ~2 for all devices. At $V_F >$3 V, the characteristics in the semi-logarithmic scale tend to saturate indicating the dominant contribution of the series resistance. At low bias $V_F <$2.5 V, the devices of the same type behave differently demonstrating the different levels of the leakage current. The leakage current is the highest for device A, followed by devices B, and C. Among these three tested diodes, device C demonstrated the best performance. Figure 2-2 (b) shows the bias points for the noise measurements in the device A. The device with the higher leakage currents was selected intentionally to illustrate the correlation between I-Vs and noise characteristics. In Figures 2-2 (c), we present the current noise spectral density, S_I, for device A as a function of frequency, f, at different currents. One can see that the noise is of the general $1/f$ type, particularly at higher currents, $i.e.$, at $I=$ 0.01 A and 0.005 A. At lower currents, $I\leq$ 50 µA, the noise spectra reveal the generation‐recombination (G-R) bulges. From analysis of the data, we concluded that devices with larger leakage currents are typically those that have G-R features in their noise spectra. The noise in the device C, with the lowest leakage current, was of the $1/f$ type. These data suggest that G-R noise is caused by the defects acting as the recombination centers, which are responsible for the higher leakage currents at low bias.

17
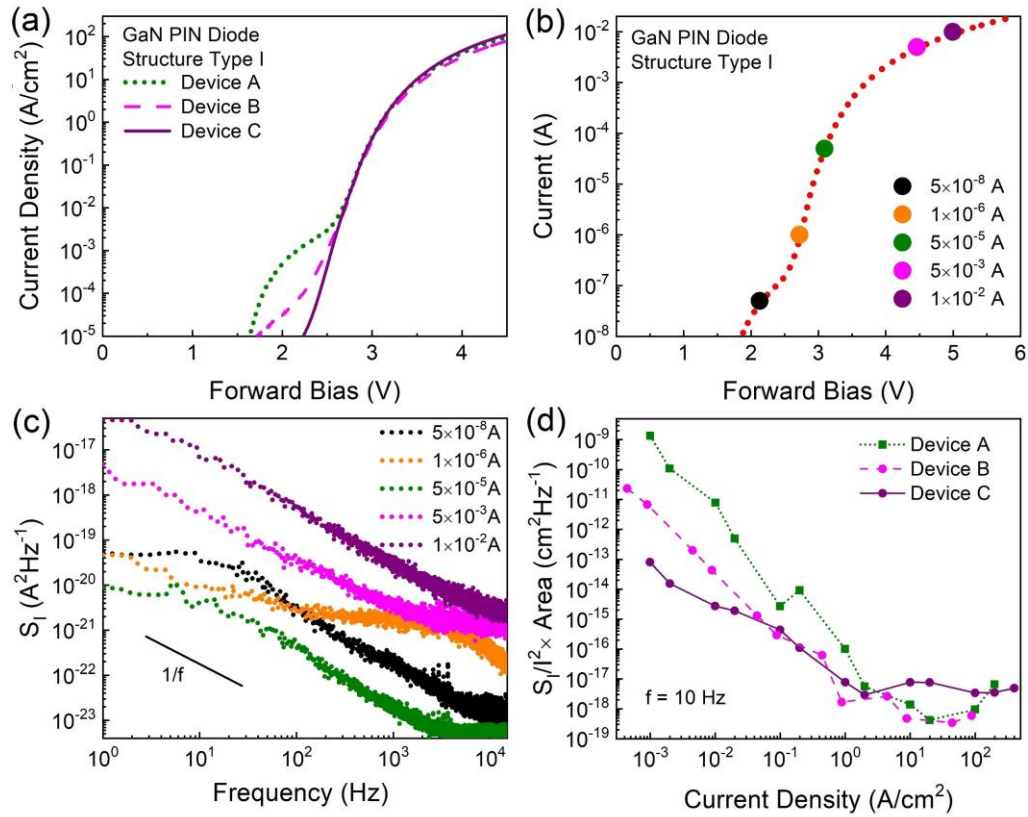
Figure 2-2: Electrical and noise characteristics of three different devices of the same Type I. (a) Current-voltage characteristics of the Type I devices, A, B, and C, with different leakage currents. (b) Current-voltage characteristics of device A with colored dots indicating the noise measurement data points. (c) Low-frequency noise spectra for different currents indicated in panel (b). Note G-R bulges in the noise spectra at low currents. At high currents, the noise is of the typical *1/f* type. (d) The normalized current noise spectral density, S_I/I^2, as a function of the current density for three devices measured at f = 10 Hz. Reprinted with permission from S. Ghosh et al., Applied Physics Letters. **2021**, 119, 243505, Copyright © 2021 AIP Publishing.

It is interesting that the noise at the intermediate current of $I=5\times10^{-5}$ A is the smallest, *i.e.*, G-R noise depends on current non-monotonically, and it has a minimum at some current. Similar behavior was reported previously for SiC *p-n* junction [24]. The model of the G-R noise developed in Ref. [24] confirms this kind of non-monotonical dependence. Therefore, we can conclude that the high leakage current in this device is not due to some parasitic channel leakage but rather due to the recombination in the space charge region. The current and area normalized noise spectral densities versus current density, at a fixed frequency $f=10$ Hz, are presented in Figure 2-2 (d) for all three devices. One can see that in all devices, the normalized noise spectral density decreases with the current density. The noise characteristics at low current density, i.e., $J<1$ A/cm^2, correlate perfectly the GaN PIN diode performance, i.e., the devices with the lowest leakage current have the lowest noise level. The low-frequency noise and the leakage current, are defined by the nature and concentration of the defects introduced during the processing steps which act as recombination centers. Therefore, the noise measured at low bias can be a sensitive metric of the device quality. Additional noise plots for Device A, B and C are shown in Figure 2-3 for reference and comparison at different current values.

Figure 2-4 (a) shows forward I-V characteristics of all four types of GaN PIN diodes. We selected device C from the 3 previously measured Type I devices due to its performance and lowest noise level. In Figure 2-4 (b) we present the I-V of a representative Type III as-grown device that had the best rectifying performance. Note that this I-V characteristic is close to a classical one. At low currents, the ideality factor $n_1=2.1$, which is close to the
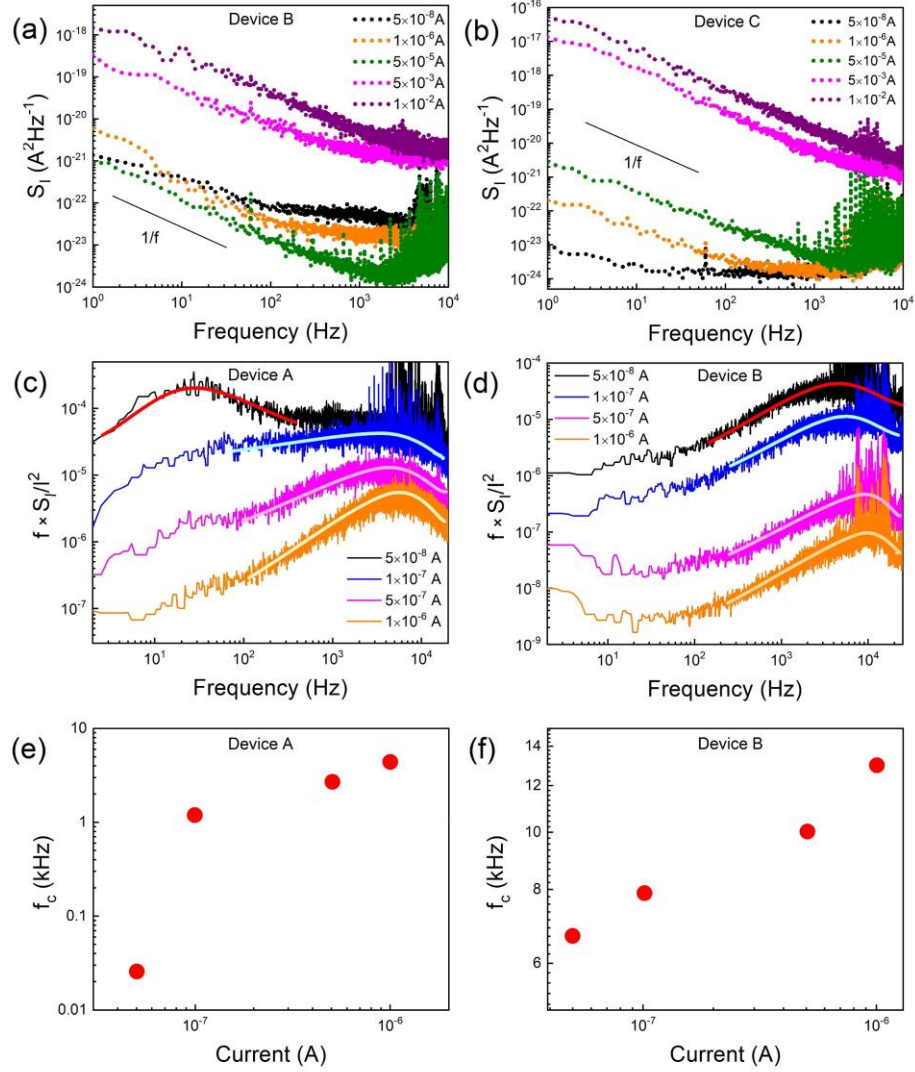
Figure 2-3: Additional noise spectrum data for Type I devices. (a) The current spectral density, S_I, as a function of frequency at different current levels for device B. Generation-recombination (G-R) Lorentzian bulges can be detected at lower currents similar to those in device A. (b) The corresponding S_I vs f characteristics for device C at different current levels. The spectra are dominated by *1/f* type noise at all measured currents. (c) The $f \times S_I/I^2$ *vs.* f plots for device A at lower currents plotted to extract the G-R contributions from each spectrum by separating the Lorentzian features from the *1/f* background. (d) Similar $f \times S_I/I^2$ *vs.* f plot for device B. (e) The corner frequencies, f_c, obtained from the maxima through numerical fittings shown as a function of current for device A. The corner frequency increases with increasing bias voltage. (f) The corresponding f_c vs I plot for device B. Reprinted with permission from S. Ghosh et al., Applied Physics Letters. **2021**, 119, 243505, Copyright © 2021 AIP Publishing.

ideal recombination current, as it should be at low bias. At the current density $J>10^{-2}$ A, the diffusion current starts to contribute, leading to the ideality factor decrease to $n_2=1.6$. Figure 2-4 (c) shows the current noise spectral density as a function of the current density at a fixed frequency $f=10$ Hz for all types of the devices. The data are plotted for each type of GaN PIN diodes with the corresponding I-Vs shown in Figure 2-4 (a). There are several important observations. The S_I vs. J (S_I vs. I) relation follows the trend $S_I \sim J$ ($S_I \sim I$), observed in many different *p-n* and Schottky diodes. At low currents, one can notice the deviation from this trend, particularly for the Type II and Type IV devices. We attribute this deviation to the appearance of the G-R bulges in these devices at low currents. This is in line with the explanation of a higher concentration of some specific defects, acting as recombination centers, which result in higher leakage current and noise level. One should note that noise with $1/f$ spectrum can also be a superposition of G-R noise bulges from several distinctive defects which are characterized by different time constants [25]. A prior study of GaN/AlGaN PIN diodes of a different design on a sapphire substrate reported $S_I \sim I^2$, similar to a linear resistor [26]. However, there have been reports for AlGaN PIN photodetector diodes with $S_I \sim I$ [27]. It is interesting to note that noise in the studied diodes is at least four to seven orders of magnitude lower than that reported for GaN/AlGaN PIN diodes in Ref. [15] and comparable to those in the lateral GaN/AlGaN Schottky diodes [28].
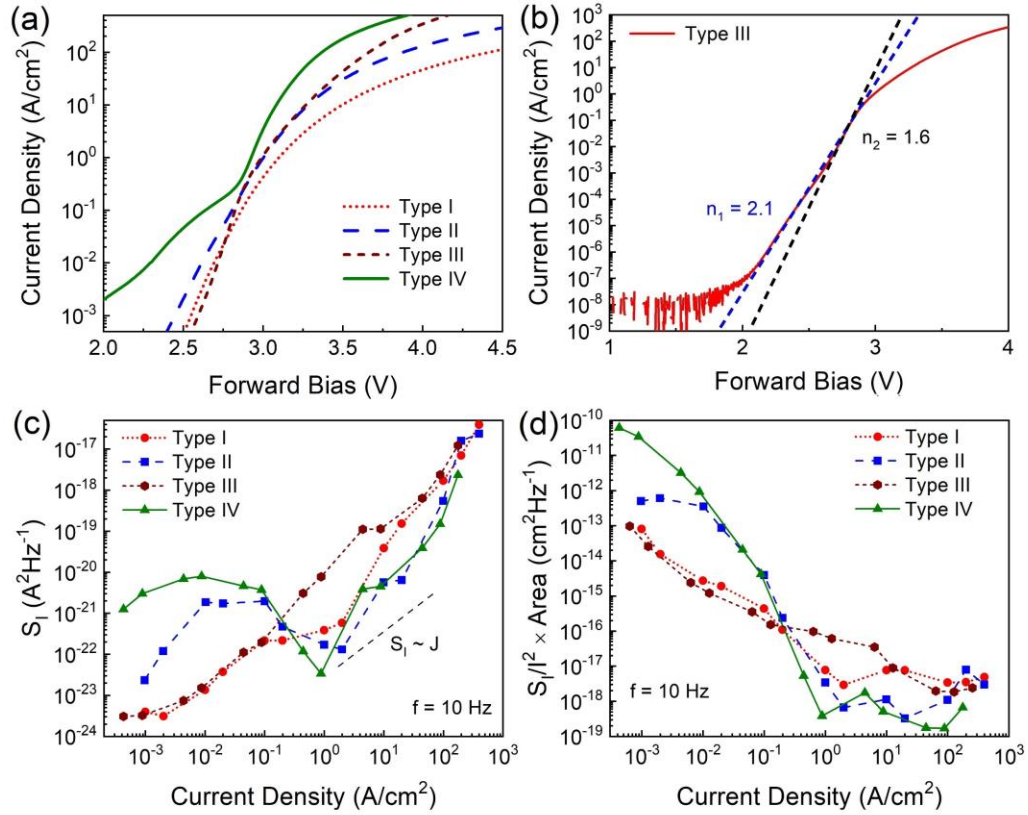
Figure 2-4: Electrical and noise characteristics of GaN PIN diodes of different type. (a) Current-voltage characteristics of representative devices of each type. (b) The forward bias current density for Type III as-grown PIN diode clearly showing the ideality factor. Note that the ideality factor takes values of 2.1 and 1.6 in the recombination and diffusion regions, correspondingly. (c) The current noise spectral density, S_I, as a function of the current density, J, at $f = 10$ Hz. (d) The normalized current noise spectral density, S_I/I^2, as a function of the current density at $f = 10$ Hz. The normalized noise level is correlated with the respective electrical properties at low currents. Reprinted with permission from S. Ghosh et al., Applied Physics Letters. **2021**, 119, 243505, Copyright © 2021 AIP Publishing.

For a more accurate and direct comparison of the noise level in each GaN PIN technology, in Figure 2-4 (d), we plot the current noise spectral density normalized by the current squared and device area, $S_I/I^2 \times \Omega$, vs. current density, J, at fixed f=10 Hz (Ω is the area of the top contact). One can see that at the small currents, $J<0.1$ A/cm^2, the lowest noise is in the diodes of Type I and Type III while the highest level of noise is in the reference Type IV PIN diode which is characterized by the high leakage current. This observation suggests that the chemical treatment and etching in our devices did not result in the strongly increased noise. We also note that the noise characteristics at low currents are the most informative since they are defined by the carrier recombination with participating of slow
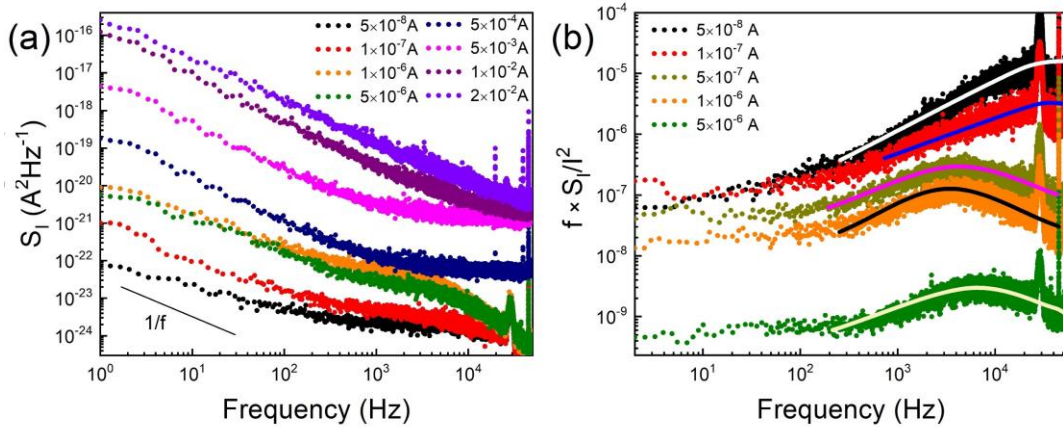
Figure 2-5: Noise characteristics of a Type II device at room temperature. (a) The current spectral density, S_I, as a function of the frequency plotted at different current levels. (b) The G-R bulges can be detected at lower current values, which contribute to the deviation from $S_I \sim J$ trend at lower currents. Reprinted with permission from S. Ghosh et al., Applied Physics Letters. **2021**, 119, 243505, Copyright © 2021 AIP Publishing.
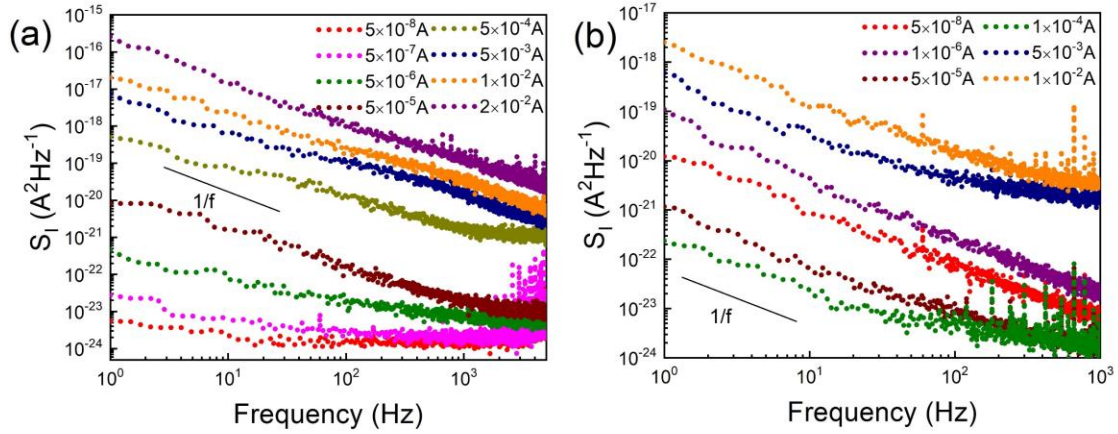
Figure 2-6: Noise characteristics of Type III and Type IV devices at room temperature. (a) The current spectral density, S_I, as a function of frequency plotted at different current levels for Type III device. The noise is of *1/f* type without visible G-R contributions. (b) The S_I vs *f* characteristics plotted for Type IV device. The noise is of *1/f* type. The non-monotonic $S_I \sim J$ dependence can be explained by superposition of several G-R trap levels with different characteristics time contacts, which results in the *1/f* type noise. Reprinted with permission from S. Ghosh et al., Applied Physics Letters. **2021**, 119, 243505, Copyright © 2021 AIP Publishing.

processes that contribute to the low-frequency noise. For all devices, the normalized noise spectral density decreases with the increasing current density. At higher currents, the noise S_I/I^2 tends to be independent on the current, which is typical behavior for the noise from a linear resistor. This noise is due to the series resistance of the devices. The noise spectra at different device currents for Type II, Type III and Type IV devices can be found in Figures 2-5 and 2-6.

2.4 Temperature Dependent Electrical and Noise Characterizations

To shed light on the physical mechanism of noise in these devices, we measured noise as a function of temperature. Measurements at elevated, rather than low temperatures, have proven to be informative for devices based on wide-band-gap semiconductors [29-32]. The elevated temperatures are also more relevant to the intended high-power applications of GaN PIN diodes. In Figure 2-7, we present the temperature dependent electrical (Figure 2-7 (a)) and noise characteristics (Figure 2-7 (b-d)) of a representative as-grown GaN PIN diode, defined above as Type III. The I-V characteristics are exponential at all studied temperatures with the ideality factor only weakly dependent on temperature. It means that even at elevated temperatures and at low bias the current is still of recombination origin without significant contribution of the parasitic leakage. It is interesting to note that the noise spectral density dependences on the current density reveal peaks for the temperatures in the range from T=375 K to T=450 K. Three regions with the changing as a function of temperature, $S_I \sim I^\zeta$, dependence can be distinguished in Figure 2-7 (c). In region I, ζ changes approximately from ~1 to ~2; in region II, it varies between ~1 and some negative values; and in the high-current region III, ζ stabilizes to around ~2, as one observes in linear resistors (Refer to Figure 2-8). The noise dependence on temperature (Figure 2-7 (d)) reveals peaks for the current levels that correspond to the transition from region I to II (in Figure 2-7 (c)). The current dependences of noise at elevated temperatures resemble those observed for the devices with the elevated leakage current and G-R noise spectra (Figure 2-2). Temperature and current dependences of noise, which demonstrate maxima, are
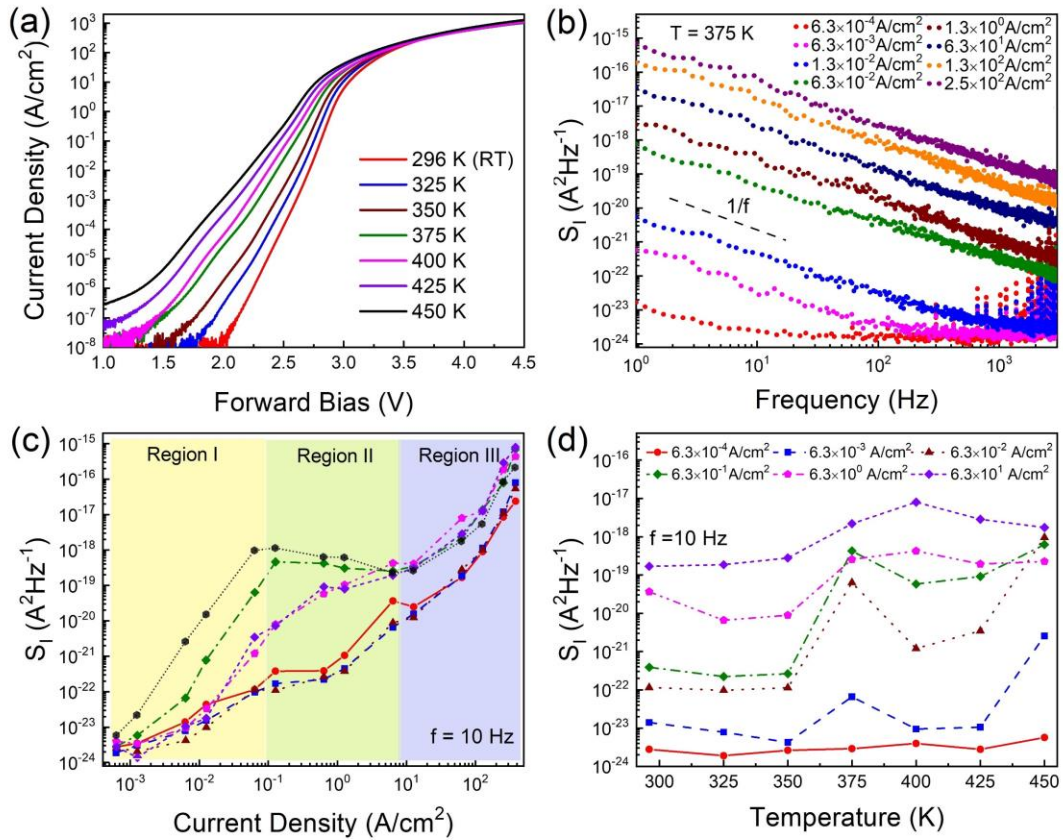
Figure 2-7: Temperature dependent electrical and noise characteristics of GaN PIN diode of Type III. (a) Current-voltage characteristics of a representative GaN PIN diode at elevated temperatures. (b) The current noise spectral density, S_I, as a function of frequency measured at different currents. (c) The current noise spectral density, S_I, as a function of the forward current density at $f = 10$ Hz shown for different temperatures. The colors of the curves correspond to the temperatures indicated in the (a) panel. (d) The current noise spectral density, S_I, as a function of the temperature T, shown for different current densities at $f = 10$ Hz. Reprinted with permission from S. Ghosh et al., Applied Physics Letters. **2021**, 119, 243505, Copyright © 2021 AIP Publishing.

characteristic features of G-R origin of noise [24]. The latter suggest that the 1/f noise in the devices of Type III is still of the G-R origin. The increase of the recombination current at elevated temperatures helps to reveal this noise mechanism. Since the noise spectra shapes are still 1/f-like we have to conclude that at least several levels with different characteristic times contribute to noise within the studied frequency band.
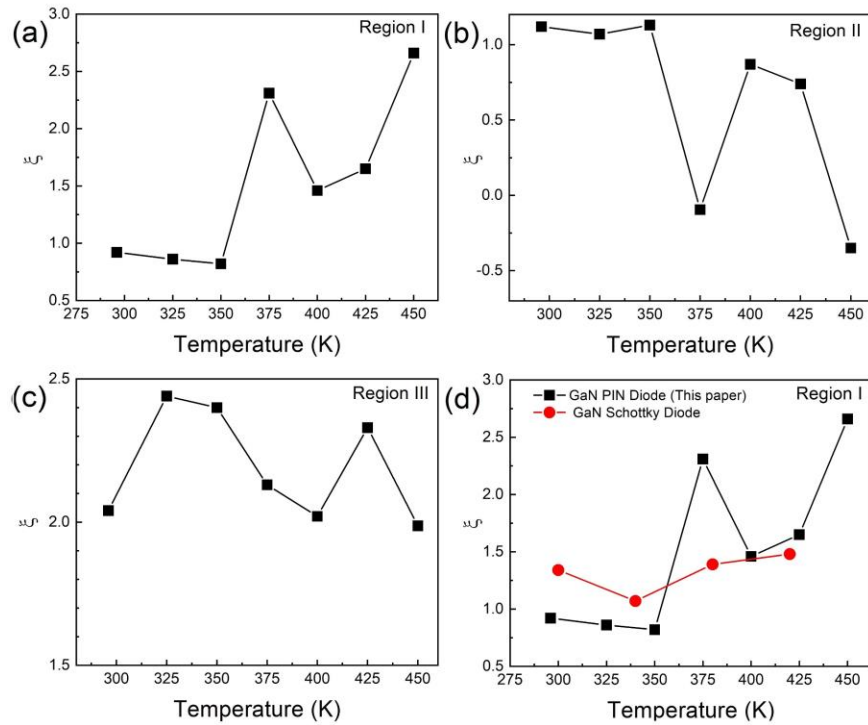
Figure 2-8: The ζ values from $S_I \sim I^\zeta$ characteristics for Type III device in (a) region I, (b) region II and (c) region III. (d) The corresponding ζ value comparisons with published data for GaN Schottky diode [33]. Reprinted with permission from S. Ghosh et al., Applied Physics Letters. **2021**, 119, 243505, Copyright © 2021 AIP Publishing.

2.5 Conclusions

In conclusion, we reported on a study of low-frequency noise in vertical GaN PIN diodes of different designs and process technologies. The noise characteristics were measured at different current densities and elevated temperatures relevant to the high-power switch applications. The noise in all considered device types has a characteristic *1/f* spectrum at high currents. Some devices with the largest leakage current revealed G-R bulges at low currents. The noise spectral density, S_I, predominantly scales with the current, I, as $S_I \sim I$. Out data indicate that the noise measurements at low currents can be used to efficiently assess the quality of GaN PIN diodes.

References

1. A. A. Balandin, Noise and Fluctuations Control in Electronics Devices, *American Scientific Publishers* **2002**.

2. L.K.J. Vandamme, *IEEE Transactions on Electron Devices* **1994**, 41, 2176.

3. P. Dutta and P.M. Horn, *Reviews of Modern Physics* **1981**, 53, 497.

4. A. Balandin, S. Morozov, G. Wijeratne, S. J. Cai, R. Li, J. Li, K. L. Wang, C. R. Viswanathan, and Y. Dubrovskii, *Applied Physics Letters* **1999**, 75, 13.

5. S.L. Rumyantsev, N. Pala, M.S. Shur, E. Borovitskaya, A.P. Dmitriev, M.E. Levinshtein, R. Gaska, M.A. Khan, J. Yang, X. Hu, and G. Simin, *IEEE Transactions on Electron Devices* **2001**, 48, 530.

6. J. Tartarin, G. Soubercaze-Pun, J. Grondin, L. Bary, J. Mimila-Arroyo, and J. Chevallier, *AIP Conference Proceedings* **2007**, 922, 163.

7. A. V. Vertiatchikh and L.F. Eastman, *IEEE Electron Device Letters* **2003**, 24, 535.

8. T.M. Chen and A.M. Yassine, *IEEE Transactions on Electron Devices* **1994**, 41, 2165.

9. H. Rao and G. Bosman, *Journal of Applied Physics* **2010**, 108, 053707.

10. H.P. Rao and G. Bosman, *IEEE Transactions on Device and Materials Reliability* **2012**, 12, 31.

11. M. Silvestri, M.J. Uren, N. Killat, D. Marcon, and M. Kuball, *Applied Physics Letters* **2013**, 103, 043506.

12. D.M. Fleetwood, S. Beyne, R. Jiang, S.E. Zhao, P. Wang, S. Bonaldo, M.W. McCurdy, Zs. Tőkei, I. DeWolf, K. Croes, E.X. Zhang, M.L. Alles, R.D. Schrimpf, R.A. Reed, and D. Linten, *Applied Physics Letters* **2019**, 114, 203501.

13. N.A. Hastas, C.A. Dimitriadis, and G. Kamarinos, *Applied Physics Letters* **2004**, 85, 311.

14. I.-H. Lee, A.Y. Polyakov, S.-M. Hwang, N.M. Shmidt, E.I. Shabunina, N.A. Talnishnih, N.B. Smirnov, I. v. Shchemerov, R.A. Zinovyev, S.A. Tarelkin, and S.J. Pearton, *Applied Physics Letters* **2017**, 111, 062103.

15. L. Dobrzanski and W. Strupinski, *IEEE Journal of Quantum Electronics* **2007**, 43, 188.

16. K. Fu, H. Fu, H. Liu, S.R. Alugubelli, T.-H. Yang, X. Huang, H. Chen, I. Baranowski, J. Montes, F.A. Ponce, and Y. Zhao, *Applied Physics Letters* **2018**, 113, 233502.

17. K. Fu, H. Fu, X. Huang, H. Chen, T.H. Yang, J. Montes, C. Yang, J. Zhou, and Y. Zhao, *IEEE Electron Device Letters* **2019**, 40, 1728.

18. K. Fu, H. Fu, X. Deng, P.-Y. Su, H. Liu, K. Hatch, C.-Y. Cheng, D. Messina, R.V. Meidanshahi, P. Peri, C. Yang, T.-H. Yang, J. Montes, J. Zhou, X. Qi, S.M. Goodnick, F.A. Ponce, D.J. Smith, R. Nemanich, and Y. Zhao, *Applied Physics Letters* **202**1, 118, 222104.

19. H. Fu, J. Montes, X. Deng, X. Qi, S.M. Goodnick, F.A. Ponce, Y. Zhao, K. Fu, S.R. Alugubelli, C.Y. Cheng, X. Huang, H. Chen, T.H. Yang, C. Yang, and J. Zhou, *IEEE Electron Device Letters* **2020**, 41, 127.

20. A.A. Balandin, *Nature Nanotechnology* **2013**, 8, 549.

21. G. Liu, S. Rumyantsev, M.A. Bloodgood, T.T. Salguero, and A.A. Balandin, *Nano Letters* **2018**, 18, 3630.

22. A. Geremew, C. Qian, A. Abelson, S. Rumyantsev, F. Kargar, M. Law, and A. A. Balandin, *Nanoscale* **2019**, 11, 20171.

23. S. Ghosh, F. Kargar, A. Mohammadzadeh, S. Rumyantsev, and A.A. Balandin, *Advanced Electronic Materials*, **2021**, 7, 2100408.

24. S.L. Rumyantsev, A.P. Dmitriev, M.E. Levinshtein, D. Veksler, M.S. Shur, J.W. Palmour, M.K. Das, and B.A. Hull, *Journal of Applied Physics* **2006**, 100, 064505.

25. M. V. Haartman, M. Östling, Low-Frequency Noise in Advanced MOS Devices, *Springer* **2007**.

26. L.S. Ma, Z. Bi, A. Bartels, K. Kim, L. Robertsson, M. Zucco, R.S. Windeler, G. Wilpers, C. Oates, L. Hollberg, and S.A. Diddams, *IEEE Journal of Quantum Electronics* **2007**, 43, 139.

27. T. Li, D.J.H. Lambert, M.M. Wong, C.J. Collins, B. Yang, A.L. Beck, U. Chowdhury, R.D. Dupuis, and J.C. Campbell, IEEE Journal of Quantum Electronics **2001**, 37, 538.

28. G. Cywiński, K. Szkudlarek, P. Kruszewski, I. Yahniuk, S. Yatsunenko, G. Muzioł, C. Skierbiszewski, W. Knap, and S.L. Rumyantsev, *Applied Physics Letters* **2006**, 109, 033502.

29.   Y.-Y. Chen, Y. Liu, Y. Ren, Z.-H. Wu, L. Wang, B. Li, Y.-F. En, and Y.-Q. Chen, *Modern Physics Letters* B **2020**, 35, 2150134.

30.   D. V. Kuksenkov, H. Temkin, A. Osinsky, R. Gaska, and M.A. Khan, *Applied Physics Letters* **1998**, 72, 1365.

31.   D. V. Kuksenkov, H. Temkin, A. Osinsky, R. Gaska, and M.A. Khan, *Journal of Applied Physics* **1998**, 83, 2142.

32.   B.H. Leung, N.H. Chan, W.K. Fong, C.F. Zhu, H.F. Lui, C.K. Ng, K.C. Wong, and C. Surya, *Proceedings of the IEEE Hong Kong Electron Devices Meeting* **2001**, 148.

33.   Y. Y. Chen, Y. Liu, Y. Ren, Z. H. Wu, L. Wang, B. Li, Y. F. En and Y. Q. Chen, *Modern Physics Letters B* **2021**, 35, 2150134-1.

3 Low-Frequency Noise in High-Current Diamond Diodes

3.1 Introduction

Ultra-wide bandgap (UWBG) semiconductors have emerged as important materials for power converters to meet the increasing efficiency needs [1-6]. Diamond is a promising UWBG material in terms of its critical electric field, drift velocity, carrier mobility, and thermal conductivity [7-13]. However, diamond chemical vapor deposition growth, processing, and doping are still in the early stages of development. Diamond technology is not as mature as that of GaN or SiC. Rather large concentrations of defects, including trap levels within the bandgap, can detrimentally affect diamond diode operation, *e.g.* by an increase in the diode turn-on voltage [8, 14-18]. Typical traps in diamonds have energy levels ranging from 0.2 eV to 1.7 eV. In the n-layer of the diode, the phosphorus dopant activation energy level is 0.43 eV to 0.63 eV [19,20] while in the p-layer the boron dopant activation energy level is ~0.3 eV [19]. Due to the high activation energies, only a small fraction of the dopant atoms is ionized. The defects and impurities, acting as charge carrier traps, negatively affect the reliability of the diodes, which is one of the most important metrics for applications in power converters for electricity grids. These considerations

explain the need for developing innovative techniques for assessing the material quality and reliability of diamond diodes.

Low-frequency electronic noise, also referred to as excess noise, has been used in characterizing reliability-limiting defects and impurities in electronic materials and devices [21-25]. The excess noise includes the $1/f$ and generation-recombination (G-R) noise with a Lorentzian type spectrum, which adds to the thermal and shot noise background (f is the frequency). It is known that $1/f$ noise can be an early indicator of electromigration damage and provide insight into the nature and energy distributions of reliability-limiting defects in the as-processed and aged materials and devices [21,26-29]. The excess noise often originates in the non-ideal components or the non-ideal currents of a device. These include leakage current, defects in the material, or parasitic resistances. The noise level increases at a much faster rate than the DC parameters as a device degrades under stress or as a result of its aging [30]. For this reason, noise can be used as a sensitive predictor of a lifetime. The rate of increase of the noise level can be related to the device mean-time-to-failure (MTTF). Since only short-time noise measurements are needed, the procedure for determining MTTF is non-destructive. To develop noise-based reliability assessment techniques for diamond diodes, one needs to conduct thorough studies of excess noise for this specific device type. The currently available data on noise in diamond devices are limited, with only a few published reports [31,32]. In this chapter, we report the results of the investigation of excess noise in diamond diodes designed specifically for applications

33

as high-current switches. The main objective of the study is to provide the noise-level baseline required for the development of reliability assessment.

3.2 Fabrication of Diamond Diode Structures

The fabrication of the diamond diodes was done by Prof. Robert J. Nemanich's research group at Arizona State University, USA. The diamond diodes were grown on a <111> highly boron-doped ($\sim 2 \times 10^{20}$ /cm^3) single crystal diamond plate (3×3×0.3 mm; TISNCM) [33]. A ~0.2 μm i-layer was grown on top of the B doped p^{++} substrate using a plasma-enhanced chemical vapor deposition (PECVD) with a mixture of H_2:CH_4:O_2 under a chamber pressure of 63 Torr and at 1000 W of microwave power. A ~0.15 μm moderately phosphorus-doped ($\sim 10^{18}$ /cm^3) n-layer was grown on top of the i-layer using an H_2:CH_4:TMP mixture under 60 Torr pressure and 2000 W microwave power in the PECVD chamber. A ~0.1 μm near-metallic highly conductive nitrogen-doped nano-carbon (nanoC) layer was grown on top of the n-layer to lower the contact resistance of the cathode contact. Additional growth details can be found in Ref. [34]. The active area of the diodes was defined by partial mesa etching the diamond into the i-layer using a SiO_2 hard mask and O_2/SF_6 chemistry in a reactive ion etcher. The top cathode and bottom anode contacts were defined by UV photolithography and e-beam deposition of a Ti-Ni-Au metal stack with 50 nm - 50 nm - 300 nm thicknesses. The layered structure of the devices and band diagram are shown in Figure 3-1 (a-b).
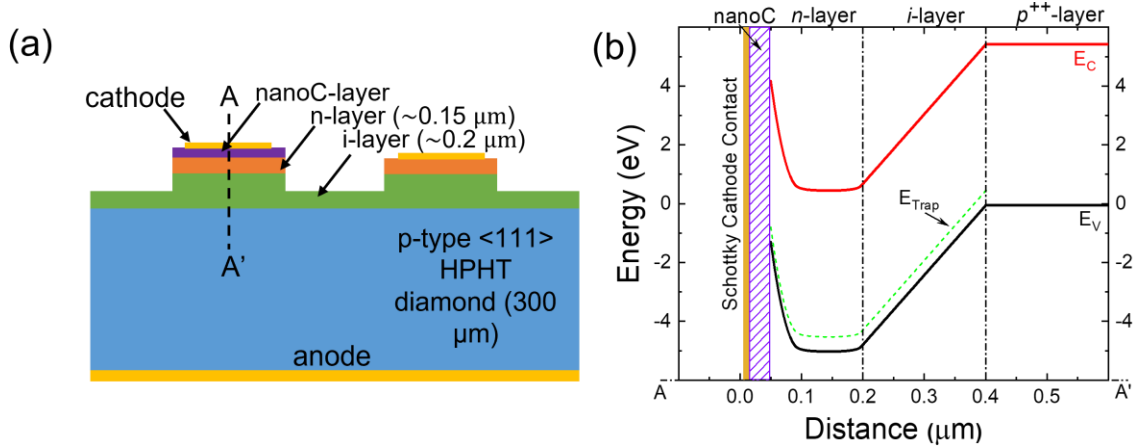
Figure 3-1: (a) Schematic of the layered structure of diamond diodes. (b) The band diagram at zero bias of a diamond diode including the trap levels as simulated by Silvaco ATLAS. Reprinted with permission from S. Ghosh et al., Applied Physics Letters. **2022**, 120, 062103, Copyright © 2022 AIP Publishing.

Although the nanoC layer provides a reduced contact resistance at the circular cathode contact, a Schottky barrier to electrons exists due to the Fermi-level pinning at the nanoC-n-layer interface. The Schottky barrier at the cathode contact can be seen from the band diagram generated from Silvaco ATLAS simulations using the diode structure (see Figure 3-1 (a-b)). The diode current is therefore largely dominated by the holes injected over the p^{++}-i-n junction barrier. The hole injection initially follows thermionic emission (TE) regime where the current is exponentially dependent on the small forward bias voltage, and then transitions into a space charge limited conduction (SCLC) where the current is proportional to V^m where m is ≥2 depending on the trap energy levels and trap density in the diode [8,35].

3.3 Electrical and Noise Measurement Results

The current-voltage (*I-V*) and low-frequency noise characteristics for all diodes were measured in a vacuum (Agilent; Lake Shore). The noise spectra were acquired with a dynamic signal analyzer (Stanford Research). Details of our noise measurements procedures, in the context of other material systems, have been reported by some of us elsewhere [36-38]. Figures 3-2 (a) and (b) show the *I-V* characteristics in forward bias for six different diamond diodes in linear and logarithmic scales, respectively. From the *I-V* characteristics, the tested diodes can be separated into two groups based on the respective turn-on voltage, V_T, of each diode. Devices 1, 2, and 3 have lower turn-on voltages, close to 5 V as compared to devices 4, 5, and 6 that have turn-on voltages of ~10 V or higher. The deviations from the ideal characteristics of these diodes and current jumps indicate the material imperfections owing to the infancy of the diamond diode growth and processing technology.

The noise measurements were conducted for all devices to examine variations in the noise characteristics for diodes with different turn-on voltages. In Figure 3-2 (c) we present the noise current spectral density, S_I, as a function of frequency for device 2 (V_T~5 V) for different currents through the diode. The noise spectra at all currents are the superposition of the 1/f and G-R noise with the pronounced Lorentzian spectral features. Similar noise spectra were measured for devices 1 and 3 with the low turn-on voltage (refer to Figures

3-3 (a-b)). The noise spectral density, S_I. as a function of frequency for device 6 with the

highest turn-on voltage is presented in Figure 3-2 (d).
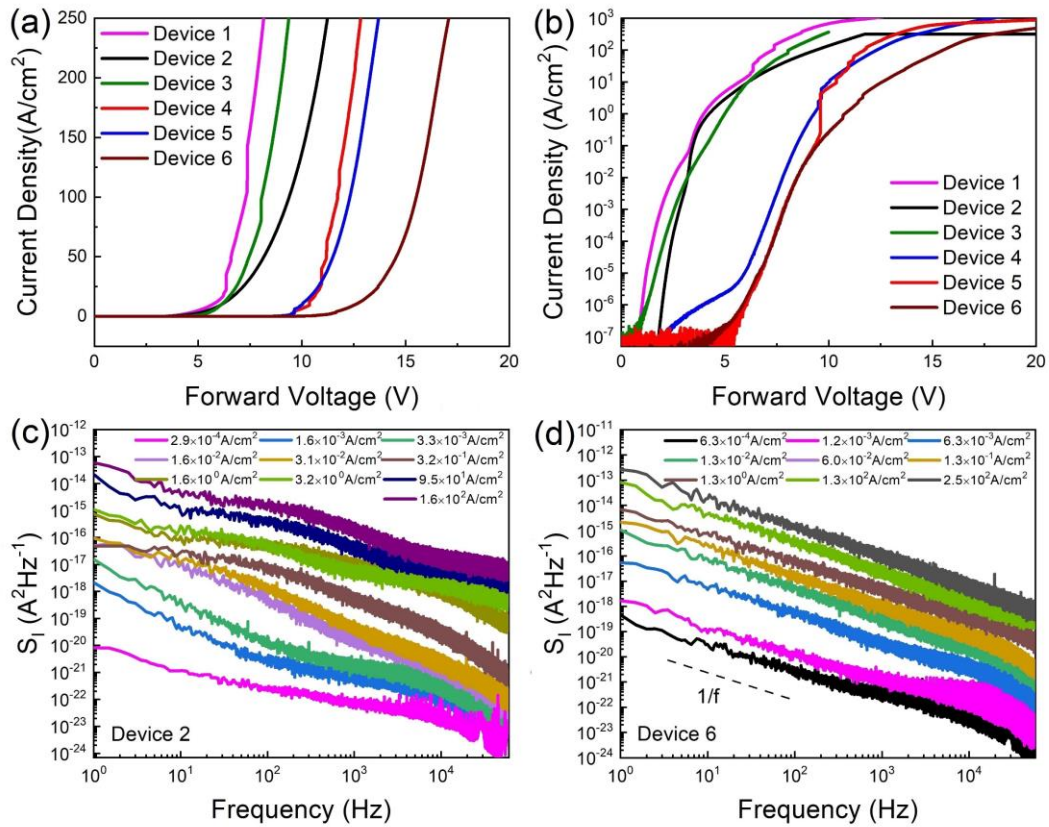
Figure 3-2: Current-voltage characteristics of six different diamond diodes plotted in linear (a) and logarithmic (b) scales. The diodes can be grouped as those with lower (V_T~5 V) and higher (V_T~10 V) turn-on voltages. (c) Noise current spectral density, S_I, as a function of frequency for different current densities, J, for device 2, with the low turn-on voltage. (d) Noise current spectral density, S_I, as a function of frequency for different current densities, J, for a device 6, with the high turn-on voltage. Reprinted with permission from S. Ghosh et al., Applied Physics Letters. **2022**, 120, 062103, Copyright © 2022 AIP Publishing.
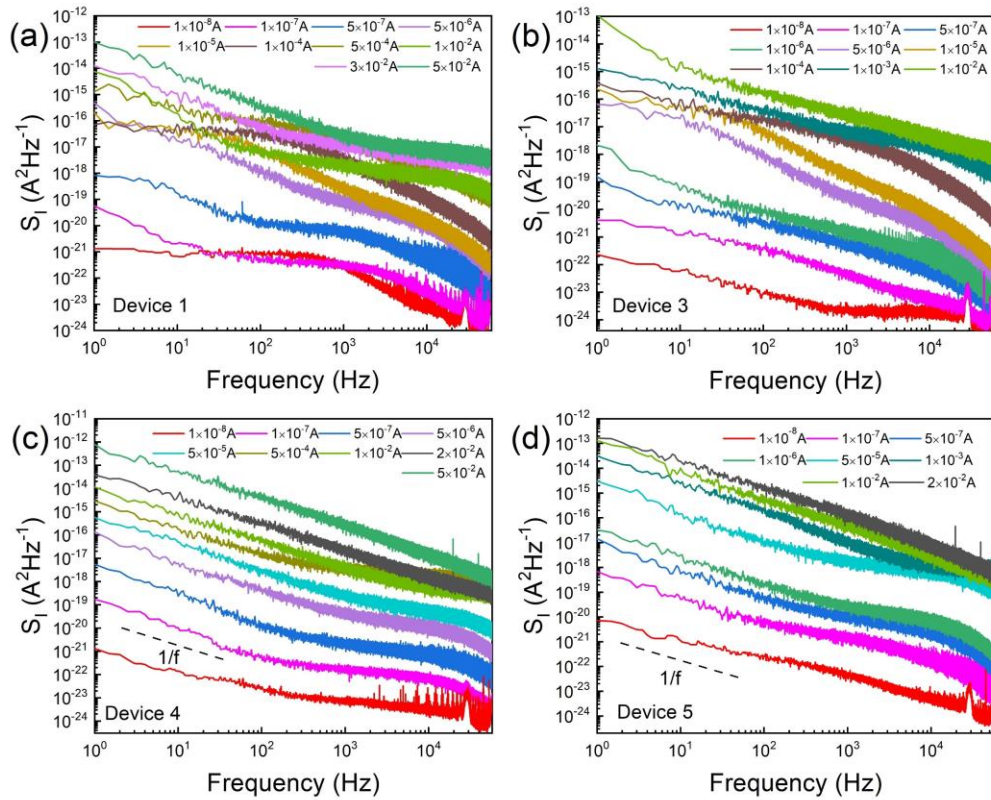
Figure 3-3: Noise current spectral density, S_I, as a function of frequency for different currents, I, for the lower turn on voltage devices: (a) device 1 and (b) device 3. The noise characteristics for both devices are dominated by the Lorentzian G-R noise at any device current similar to those of device 2. The S_I *vs f* spectra for high turn on voltage devices: (c) device 4 and (d) device 5. The spectra are of *1/f* type at lower frequencies as observed for device 3. Reprinted with permission from S. Ghosh et al., Applied Physics Letters. **2022**, 120, 062103, Copyright © 2022 AIP Publishing.

Interestingly, in this and other high turn-on voltage diodes, the noise is predominantly of the *1/f*-type. Some signatures of the deviation from 1/*f* spectrum and contribution of the G-R noise appear only at higher frequency (*f*~10 kHz). These noise characteristics were similar for all diodes with high turn-on voltages as seen in Figures 3-3 (c-d). The diamond diodes with the larger turn-on voltages are typically those that have a higher concentration of defects [8]. One may consider it unusual that the devices with more defects have 1/*f* spectrum while those with fewer defects show G-R spectral features. Below we explain it by the specifics of the noise mechanisms in diodes as compared to linear resistors or field-effect transistors (FETs).

Figure 3-4 (a) shows the noise current spectral density, S_I, as a function of the current density, *J*, at a fixed frequency *f*=10 Hz for all six tested devices. The S_I vs. *J* (S_I vs. *I*) relation for the measured diamond diodes follows the $S_I \sim J^2$ ($S_I \sim I^2$) trend at low currents. Although the dependence $S_I \sim I$ can be considered as a typical one for forward-biased diodes, $S_I \sim I^2$ dependences were also reported in *p-n* junction and Schottky diodes, including those based on wide bandgap semiconductors [39]. The $S_I(J)$ dependence becomes almost flat in the intermediate current density range, *i.e.* from about *J*~0.1 A/cm^2 to 100 A/cm^2. The $S_I \sim J^2$ noise behavior is restored at higher currents. It is interesting to note that the transition to the flat $S_I(J)$ dependence at the intermediate current levels roughly corresponds to the transition from the TE to SCLC hole transport regimes. In previous studies, the non-monotonic trends in the noise spectral density of GaN diodes were interpreted as the interplay of contributions to noise from the diode base, *p-n* junction region, and the series

resistances associated with the contacts [40]. A quantitative description for a non-monotonic trend was developed for SiC diodes [41].

To compare the noise characteristics of diamond diodes with those made of other material systems, we present the noise spectral density normalized by the current and device area in Figure 3-4 (b). For all measured diamond diodes, the normalized noise spectral density, $S_I/I^2 \times \Omega$, measured at fixed f=10 Hz, decreases with the increasing current density, J (Ω is the area of the top cathode contact). The decrease becomes slow or saturates completely at high current densities when the contributions from series resistances start to dominate the noise response. A comparison of the noise spectral density normalized to the area indicates a substantially higher noise level in diamond than that in GaN diodes [25]. Additional comparison of the noise characteristics in different device technologies is provided in table 3-1. The *I-V* and noise characteristics of the diamond diodes at elevated temperatures are shown in Figures 3-4 (c) and (d). One can see that both current and noise are weak functions of temperature, which are beneficial for high-power switching applications. Despite the high thermal conductivity of diamond, the high-current diodes can still experience substantial Joule heating at the considered power levels [8,42,43]. The thermal interface resistances between the layers increase the overall thermal resistance of the device structure [44]. The dashed lines in Figure 3-4 (c) show the slope of the exponential part of *I-V* characteristics, *e.g.*, $I \sim \exp(V \eta KT)$, at low currents. The ideality factor, η, decreases with the temperature increase. The decrease in the ideality factor together with almost constant noise level with temperature indicates that the performance of the diamond diodes can be

improved with increasing temperature. The latter is an extra benefit for applications of diamond diodes as high-power switches.
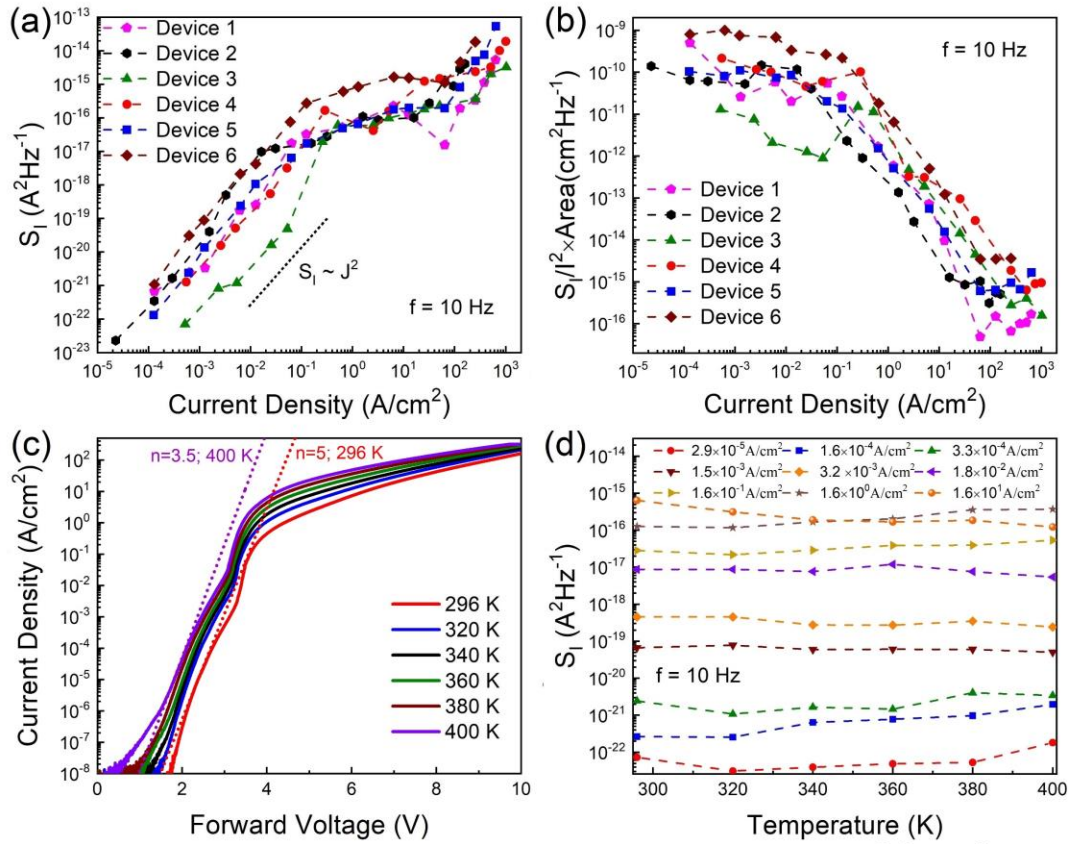
Figure 3-4: (a) Noise current spectral density, S_I, as a function of the current density, J, at f=10 Hz for all devices, measured at room temperature. (b) The normalized noise current spectral density, $S_I/I^2 \times \Omega$, as a function of J at f=10 Hz. (c) Current-voltage characteristics of a diamond diode (device 2) at elevated temperatures. (d) The noise spectral density, S_I, at f=10 Hz, as a function of temperature, measured for different current densities. Reprinted with permission from S. Ghosh et al., Applied Physics Letters. **2022**, 120, 062103, Copyright © 2022 AIP Publishing.

Table 3-1: Noise Comparison of Different Diode Technologies

Device Type	S_I (A^{2}Hz^{-1}) [f=10 Hz], I=10^{-6} A	Ref.
Diamond diode	10^{-17} - 10^{-18}	This work
GaN PIN	10^{-20} - 10^{-22}	[25]
GaN/AlGaN Schottky	10^{-18} - 10^{-21}	[40]
SiC p-n diode	10^{-23}	[41]

We now turn to a more detailed analysis of the G-R bulges observed in the spectra of the low turn-on voltage devices. Figures 3-5 (a) and (b) show the noise spectra of device 1 for J=1.3 A/cm^2 and J=1.3×10^{-3} A/cm^2, respectively. One can see an overlap of two Lorentzians at the intermediate current levels (panel (a)), and just one pronounced Lorentzian superimposed over 1/f shape at the small current level (panel (b)). The Lorentzians are shifting with the changing current level, and can go beyond the measurable range. We used fitting with Lorentzian to determine the corner frequency of the G-R noise. The G–R noise spectral density is described by the Lorentzian using an expression $S_I(f)=S_0/[1 + (2\pi f\tau)^2]$, where S_0 is the frequency-independent portion of $S_I(f)$ observed at $f<<(2\pi\tau)^{-1}$ and τ is the time constant associated with a particular fluctuation process. Figures 3-5 (c) and (d) show the characteristic frequency $f_c=(1/2\pi\tau)$ as a function of J for diamond diodes 1 and 2, respectively. The general trend for f_c is to increase with J. The functional dependence can be approximated as $f_c\sim J^\beta$, where β takes the values 0.31 and 1.15 for device 1, 1.39 for device 2, and 1.35 for device 3. The dependence of f_c on current in the diodes can be explained by the dependence of the trap capture time $\tau_{cap}=(nv\sigma)^{-1}$ on

42
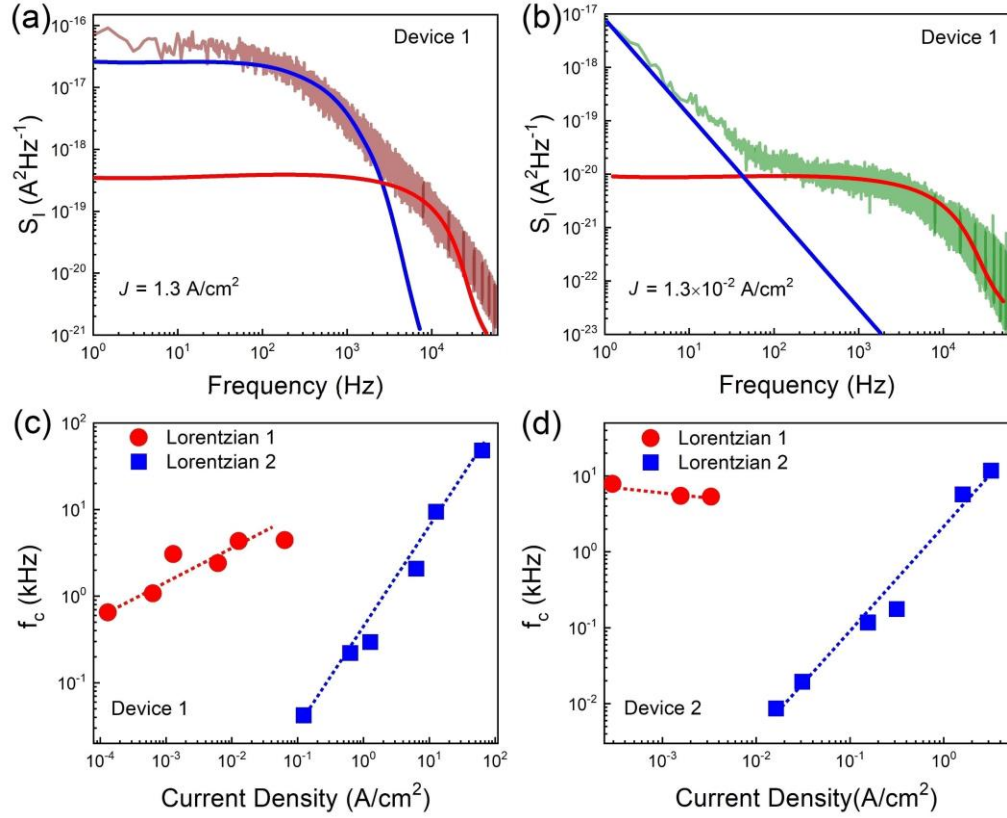
Figure 3-5: (a) Current noise spectral density, S_I, as a function of frequency at an intermediate current density, J=1.3 A/cm^2, for a device 1 with the low turn-on voltage. (b) The current noise spectral density, S_I, as a function of frequency at a low current density, J=1.3 ×10^{-2} A/cm^2, for the same device. Dependence of the corner frequency of the G-R bulges on the current density shown for (c) device 1 and (d) device 2. Reprinted with permission from S. Ghosh et al., Applied Physics Letters. **2022**, 120, 062103, Copyright © 2022 AIP Publishing.

the carrier concentration, n (where v is the charge carrier thermal velocity and σ is the capture cross-section) [45]. The current increase leads to the increase of the concentration, n, and corresponding increase of the corner frequency, f_c=($1/2\pi\tau$). This is true if the time constant τ is dominated by capture rather than emission time. Since our diamond diodes are characterized by the deeper, not fully ionized donor and acceptor states, high trap

concentration, and the hole-dominated charge transport, the obtained $f_c(J)$ relations for the diamond diodes are substantially different from those reported for GaN diodes [45]. It is interesting to note that characteristic frequencies for some Lorentzian, *e.g.* red line in Figure 5 (c), coincide with the current jumps in *I-V* characteristics – see the current jump at 3.3 V in Figure 3-2 (a). This adds support to the model, which correlates current jumps in the *I-V*s with the traps in the energy bandgap [8].

The G-R noise mechanisms in diodes are different from the G-R and 1/*f* noise mechanisms in bulk semiconductors and FETs [26,46]. In the McWhorter model for FETs, the 1/*f* noise emerges as an overlap of Lorentzian bulges due to traps with different time constants. The time constant, τ, of the trap is determined by its distance from the conduction channel, *e.g.*, $\tau=\tau_0\exp(\lambda z)$, where z is the distance of the trap from the channel, $\tau_0\sim10^{-10}$ s and λ is the tunneling parameter. In bulk semiconductors, one needs several levels or a continuous band of trap levels with different capture cross-sections, like the density of state tails near conduction and valence band edges, to construct the 1/*f* noise spectrum [47]. The situation in diodes is different. One of the conventional models for the low-frequency noise in a diode assumes that the emission and capture of carriers by the recombination level leads to the fluctuations of the charge state of this trap, and, as a result, to the fluctuations of the electric field distribution in the space charge region with the corresponding current fluctuations [48]. This model has been refined to correlate the current fluctuations with the fluctuations of the electric field not in the entire space-charge region but rather in a small vicinity of a trap in a specific location in the p-n junction region [41]. The local fluctuations

of the electric field are caused by the fluctuations of the charge state of the trap due to the exchange of electrons between this trap and the conduction band. Within this model, the same type of trap can give different time constants depending on its position in the diode structure since its energy level with respect to the Fermi energy is a strong function of the coordinate along the diode structure (see Figure 3-1 (b)). This can explain the evolution of G-R noise spectra to 1/f noise and observed differences in the noise for the same type of devices that have low and high turn-on voltages (see Figures 3-2 (c-d) and Figures 3). The diodes with the high turn-on voltage, which typically have more traps, have sufficient variation in the time constant, integrated over the junction length, to smooth out the G-R bulges to the *1/f* envelope.

The noise in diamond diodes shows variations not only for the devices with different turn-on voltage but also for low-current, intermediate-current, and high-current regimes (*e.g.* see Figures 3-4 (a-b)). In our case, the current regimes roughly correspond to TE, SCLC, and series resistance limited currents. In conventional diodes, the TE and SCLC regimes can be replaced with recombination and diffusive transport, respectively. The noise data for each regime has important implications for device reliability assessment [49]. The low-frequency noise measured at low bias is sensitive to the degradation of the active region [23,50]. At high bias, the measured noise reflects the degradation of the metal contacts and semiconductor layers contributing to the series resistance. Our data demonstrate that the difference in the noise level for different diodes is large at all currents (see Figure 3-4 (b)). The variations in the noise level are at their maximum, and span about three orders of

magnitude, at the low currents. Interestingly, the smallest noise level was observed for the devices with the low turn-on voltage and the highest noise was recorded for the devices with the high turn-on voltage. These observations attest to the potential of the noise spectroscopy for the diamond diode reliability assessment.

3.4 Conclusions

In conclusion, we reported the results of the investigation of excess noise in high-current diamond diodes. In high turn-on voltage diodes, the $1/f$ noise dominated, which can be attributed to the higher concentration of traps responsible for noise in these diodes. The G-R noise was found to be characteristic of diamond diodes with lower turn-on voltages. The dependences of noise spectral density, S_I, on forward current show different slopes, which can be correlated with different transport regimes in the diodes. The characteristic time constants, extracted from the G-R noise data, reveal uniquely strong dependence on current, attributed to the specifics of the charge transport and recombination processes in our diamond diodes. The obtained results are important for developing the noise spectroscopy-based approaches for the device reliability assessment for high-power diamond electronics.

References

1. S. Choi, S. Graham, S. Chowdhury, E.R. Heller, M.J. Tadjer, G. Moreno, and S. Narumanchi, *Applied Physics Letters* **2021**, 119, 170501.

2. Z. Liang, H. Du, Y. Yuan, Q. Wang, J. Kang, H. Zhou, J. Zhang, Y. Hao, X. Wang, and G. Zhang, *Applied Physics Letters* **2021**, 119, 252101.

3. M. Higashiwaki, R. Kaplar, J. Pernot, and H. Zhao, *Applied Physics Letters* **2021**, 118, 200401.

4. T. Matsumoto, T. Yamakawa, H. Kato, T. Makino, M. Ogura, X. Zhang, T. Inokuma, S. Yamasaki, and N. Tokuda, *Applied Physics Letters* **2021***, 119, 242105.

5. M. Wohlfahrt, M.J. Uren, Y. Yin, K.B. Lee, and M. Kuball, *Applied Physics Letters* **2021***, 119, 243502.

6. S. Lu, M. Deki, J. Wang, K. Ohnishi, Y. Ando, T. Kumabe, H. Watanabe, S. Nitta, Y. Honda, and H. Amano, *Applied Physics Letters* **2021**, 119, 242104.

7. N. Donato, N. Rouger, J. Pernot, G. Longobardi, and F. Udrea, *Journal of Physics D: Applied Physics* **2019**, 53, 093001.

8. H. Surdi, F.A.M. Koeck, M.F. Ahmad, T.J. Thornton, R.J. Nemanich, and S.M. Goodnick, *IEEE Transactions on Electron Devices* **2021**, 69, 254.

9. V. Jha, H. Surdi, M. Faizan Ahmad, F. Koeck, R.J. Nemanich, S. Goodnick, and T.J. Thornton, *Solid-State Electronics* **2021**, 186, 108154.

10. Y. Sasama, T. Kageura, K. Komatsu, S. Moriyama, J.I. Inoue, M. Imura, K. Watanabe, T. Taniguchi, T. Uchihashi, and Y. Takahide, Journal of Applied Physics **2020**, 127, 185707.

11. D. Das, A. Kandasami, and M.S. Ramachandra Rao, *Applied Physics Letters* **2021**, 118, 102102.

12. Y. Sasama, K. Komatsu, S. Moriyama, M. Imura, T. Teraji, K. Watanabe, T. Taniguchi, T. Uchihashi, and Y. Takahide, *APL Materials* **2018**, 6, 111105.

13. R. Nelz, J. Görlitz, D. Herrmann, A. Slablab, M. Challier, M. Radtke, M. Fischer, S. Gsell, M. Schreck, C. Becher, and E. Neu, *APL Materials* **2019**, **7**, 011108.

14. D. Araujo, F. Lloret, G. Alba, M.P. Alegre, and M.P. Villar, *Applied Physics Letters* **2021**, 118, 052108.

15.   T. Murooka, M. Shiigai, Y. Hironaka, T. Tsuji, B. Yang, T.M. Hoang, K. Suda, K. Mizuno, H. Kato, T. Makino, M. Ogura, S. Yamasaki, M. Hatano, and T. Iwasaki, *Applied Physics Letters* **2021**, 118, 253502.

16.   T. Hanada, S. Ohmagari, J.H. Kaneko, and H. Umezawa, *Applied Physics Letters* **2020**, 117, 262107.

17.   R.E. Lake, A. Persaud, C. Christian, E.S. Barnard, E.M. Chan, A.A. Bettiol, M. Tomut, C. Trautmann, and T. Schenkel, *Applied Physics Letters* **2021**, 118, 084002.

18.   P. Muret, J. Pernot, A. Kumar, L. Magaud, C. Mer-Calfati, and P. Bergonzo, *Physical Review B - Condensed Matter and Materials Physics* **2010**, 81, 235205.

19.   I. Stenger, M.A. Pinault-Thaury, T. Kociniewski, A. Lusson, E. Chikoidze, F. Jomard, Y. Dumont, J. Chevallier, and J. Barjon, *Journal of Applied Physics* **2013**, 114, 073711.

20.   J.Y. Tsao, S. Chowdhury, M.A. Hollis, D. Jena, N.M. Johnson, K.A. Jones, R.J. Kaplar, S. Rajan, C.G. van de Walle, E. Bellotti, C.L. Chua, R. Collazo, M.E. Coltrin, J.A. Cooper, K.R. Evans, S. Graham, T.A. Grotjohn, E.R. Heller, M. Higashiwaki, M.S. Islam, P.W. Juodawlkis, M.A. Khan, A.D. Koehler, J.H. Leach, U.K. Mishra, R.J. Nemanich, R.C.N. Pilawa-Podgurski, J.B. Shealy, Z. Sitar, M.J. Tadjer, A.F. Witulski, M. Wraback, and J.A. Simmons, *Advanced Electronic Materials* **2018**, 4, 1600501.

21.   L.K.J. Vandamme, *IEEE Transactions on Electron Devices* **1994**, 41, 2176.

22.   Y. Dai, *Microelectronics Reliability* **1991**, 31, 75.

23.   X.Y. Chen, A. Pedersen, and A.D. van Rheenen, *Microelectronics Reliability* **2001**, 41, 105.

24.   D.M. Fleetwood, S. Beyne, R. Jiang, S.E. Zhao, P. Wang, S. Bonaldo, M.W. McCurdy, Z. Tokei, I. Dewolf, K. Croes, E.X. Zhang, M.L. Alles, R.D. Schrimpf, R.A. Reed, and D. Linten, *Applied Physics Letters* **2019**, 114, 203501.

25.   S. Ghosh, K. Fu, F. Kargar, S. Rumyantsev, Y. Zhao, and A.A. Balandin, *Applied Physics Letters* **2021**, 119, 243505.

26.   A. A. Balandin, Noise and Fluctuations Control, *American Scientific Publishers* **2002**, 258.

27.   A. Szewczyk, Ł. Gaweł, K. Darowicki, and J. Smulko, *Energies* **2021**, 14, 8340.

28.   Z. Gingl, C. Pennetta, L.B. Kiss, and L. Reggiani, *Semiconductor Science and Technology* **1996**, 11, 1770.

29.   J. Xu, D. Abbott, and Y. Dai, *Microelectronics Reliability* **2000**, 40, 171.

30.   B.K. Jones, *IEEE Proceedings-Circuits, Devices and Systems* **2002**, 149, 13.

31.   M. V. Hauf, L.H. Hess, J. Howgate, M. Dankerl, M. Stutzmann, and J.A. Garrido, *Applied Physics Letters* **2010**, 97, 093504.

32.   J. Wu, T. Tshepe, J.E. Butler, and M.J.R. Hoch, *Physical Review B - Condensed Matter and Materials Physics* **2005**, 71, 113108.

33.   V.S. Bormashov, S.A. Tarelkin, S.G. Buga, M.S. Kuznetsov, S.A. Terentiev, A.N. Semenov, and V.D. Blank, *Diamond and Related Materials* **2013**, 35, 19.

34.   F. A. Koeck, M. Benipal, R. J. Nemanich, *Diamond and Related Materials* **2020**, 101 107607.

35.   P. Mark and W. Helfrich, *Journal of Applied Physics* **1962**, 33, 205.

36.   S. Ghosh, F. Kargar, A. Mohammadzadeh, S. Rumyantsev, and A.A. Balandin, *Advanced Electronic Materials* **2021**, **7**, 2100408.

37.   A. Mohammadzadeh, A. Rehman, F. Kargar, S. Rumyantsev, J.M. Smulko, W. Knap, R.K. Lake, and A.A. Balandin, *Applied Physics Letters* **2021**, 118, 223101.

38.   A. Geremew, C. Qian, A. Abelson, S. Rumyantsev, F. Kargar, M. Law, and A.A. Balandin, *Nanoscale* **2019**, 11, 20171.

39.   L. Dobrzanski and W. Strupinski, IEEE Journal of Quantum Electronics 43, 188 **2007**.

40.   G. Cywiński, K. Szkudlarek, P. Kruszewski, I. Yahniuk, S. Yatsunenko, G. Muzioł, C. Skierbiszewski, W. Knap, and S.L. Rumyantsev, *Applied Physics Letters* **2016**, 109, 033502.

41.   S.L. Rumyantsev, A.P. Dmitriev, M.E. Levinshtein, D. Veksler, M.S. Shur, J.W. Palmour, M.K. Das, and B.A. Hull, *Journal of Applied Physics* **2006**, 100, 064505.

42.   J.S. Lundh, D. Shoemaker, A.G. Birdwell, J.D. Weil, L.M. de La Cruz, P.B. Shah, K.G. Crawford, T.G. Ivanov, H.Y. Wong, and S. Choi, *Applied Physics Letters* **2021**, 119, 143502.

43.   V.D. Blank, V.S. Bormashov, S.A. Tarelkin, S.G. Buga, M.S. Kuznetsov, D. v. Teteruk, N. V. Kornilov, S.A. Terentiev, and A.P. Volkov, *Diamond and Related Materials* **2015**, 57, 32.

44.   V. Turin, A.A. Balandin, *Electronics Letters* **2004**, 40, 81.

45. S. Sawyer, S.L. Rumyantsev, M.S. Shur, N. Pala, Y. Bilenko, J.P. Zhang, X. Hu, A. Lunev, J. Deng, and R. Gaska, *Journal of Applied Physics* **2006**, 100, 034504.

46. A. L. McWhorter and R. H. Kingston, *Semiconductor Surface Physics*, Univ. of Pennsylvania Press **1957**.

47. N. V. D'yakonova, M.E. Levinshtein, and S.L. Rumyantsev, *Soviet Physics Semiconductors* **1991**, 25, 1241.

48. J.A. Jiménez Tejada, A. Godoy, A. Palma, and P. Cartujo, *Journal of Applied Physics* **2001**, 90, 3998.

49. S. Sawyer, S.L. Rumyantsev, and M.S. Shur, *Solid-State Electronics* **2008**, 52, 968.

50. S. Bychikhin, D. Pogany, L.K.J. Vandamme, G. Meneghesso, and E. Zanoni, *Journal of Applied Physics* **2005**, 97, 123714.

4   Low-Frequency Electronic Noise Measurements of Quasi-2D van der Waals Antiferromagnetic Semiconductor

4.1   Introduction

Transition-metal phospho-trichalcogenides, MPX_3, where M is a transition metal *e.g.* V, Mn, Fe, Co, Ni, or Zn and X is a chalcogenide as S, Se, Te, have recently attracted a lot of attention [1-6]. These layered quasi-two-dimensional (2D) van der Waals (vdW) compounds have interesting electronic, optical, and magnetic properties that can offer new device functionalities [7-19]. It has been demonstrated that some MPX_3 thin films are one of the rare few-layer vdW materials, which can have stable intrinsic antiferromagnetism (AF) even at mono- and few-layer thicknesses [20-22]. The existence of weak vdW bonds between the MPX_3 layers makes them potential candidates for the 2D spintronic devices. The metal element of the MPX_3 materials modifies the band gap from a medium band gap of ~1.3 eV to a wide band gap of ~3.5 eV [1-3]. The diverse properties of these materials tunable by proper selection and combination of the M and X elements make the MPX_3

materials an interesting platform for fundamental science and practical applications [1-4, 23-30].

Among MPX_3 materials, $FePS_3$ is particularly promising. Its Ising-type ordering allows it to maintain the bulk-like magnetic behavior down to a single monolayer, which explains its moniker - "magnetic graphene" [31]. The cleavage energy of $FePSe_3$ is slightly higher than that of graphite, while that for all other combinations of the M and X elements is lower than that of graphite [32]. The Néel temperature, T_N, for $FePS_3$ is reported to be around 118 K [1,2,20]. It shows strong magnetic anisotropy [15,33,34]. In the crystal, each Fe atom is ferromagnetically coupled with two of its neighbors, but the layer is antiferromagnetically coupled with nearest layers making it a zigzag-AF (z-AF) material [1]. The semiconducting nature of $FePS_3$, with the energy band gap of 1.5 eV, and a possibility of the strain engineering of electron and phonon band-structure create additional means for the control of both electron and spin transport [9,17,35]. The quantized spin waves, *i.e.*, magnons in $FePS_3$, have frequencies in the terahertz (THz) frequency range [36,37], which makes this material interesting for THz magnonic devices. However, the electron and spin transport properties of $FePS_3$ have not been studied in sufficient details yet to assess the potential of such materials for THz applications.

In this dissertation chapter, we report the results of investigation of low-frequency current fluctuations, *i.e.* electronic noise, in thin films of antiferromagnetic semiconductor, $FePS_3$. The current-voltage (I-V) and noise characteristics were measured as a function of

temperature to understand their evolution below the room temperature (RT) and, particularly in the vicinity of the Néel temperature of the transition from paramagnetic (PM) to AF ordering. The knowledge of the low-frequency noise is important for assessing the quality of the material and its prospects for any electronic, spintronic or sensor application [38,39]. The noise spectral density and its dependence on external stimuli, *e.g.* electrical bias and temperature, can shed light on electron transport, carrier recombination mechanisms and, what is most important in this case, magnetic and metal-insulator phase transitions [40-46]. We have previously used successfully the low-frequency noise measurements as the "noise spectroscopy" for monitoring phase transitions in the 2D charge-density-wave materials [47-49]; examining the specifics of magnon transport in magnetic electrical insulators [50]; and clarifying the nature of electron transport in quasi-one-dimensional (1D) vdW materials [51,52]. Our measurements of noise in thin films of $FePS_3$ reveal a number of interesting features, which contribute to a better understanding of the properties of this AF vdW semiconductor.

4.2 Material Characterization and Test Device Preparation

For this study, we used high-quality single crystals of $FePS_3$, purchased from commercial vendor (HQ Graphene), which were synthesized by the chemical vapor deposition (CVD) process. The crystals had background *p*-type doping. Figure 4-1 (a) shows the schematic of the monoclinic atomic crystal structure of $FePS_3$ with C2/m symmetry. The Fe, P, and S

atoms are indicated by the violet, green and yellow circles, respectively. The red and violet arrows indicate the up and down directions of the z-AF spin ordering [1,20]. The X-ray diffraction (XRD) and Raman spectroscopy were used to verify the material composition and crystal structure (see Figures 4-1 (b) and (c)). The Raman spectra were taken in the backscattering configuration under 488 nm laser excitation. It is known that $FePS_3$ crystal contains 30 irreducible zone center phonons at Γ point of the first Brillouin zone: $\Gamma = 8A_g$ $+6A_u + 7B_g + 9B_u$, among which only the A_g and B_g modes are Raman active [53,54]. The Raman active modes can be classified into the high-frequency phonon modes, which belong to the internal vibrations of the $(P_2S_6)^{4-}$ anions, and the low-frequency phonon modes, typically below 200 cm^{-1}, which correspond to the interaction of the transition metals (Fe) with both the P and S atoms In our measured Raman spectrum, we were able to observe seven Raman frequency peaks: 98 cm^{-1} (A_g, B_g), 158 cm^{-1} (A_g, B_g), 226 cm^{-1} (A_g, B_g), 247 cm^{-1} (A_g), 279 cm^{-1} (A_g, B_g), 380 cm^{-1} (A_g) and 579 cm^{-1} (A_g). The sharp peak at 520 cm^{-1} comes from the Si/SiO_2 substrate. The obtained Raman data are in line with the literature reports attesting to the quality of the crystals [6,20,53-57].

The test structures were prepared by mechanically exfoliating bulk crystals onto a Si/SiO_2 substrate with the oxide thickness of 300 nm. The uniform and relatively thick layers (200 nm – 400 nm) of the exfoliated layers were chosen in order to compensate for the high resistivity of the material and increase the current level in the device channels required for reliable noise measurements. We employed the electron beam lithography (EBL) to fabricate the devices for the noise measurements. The Si/SiO_2 substrates containing
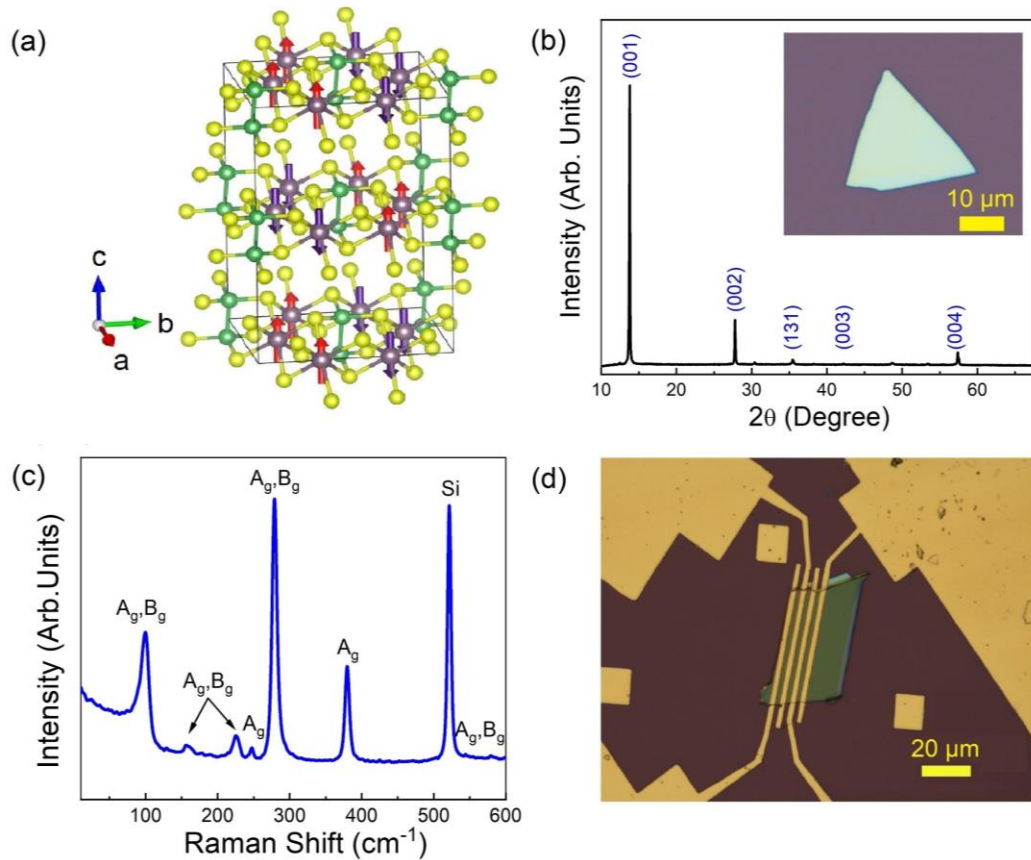
Figure 4-1: Material characteristics and test structure. (a) Crystal structure of bulk $FePS_3$ material. (b) The XRD data for the FePS3 crystal. The inset shows an optical image of a representative crystal. (c) Raman spectrum of the exfoliated FePS3 film on Si/SiO2 substrate. The Raman data were accumulated under 488-nm laser excitation at room temperature. (d) Optical microscopy image of the fabricated test structure, containing four Cr/Au contacts. Reprinted with permission from S. Ghosh et al., Advanced Electronic Materials. 2021, 7, 2100408, Copyright © 2021, Wiley-VCH GmbH.

mechanically exfoliated $FePS_3$ flakes were spin coated with layers of A4 PMMA in a photo-resist spin coat station. The resist coated layers were then placed inside an EBL system (Leo SUPRA 55 SEM/EBL). The predesigned patterns were written on the surface

of the substrates. Once completed, the substrates were developed with a standard solution. After that the metals (Cr/Au) were deposited using an electron beam evaporator tool (Temescal BJD 1800) to create the contact electrodes. The contacts were prepared with 2-µm distance between the nearest contacts. The optical microscopy image of the tested device is shown in Figure 4-1 (d). The thickness of the channel of this device structure was determined with the atomic force microscopy (Dimension 3100).

4.3   Experimental Results and Discussions

Two terminal I-V characteristics of the fabricated device were measured in vacuum inside a cryogenic probe station (Lake Shore TTPX) in the temperature range from room temperature down to ~ 110 K. Figure 4-2 (a) shows the I-V measurement plots at lower bias voltages ($\leq$ 5 V) between 300 K and 150 K where the IV curves are nearly linear. Figure 4-2 (b) shows measured I-V curves at different temperatures at the extended voltage regimes, in the range from room temperature down to 110 K. The I-V plots in semi-logarithmic scale are presented in Figure 4-2 (c). The I-V characteristics are nearly linear at small bias voltage as discussed above but became non-linear for voltages above 10 V. Similar non-linear I-Vs have been reported for other MPX_3 materials [25-27,58,59]. The study, which reported linear I-Vs for $FePS_3$ devices, was limited to the lower voltage regimes [60]. The exact nature of the non-linearity at high bias voltage is still an open question. While some studies attributed it to the formation of the Schottky barriers at the junction between the channel and the metal contacts [25-27,58], the I-V characteristics of

our devices plotted in semi-logarithmic scale (see Figure 4-2 (c)) suggest deviation from the conventional Schottky barrier thermionic model. Other possible reasons for non-linearity can be related to both intrinsic properties of this material as well as to such effects as surface charge accumulation under high electric bias. The local Joule heating does not seem to be a likely mechanism due to the small level of the electric currents even though MPX_3 materials have low thermal conductivity, which can be further reduced in thin films owing to the phonon – boundary scattering [6]. One can also see from Figures 4-2 (b - d) that the resistivity of the $FePS_3$ channel is the smallest at the highest temperature and increases as the temperature is reduced. This is expected owing to the stronger thermal generation of the charge carriers at higher temperatures, which increases the concentration of free carriers contributing to the current [61]. The increase in the resistivity appears to be particularly strong as the temperature reduces below T=200 K. Similar temperature dependence of resistivity in such material has been reported previously [11,62].

The low-frequency noise measurements of the fabricated $FePS_3$ devices were carried out using an in-house experimental setup. The schematic of the setup is shown in Figure 4-3 (a). The equipment consists of six 12 V batteries, with the low internal noise, connected in
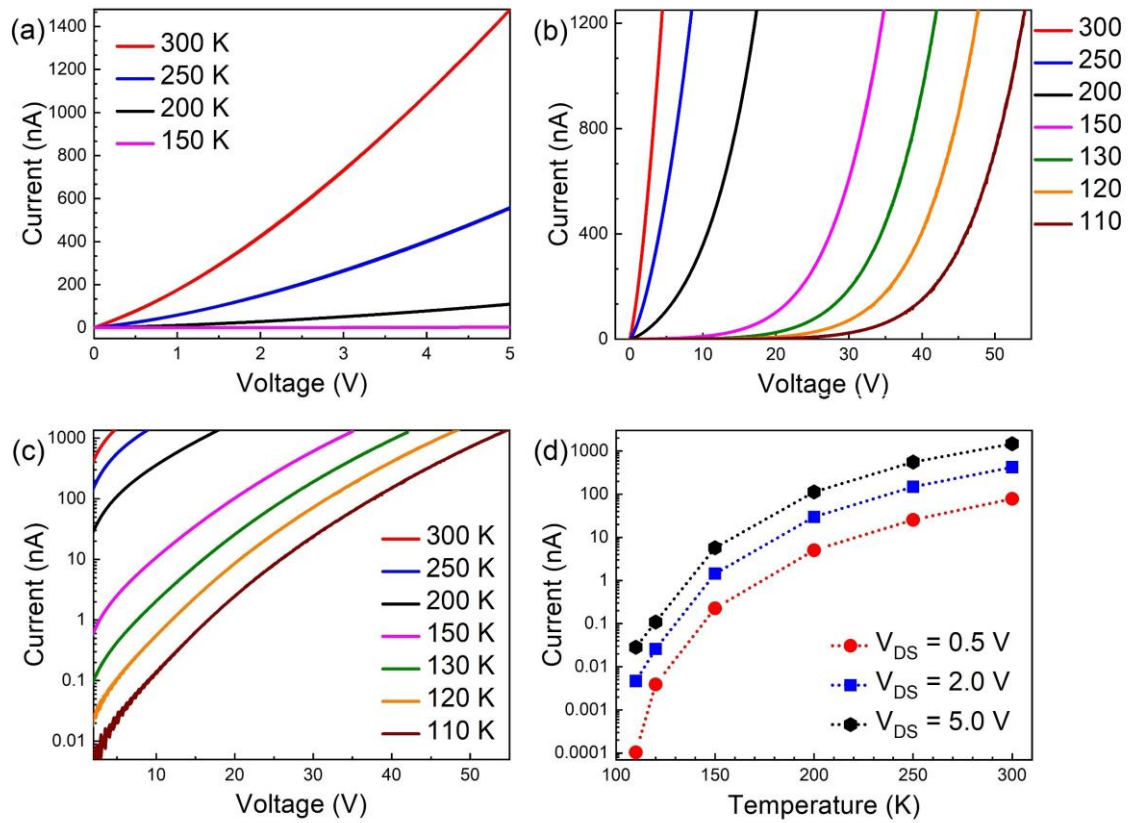
Figure 4-2: Current-voltage characteristics of $FePS_3$ antiferromagnetic semiconductor. (a) Current-voltage characteristics of the $FePS_3$ test structure measured at low voltage bias ($\leq 5V$) in the temperature range from 150 K to 300 K. The I-V plots are almost linear at low voltages. The current at 150 K is small due to the high resistance of the $FePS_3$ channel. (b) Current-voltage characteristics of the same test structure over extended bias range, measured in the temperature range from 110 K to 300 K. (c) The same characteristics as in panel (b) but shown in the semi-log scale. The non-linearity of I-V characteristics is pronounced at large biases. The resistance of the material increases with decreasing temperature. (d) The current through the $FePS_3$ channel as a function of temperature at fixed bias voltage. Reprinted with permission from S. Ghosh et al., Advanced Electronic Materials. **2021**, 7, 2100408, Copyright © 2021, Wiley-VCH GmbH.

58

series to supply a maximum of 72 V bias to the system; a potentiometer to control the voltage drop across the circuit; a load resistor; a low noise voltage preamplifier; and a dynamic signal analyzer. The batteries were intentionally used as the voltage source instead of connecting the system directly to the DC power source in order to minimize the effect of 60 Hz power line frequency and its harmonics. Details of low-frequency noise measurement protocol are described in chapter 1 and in prior reports in the context of other materials systems [47-49,51,52,63-69]. Measuring low-frequency noise in conductors with high electrical resistivity is challenging – one needs to have a sufficient current level to obtain reliable data. From the other side, one typically prefers to use the linear region of the I-V characteristics for biasing the device during the noise measurements.

The low-frequency noise measured at RT for different bias voltages, V_D, varying from 0.14 V to 3.73 V is shown in Figure 4-3 (b). The voltage-referred noise-power spectral density, S_V, reveals the typical flicker noise trend, $S_V \sim 1/f^\gamma$, where f is the frequency and parameter $\gamma \approx 1$. The $1/f$ noise is typical for many semiconductor and metallic materials [70]. We verified that the $1/f$ noise level at the lowest applied bias is more than an order of magnitude higher than the background noise of the measurement system, confirming that the spectra in Figure 4-3 (b) are indeed resulting from the current fluctuations in the device under test. Figure 4-3 (c) presents the current noise-power spectral density, S_I, as a function of current, I_D, at different temperatures. The data are shown at fixed frequency $f = 10$ Hz. In general, the dependence of S_I on the device current I_D is expected to be quadratic, *i.e.* $S_I \sim I_D^2$, so that the slope in the S_I *vs* I_D plot is close to 2. It is observed in various materials where the

noise is $1/f$ type, without the superimposed G-R bulges [49,52,63]. In our measurements the $S_I(I_D)$ dependence at different temperatures does not show a perfect quadratic scaling, Instead, we obtained $S_I(I_D) \sim I_D^\zeta$ where parameter ζ is in the range between from 1.49 to 2.15. We attribute this deviation to the non-linearity of I-V characteristics in the tested devices. The deviation from the $S_I \sim I_D^2$ law is an indication that noise properties of the device depend on the applied bias. This is a typical behavior for devices with non-linear current-voltage characteristics [25-27,58,59]. Since the non-linearity of the I-V characteristics is not related to the contacts, as discussed above, the deviation from the quadratic $S_I \sim I_D^2$ dependence is attributed to the material itself. It is not related to any current induced damage in the devices, *e.g.* onset of electromigration owing to the small current levels used in the measurements. The reproducibility of the noise data also attests to the absence of any damage during the measurements.

The normalized noise-power spectral densities, S_I/I^2, as a function of frequency at different temperatures are presented in Figure 4-3 (d). These spectra were measured at a fixed current through the channel, $I \equiv I_D = 50$ nA. The noise measurements were intentionally carried out at the smallest current level to avoid even small Joule heating of the channel near the expected phase transition temperature points. At low temperatures, the measurements were conducted at 2-K interval in order to examine the effect of transition from PM to AF phase at the Néel temperature of 118 K. The spectra show the $1/f$ noise as temperature decreases from 300 K to 130 K. As it approaches $T_N = 118$ K, the spectrum develops pronounced Lorentzian bulges. The spectral position of the Lorentzian bulges
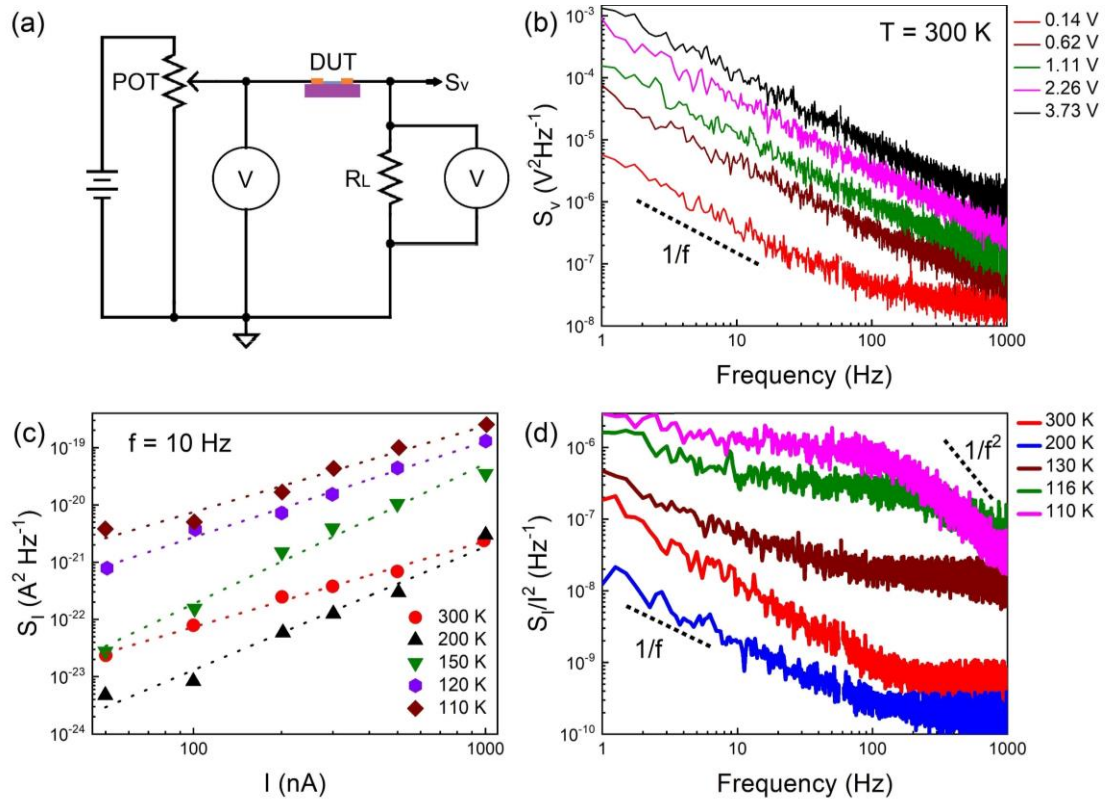
Figure 4-3: Low-frequency noise spectra of FePS$_3$ thin films. (a) Schematic of the noise measurements showing the biasing of the device under test (DUT). (b) The voltage-referred noise spectral density, S_V, as a function of frequency measured for different bias voltage at room temperature. (c) The current noise spectral density, S_I, as a function of the channel current at different temperatures and fixed frequency f=10 Hz. (d) The normalized current noise spectral density, S_I/I^2, as a function of frequency at different temperatures. The noise was measured at the constant channel current $I_D = 50$ nA. Note the appearance of Lorentzian bulges at low temperatures. Reprinted with permission from S. Ghosh et al., Advanced Electronic Materials. **2021**, 7, 2100408, Copyright © 2021, Wiley-VCH GmbH.

reveals a pronounced dependence on temperature. Appearance of the Lorentzian bulges

near the characteristic Néel temperature of PM – AF phase transition and their strong

temperature dependence constitute additional proof that the noise is associated with FePS$_3$

material, and not with the contacts. This also excludes the possibility of a typical cutoff of the noise spectrum due to the amplifier used for signal acquisition.

The Lorentzian shape of the noise spectrum at T=120 K and below can be described by the equation $S_I(f) = S_0 \times (f_c^2/(f^2 + f_c^2))$ where f_c is the corner frequency of the spectrum defined as $f_c = (2\pi\tau)^{-1}$, S_0 is the frequency independent portion of the function $S_I(f)$ when $f < f_c$ and τ represents the characteristic time constant [48,51]. In most cases, the emergence of the Lorentzian bulges in semiconductor devices is associated with the generation – recombination (G-R) noise, which is conventionally interpreted as evidence that the material does have high concentration of certain defects, which would dominate the noise properties [70]. However, this is not the only possible origin of the Lorentzian bulges. They can also be related to various phase transitions that material is undergoing under changing temperature or applied electrical bias [48,49,51]. We have previously observed Lorentzian spectra associated with the charge-density-wave (CDW) phase transitions [48,49], magnon transport in electrically insulating materials [50], and electron transport in bundles of quasi-1D vdW materials [51]. The noise mechanisms leading to the appearance of Lorentzian bulges, which are associated with the phase transitions, are completely different from that of the G-R trapping noise.

To further analyze the effect of temperature and applied bias on the noise spectra, we plotted the normalized noise-power spectral density, S_I/I^2, multiplied by the frequency, *i.e.* $f \times S_I/I^2$ *vs.* f. This procedure helps to separate the Lorentzian features from the $1/f$

background. Figure 4-4 (a) how the maxima, which correspond to the corner frequencies, f_c, are shifting with the temperature. The data are presented for $I_D = 50$ nA. Figure 4-4 (b) presents $f \times S_I / I^2$ vs. f for the fixed temperature T=110 K and varied channel current, I_D. For each spectrum, we determine the corner frequency by numerical fitting. The corner frequency, f_c, at different currents, is shown as a function of $1000/T$ in Figure 4-4 (c). It increases strongly near the Néel temperature and follows the same trend across all currents. The corner frequency values at 118 K and 120 K for higher currents are out of the measured frequency range. From the Arrhenius plot of $ln(f_c)$ vs. $1000/T$ in Figure 4-4 (c), we have also extracted the "noise activation" energy, E_A, to be 0.9 eV for this material. In semiconductors, this activation energy is usually associated with the exponential dependence of the characteristic emission time from the trap level to conduction or valence bands $\tau_e \propto \exp\left(-E_A/KT\right)$ [71]. However, this activation energy is unrealistically large for a semiconductor with the 1.5-eV energy bandgap. The latter confirms our conclusion that the Lorentzian noise bulges are not of G-R charge carrier trapping - de-trapping origin. Since the Lorentzian bulges were observed at temperatures close to the Néel temperature we argue that these spectral features are associated not with the GR noise but with the PM – AF phase transition. The additional evidence for this conclusion comes from the fast increase of the corner frequency with the applied bias voltage (see Figure 4-4 (d)). Such a strong dependence of f_c on V_D is unusual for conventional trapping G-R noise. However, it is common in CDW materials where Lorentzian bulges appear at the nearly commensurate to incommensurate CDW phase transition [47-49].
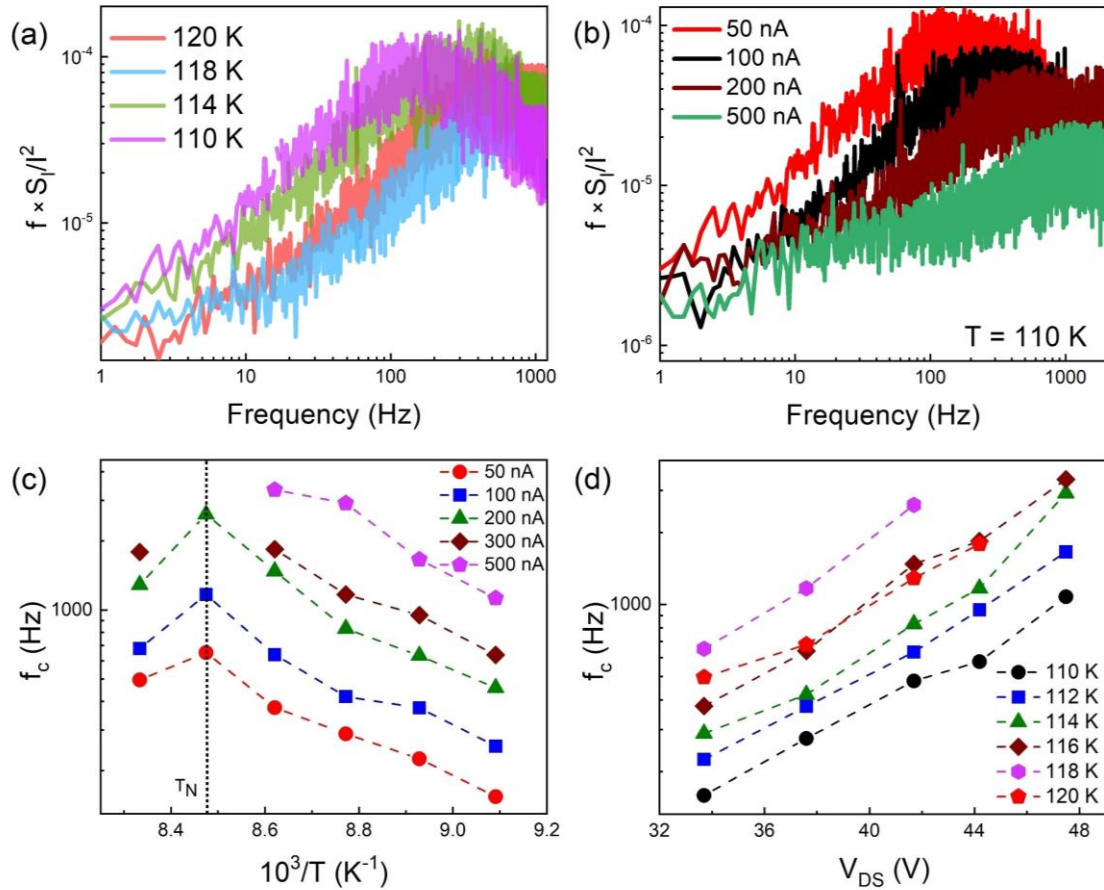
Figure 4-4: Lorentzian spectral features in the noise spectra. (a) The normalized noise spectral density multiplied by the frequency, $S_I/I^2 \times f$, as a function of frequency measured near the Néel temperature at the constant channel current I_D=50 nA. (b) The normalized noise spectral density multiplied by the frequency, $S_I/I^2 \times f$, as a function of frequency measured for different channel currents at a fixed temperature T=110 K. (c) The corner frequency, f_c, of the Lorentzian noise components as function of the inverse temperature, $1000/T$, measured at different channel currents. The corner frequency attains its highest value at the Néel temperature T_N=118 K. The dashed lines are guides for the eye. (d) The corner frequency, f_c, of the Lorentzian noise components as function of the applied bias voltage measured at different temperatures. Note the strong dependence of the corner frequency on temperature and bias voltage. Reprinted with permission from S. Ghosh et al., Advanced Electronic Materials. **2021**, 7, 2100408, Copyright © 2021, Wiley-VCH GmbH.

Figures 4-5 (a) and (b) show the current fluctuations, *i.e.* noise, in the time-domain near the Néel temperature and high temperature, respectively. The large sharp peaks in both figures are due to the external electromagnetic influence since they were also observed without the electrical bias. These features should be ignored in the analysis. As one can see in Figure 4-5 (a), the noise has the form of the pulses with nearly constant amplitudes and random duration and intervals between the pulses. The amplitude of the pulses depends only weakly on temperature. This type of current fluctuations is referred to as the random telegraph signal (RTS) noise. The RTS noise appears when only one fluctuator within the whole sample is responsible for noise [50,72,73]. Since the assumption that the macroscopic sample includes only one charge carrier trap, which contributes to noise, is not realistic, the existence of the RTS noise is a further proof that this noise, and the corresponding Lorentzian bulges in the frequency domain, are associated with the phase transition. The RTS noise disappears at higher temperatures (Figure 4-5 (b)), which is in line with our explanation. Our conclusions are further supported by the analogies in the noise features which we have observed near phase transitions in the CDW materials [48,49]. One can envision the use of the low-frequency noise measurements for the noise spectroscopy of various phase transitions in different types of materials. In this regard, the noise can be interpreted as a signal similar to the fluctuation-enhanced sensing [74].
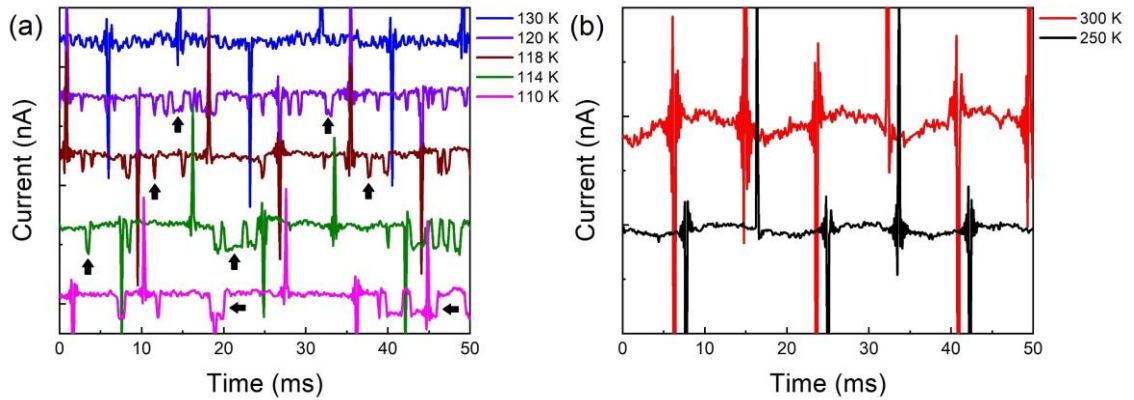
Figure 4-5: Current fluctuations in the time domain. (a) The time-domain noise spectra near the Néel temperature. The current fluctuations measured in the temperature range from 110 K to 120 K reveal clear signatures of the random telegraph signal noise. The black arrows indicate representative RTS pulses at each temperature. (b) The time-domain noise spectra near the room temperature. No random telegraph signal noise is observed. Note that in both panels, the large spikes are due to the electromagnetic interference and should be ignored in the data analysis. Reprinted with permission from S. Ghosh et al., Advanced Electronic Materials. **2021**, 7, 2100408, Copyright © 2021, Wiley-VCH GmbH.

We now look closely at the evolution of the normalized noise spectral density, S_I/I^2, as a function of temperature (see Figures 4-6 (a-d)). One can see a consistent trend at every frequency and current through the device channel. At $T < 200$ K, the noise increases as the temperature decreases and reaches the Néel transition temperature to AF phase. One can expect that the noise will be close to its maximum value near the phase transition temperature, in this case, from PM to AF phase. At this point, the material system is undergoing structural change, often characterized by an increased disorder and, as a result, increased electronic noise. The increased noise can also be associated with abrupt changes in the resistance and instability of the characteristics of the material at the phase transition. In general, it is possible that a maximum in the noise should signal a phase transition [47-

49,75-79]. Prior studies indicate that the noise increases in the vicinity of the metal-insulator transition [75], spin glass transition [76,77], and other various phase transitions [78,79].
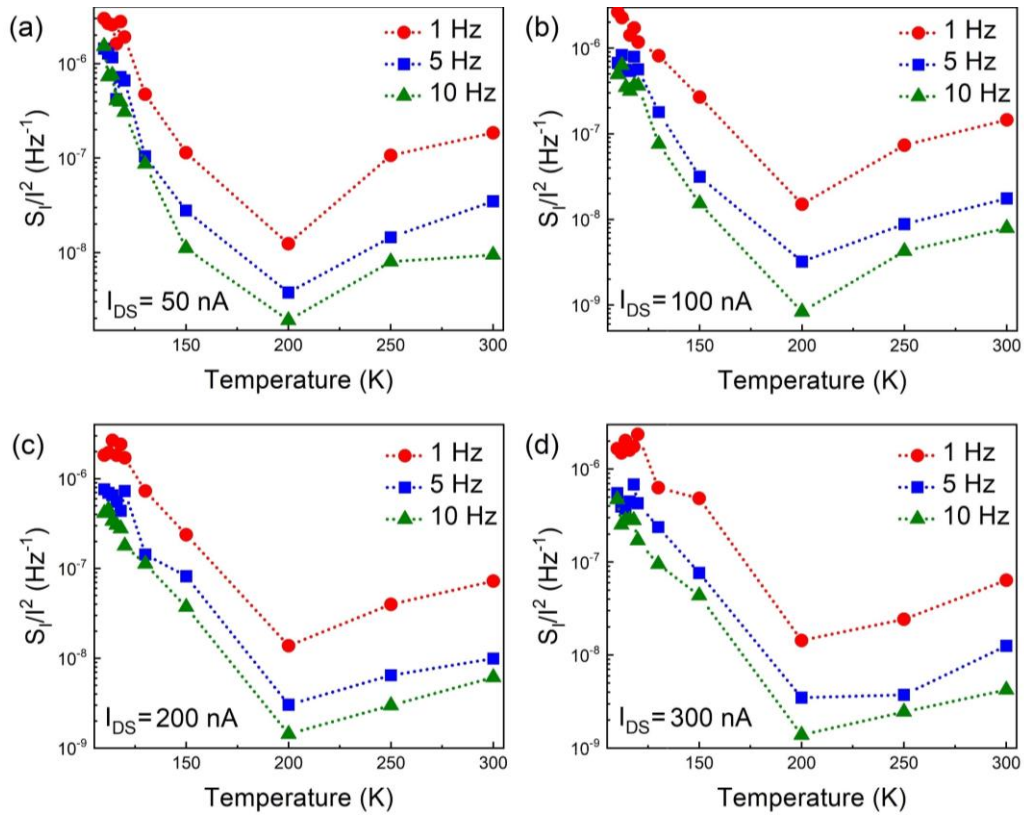
Figure 4-6: Noise evolution with temperature. The normalized current noise spectral density as a function of temperature plotted for three different frequencies f=1 Hz, 5 Hz and 10 Hz. The data are presented for several fixed current levels, I_D, to demonstrate the consistency and reproducibility: (a) 50 nA, (b) 100 nA, (c) 200 nA and (d) 300 nA. The noise level attains its maximum near the Néel temperature. The non-monotonic dependence of noise spectral density on temperature is likely related to an interplay of two opposite trends in noise scaling – one for semiconductors and another for materials with the phase transitions. Reprinted with permission from S. Ghosh et al., Advanced Electronic Materials. **2021**, 7, 2100408, Copyright © 2021, Wiley-VCH GmbH.

The noise temperature dependence at around T=200 K, where it attains minimum, is intriguing (see Figures 6 (a-d)). Previously, this temperature was identified as a possible Mott metal – insulator transition point for FePS$_3$ [11,62]. The latter was established *via* measurements that involved an application of high pressure [11,62]. One would expect a noise increase at the metal – insulator transition. To explain the noise minimum near 200 K, we consider the following physical mechanism. The conventional models of the low-frequency noise in semiconductors predict the noise magnitude proportional to temperature. For example, in McWhorter's theory, the noise spectral density scales with temperature as $S_I \sim k_B T$ (here k_B is the Boltzmann constant) [80]. This explains the decrease of the noise with the temperature decrease from 300 K to 200 K. The increase in the noise level with the further temperature decrease is associated with the early effect of the phase transition at Néel temperature. In this scenario, the position of the noise minimum is an interplay of two trends – one is the noise temperature dependence typical for semiconductors and the other one is the noise increase near the phase transition point. There have been reports of a similar trend in electrical noise from the spin fluctuations *vs.* temperature in CuMn [76] and Cr [77]. While noise scaling in metals is more complicated one can envision a similar interplay resulting in non-monotonic dependence of noise on temperature.

4.4 Conclusions

In conclusion, we investigated low-frequency noise in the quasi-2D van der Waals AF semiconductor FePS$_3$ with the electronic bandgap of 1.5 eV. The noise spectral density was of the 1/f-type over most of the examined temperature range but reveals well-defined Lorentzian bulges, and it increases strongly near the Néel temperature T_N =118 K. Intriguingly, the noise spectral density attained its minimum at temperature T~200 K, which is likely related to an interplay of two opposite trends in the noise scaling – one is the noise decrease following the dependence S_I~$k_B T$, as observed in conventional semiconductors, and another one is the noise increase for materials with the phase transitions. This explains the noise reduction with the temperature decreasing from 300 K to 200 K, and noise increase with further decrease in temperature associated with the early effect of the phase transition at Néel temperature. The noise spectra revealed well-defined Lorentzian bulges near the Néel temperature T_N=118 K. The Lorentzian corner frequencies depend strongly on temperature and bias voltage, suggesting that their origin is different from the conventional generation – recombination noise. The observed Lorentzian spectral features are signatures of the AF phase transitions rather than electron trapping and de-trapping by the defects. The obtained results are important for proposed applications of antiferromagnetic semiconductors in spintronic devices. They also attest to the power of the *noise spectroscopy* for monitoring phase transitions of various nature and in different materials.

References

1. F. Wang, T. A. Shifa, P. Yu, P. He, Y. Liu, F. Wang, Z. Wang, X. Zhan, X. Lou, F. Xia, J. He, *Advanced Functional Materials* **2018**, *28*, 1802151.

2. L. Wang, P. Hu, Y. Long, Z. Liu, X. He, *J. Mater. Chem. A* **2017**, *5*, 22855.

3. R. Samal, G. Sanyal, B. Chakraborty, C. S. Rout, *J. Mater. Chem. A* **2021**, *9*, 2560.

4. Y. Zhang, T. Fan, S. Yang, F. Wang, S. Yang, S. Wang, J. Su, M. Zhao, X. Hu, H. Zhang, T. Zhai, *Small Methods* **2021**, 2001068.

5. C. C. Mayorga-Martinez, Z. Sofer, D. Sedmidubský, Š. Huber, A. Y. S. Eng, M. Pumera, *ACS Applied Materials and Interfaces* **2017**, *9*, 12563.

6. F. Kargar, E. A. Coleman, S. Ghosh, J. Lee, M. J. Gomez, Y. Liu, A. S. Magana, Z. Barani, A. Mohammadzadeh, B. Debnath, R. B. Wilson, R. K. Lake, A. A. Balandin, *ACS Nano* **2020**, *14*, 2424.

7. R. Brec, D. M. Schleich, G. Ouvrard, A. Louisy, J. Rouxel, *Inorganic Chemistry* **1979**, *18*, 1814.

8. Y. V. Kuzminskii, B. M. Voronin, N. N. Redin, *Journal of Power Sources* **1995**, *55*, 133.

9. B. L. Chittari, Y. Park, D. Lee, M. Han, A. H. Macdonald, E. Hwang, J. Jung, *Physical Review B* **2016**, *94*, 184428.

10. K. Ichimura, M. Sano, *Synthetic Metals* **1991**, *45*, 203.

11. M. Tsurubayashi, K. Kodama, M. Kano, K. Ishigaki, Y. Uwatoko, T. Watanabe, K. Takase, Y. Takano, *AIP Advances* **2018**, *8*, 101307.

12. H. Xiang, B. Xu, Y. Xia, J. Yin, Z. Liu, *RSC Advances* **2016**, *6*, 89901.

13. P. J. S. Foot, J. Suradi, P. A. Lee, *Materials Research Bulletin* **1980**, *15*, 189.

14. M. Piacentini, F. S. Khumalo, C. G. Olson, J. W. Anderegg, D. W. Lynch, *Chemical Physics* **1982**, *65*, 289.

15. P. A. Joy, S. Vasudevan, *Physical Review B* **1992**, *46*, 5425.

16. A. Ghosh, M. Palit, S. Maity, V. Dwij, S. Rana, S. Datta, *Physical Review B* **2021**, *103*, 064431.

17. J. min Zhang, Y. zhuang Nie, X. guang Wang, Q. lin Xia, G. hua Guo, *Journal of Magnetism and Magnetic Materials* **2021**, *525*, 167687.

18. D. Lançon, H. C. Walker, E. Ressouche, B. Ouladdiaf, K. C. Rule, G. J. McIntyre, T. J. Hicks, H. M. Rønnow, A. R. Wildes, *Physical Review B* **2016**, *94*, 214407.

19. Y. Zheng, X. X. Jiang, X. X. Xue, J. Dai, Y. Feng, *Physical Review B* **2019**, *100*, 174102.

20. J. U. Lee, S. Lee, J. H. Ryoo, S. Kang, T. Y. Kim, P. Kim, C. H. Park, J. G. Park, H. Cheong, *Nano Letters* **2016**, *16*, 7433.

21. K. S. Burch, D. Mandrus, J. G. Park, *Nature* **2018**, *563*, 47.

22. M. Gibertini, M. Koperski, A. F. Morpurgo, K. S. Novoselov, *Nature Nanotechnology* **2019**, *14*, 408.

23. M. Ramos, F. Carrascoso, R. Frisenda, P. Gant, S. Mañas-Valero, D. L. Esteras, J. J. Baldoví, E. Coronado, A. Castellanos-Gomez, M. R. Calvo, *npj 2D Materials and Applications* **2021**, *5*, 1.

24. X. Han, P. Song, J. Xing, Z. Chen, D. Li, G. Xu, X. Zhao, F. Ma, D. Rong, Y. Shi, M. R. Islam, K. Liu, Y. Huang, *ACS Applied Materials and Interfaces* **2021**, *13*, 2836.

25. J. Chu, F. Wang, L. Yin, L. Lei, C. Yan, F. Wang, Y. Wen, Z. Wang, C. Jiang, L. Feng, J. Xiong, Y. Li, J. He, *Advanced Functional Materials* **2017**, *27*, 1701342.

26. R. N. Jenjeti, R. Kumar, M. P. Austeria, S. Sampath, *Scientific Reports* **2018**, *8*, 8586.

27. R. Kumar, R. N. Jenjeti, M. P. Austeria, S. Sampath, *Journal of Materials Chemistry C* **2019**, *7*, 324.

28. R. Kumar, R. N. Jenjeti, S. Sampath, *ACS Sensors* **2020**, *5*, 404.

29. Y. Fujii, A. Miura, N. C. Rosero-Navarro, M. Higuchi, K. Tadanaga, *Electrochimica Acta* **2017**, *241*, 370.

30. C. E. Byvik, B. T. Smith, B. Reichman, *Solar Energy Materials* **1982**, *7*, 213.

31. M. J. Coak, D. M. Jarvis, H. Hamidov, A. R. Wildes, J. A. M. Paddison, C. Liu, C. R. S. Haines, N. T. Dang, S. E. Kichanov, B. N. Savenko, S. Lee, M. Kratochvílová, S. Klotz, T. C. Hansen, D. P. Kozlenko, J. G. Park, S. S. Saxena, *Physical Review X* **2021**, *11*, 011024.

32. K. Z. Du, X. Z. Wang, Y. Liu, P. Hu, M. I. B. Utama, C. K. Gan, Q. Xiong, C. Kloc, *ACS Nano* **2016**, *10*, 1738.

33. Z. ur Rehman, Z. Muhammad, O. Adetunji Moses, W. Zhu, C. Wu, Q. He, M. Habib, L. Song, *Micromachines* **2018**, *9*, 292.

34. M. Nauman, D. H. Kiem, S. Lee, S. Son, J.-G. Park, W. Kang, M. J. Han, Y. J. Jo, *2D Materials* **2021**, *8*, 35011.

35. A. Hashemi, H. P. Komsa, M. Puska, A. v. Krasheninnikov, *Journal of Physical Chemistry C* **2017**, *121*, 27207.

36. McCreary, J. R. Simpson, T. T. Mai, R. D. McMichael, J. E. Douglas, N. Butch, C. Dennis, R. Valdés Aguilar, A. R. Hight Walker, *Physical Review B* **2020**, *101*, 064416.

37. A. R. Wildes, K. C. Rule, R. I. Bewley, M. Enderle, T. J. Hicks, *Journal of Physics Condensed Matter* **2012**, *24*, 416004.

38. G. Scandurra, J. Smulko, L. B. Kish, *Applied Sciences* **2020**, *10*, 5818.

39. J. Smulko, T. Chludziński, U. Çindemir, C. G. Granqvist, H. Wen, *Journal of Sensors* **2020**, *2020*, 1.

40. C. Barone, H. Rotzinger, J. N. Voss, C. Mauro, Y. Schön, A. v. Ustinov, S. Pagano, Nanomaterials **2020**, *10*, 524.

41. U. Chandni, A. Ghosh, H. S. Vijaya, S. Mohan, Physical Review Letters **2009**, *102*, 025701.

42. U. Chandni, A. Ghosh, Physical Review B - Condensed Matter and Materials Physics **2010**, *81*, 134105.

43. C. Barone, S. Pagano, I. Pallecchi, E. Bellingeri, M. Putti, C. Ferdeghini, Physical Review B - Condensed Matter and Materials Physics **2011**, *83*, 134523.

44. S. Pagano, N. Martucciello, E. Enrico, E. Monticone, K. Iida, C. Barone, Nanomaterials **2020**, *10*, 862.

45. M. Kuiri, S. Das, D. V. S. Muthu, A. Das, A. K. Sood, Nanoscale **2020**, *12*, 8371.

46. C. Barone, A. Galdi, N. Lampis, L. Maritato, F. M. Granozio, S. Pagano, P. Perna, M. Radovic, U. Scotti Di Uccio, Physical Review B - Condensed Matter and Materials Physics **2009**, *80*, 115128.

47. K. Geremew, S. Rumyantsev, F. Kargar, B. Debnath, A. Nosek, M. A. Bloodgood, M. Bockrath, T. T. Salguero, R. K. Lake, A. A. Balandin, *ACS Nano* **2019**, *13*, 7231.

48. G. Liu, S. Rumyantsev, M. A. Bloodgood, T. T. Salguero, A. A. Balandin, *Nano Letters* **2018**, *18*, 3630.

49. R. Salgado, A. Mohammadzadeh, F. Kargar, A. Geremew, C. Y. Huang, M. A. Bloodgood, S. Rumyantsev, T. T. Salguero, A. A. Balandin, *Applied Physics Express* **2019**, *12*, 037001.

50. S. Rumyantsev, M. Balinskiy, F. Kargar, A. Khitun, A. A. Balandin, *Applied Physics Letters* **2019**, *114*, 090601.

51. A. K. Geremew, S. Rumyantsev, M. A. Bloodgood, T. T. Salguero, A. A. Balandin, *Nanoscale* **2018**, *10*, 19749.

52. G. Liu, S. Rumyantsev, M. A. Bloodgood, T. T. Salguero, M. Shur, A. A. Balandin, *Nano Letters* **2017**, *17*, 377.

53. X. Wang, K. Du, Y. Y. F. Liu, P. Hu, J. Zhang, Q. Zhang, M. H. S. Owen, X. Lu, C. K. Gan, P. Sengupta, C. Kloc, Q. Xiong, *2D Materials* **2016**, *3*, 031009.

54. M. Scagliotti, M. Jouanne, M. Balkanski, G. Ouvrard, *Solid State Communications* **1985**, *54*, 291.

55. M. Scagliotti, M. Jouanne, M. Balkanski, G. Ouvrard, G. Benedek, *Physical Review B* **1987**, *35*, 7097.

56. K. Kim, J. U. Lee, H. Cheong, *Nanotechnology* **2019**, *30*, 452001.

57. M. Bernasconi, G. L. Marra, G. Benedek, L. Miglio, M. Jouanne, C. Julien, M. Scagliotti, M. Balkanski, Physical Review B **1988**, *38*, 12089.

58. S. Lee, K. Y. Choi, S. Lee, B. H. Park, J. G. Park, *APL Materials* **2016**, *4*, 086108.

59. G. Long, H. Henck, M. Gibertini, D. Dumcenco, Z. Wang, T. Taniguchi, K. Watanabe, E. Giannini, A. F. Morpurgo, *Nano Letters* **2020**, *20*, 2452.

60. Z. Ou, T. Wang, J. Tang, X. Zong, W. Wang, Q. Guo, Y. Xu, C. Zhu, L. Wang, W. Huang, H. Xu, *Advanced Optical Materials* **2020**, *8*, 2000201.

61. V. Grasso, F. Neri, S. Patanè, L. Silipigni, M. Piacentini, *Physical Review B* **1990**, *42*, 1690.

62. R. S. Haines, M. J. Coak, A. R. Wildes, G. I. Lampronti, C. Liu, P. Nahai-Williamson, H. Hamidov, D. Daisenberger, S. S. Saxena, *Physical Review Letters* **2018**, *121*, 266801.

63. A. Geremew, C. Qian, A. Abelson, S. Rumyantsev, F. Kargar, M. Law, A. A. Balandin, *Nanoscale* **2019**, *11*, 20171.

64. M. A. Stolyarov, G. Liu, S. L. Rumyantsev, M. Shur, A. A. Balandin, *Applied Physics Letters* **2015**, *107*, 023106.

65. A. K. Geremew, S. Rumyantsev, B. Debnath, R. K. Lake, A. A. Balandin, *Applied Physics Letters* **2020**, *116*, 163101

66. J. Renteria, R. Samnakay, S. L. Rumyantsev, C. Jiang, P. Goli, M. S. Shur, A. A. Balandin, *Applied Physics Letters* **2014**, *104*, 153104.

67. A. A. Balandin, *Nature Nanotechnology* **2013**, *8*, 549.

68. M. Z. Hossain, S. Rumyantsev, M. S. Shur, A. A. Balandin, *Applied Physics Letters* **2013**, *102*, 153512.

69. M. Z. Hossain, S. L. Rumyantsev, K. M. F. Shahil, D. Teweldebrhan, M. Shur, A. A. Balandin, *ACS Nano* **2011**, *5*, 2657.

70. V. Mitin, L. Regianni, L. Varani, Generation- recombination noise in semiconductors; Balandin, A. A.; Noise and Fluctuations Control in Electronic Devices; American Scientific Publishers Los Angeles, 2002; pp. 12 – 31.

71. M.E. Levinshtein, S.L. Rumyantsev, *Semiconductor Science and Technology* **1994**, *9*, 1183.

72. J. Pavelka, J. Šikula, M. Tacano, M. Toita, *Radioengineering* **2011**, *20*, 194.

73. J. Pavelka, J. Šikula, M. Tacano, *Wseas Tranactions on Electronics* **2007**, *9*, 221.

74. S. Rumyantsev, G. Liu, M. S. Shur, R. A. Potyrailo, A. A. Balandin, *Nano Letters* **2012**, *12*, 2294.

75. J. Jaroszyński, D. Popović, T. M. Klapwijk, *Physical Review Letters* **2002**, *89*, 276401.

76. N. E. Israeloff, M. B. Weissman, G. J. Nieuwenhuys, J. Kosiorowska, *Physical Review Letters* **1989**, *63*, 794.

77. N. E. Israeloff, M. B. Weissman, G. A. Garfunkel, D. J. van Harlingen, J. H. Scofield, A. J. Lucero, *Physical Review Letters* **1988**, *60*, 152.

78.   C. Reichhardt, C. J. O. Reichhardt, *Physical Review Letters* **2004**, *93*, 176405.

79.   O. Cohen, Z. Ovadyahu, *Physical Review B* **1994**, *50*, 10442.

80.   P. Dutta and P. M. Horn, *Reviews of Modern Physics*, **1981**, *53*, 497.

5 Low-Frequency Current Fluctuations in Quasi-1D Weyl Semimetal Nanoribbons

The following chapter (text and figures) has been fully reprinted from the arXiv Preprint:

S. Ghosh, F. Kargar, N. R. Sesing, Z. Barani, T. T. Salguero, D. Yan, S. Rumyantsev, and A. A. Balandin, Low-Frequency Noise in Quasi-1D $(TaSe_4)_2I$ Weyl Semimetal Nanoribbons, arXiv:2208.06476, 2022.

5.1 Introduction to Quasi 1D Weyl Semimetal

Recently, one-dimensional (1D) van der Waals (vdW) quantum materials with emergent topological phases, derived from strongly correlated interactions, have attracted significant attention [1, 3]. A prototype example is a tetra-selenide compound $(TaSe_4)_2I$, with a structure featuring unusual axially chiral $(TaSe_4)_n$ chains [4-7]. At elevated temperatures, this quasi-1D material is defined as a Weyl semimetal with Weyl points located above and below the Fermi level, forming pairs with the opposite chiral charge. At temperatures below the Peierls transition temperature $T_P = 248$ K – 263 K, $(TaSe_4)_2I$ reveals the charge-density-wave (CDW) phase [4, 8-13]. The quantum CDW phase consists of a periodic modulation of the electronic charge density accompanied by a periodic distortion of the atomic lattice, in this case, Ta tetramerization [14-19]. It has been suggested that $(TaSe_4)_2I$ reveals a correlated topological phase, which arises from the formation of CDW in a Weyl

semimetal [11, 12]. This quasi-1D quantum material represents an interesting avenue for exploring the interplay of correlations and topology, as well as being an exciting system for examining new functionalities and electronic applications [17, 20].

There is an interesting, applied physics aspect in the research of topological semimetals. The resistance and current density bottlenecks in downscaled metal interconnect motivate the search for new materials for the back end of the line (BEOL) interconnect applications [21, 22]. When the interconnect linewidth scales below the electron mean free path, its resistivity increases in a power-law function due to increased electron scattering from interfaces and grain boundaries [23, 24]. This problem is persistent for all *elemental* metals, including Cu, Co, and Ru. Quasi-1D vdW materials demonstrated different dependencies where the resistivity remained nearly constant with the scaling of the interconnect cross-sectional area due to their single-crystal nature and sharp vdW boundary interfaces [25, 26]. There are indications that in some topological semimetals, the electrical conductivity can actually increase as the cross-sectional area decreases. Recent studies have shown that in the topological Weyl semimetal NbAs the resistivity can decrease by an order of magnitude from 35 μΩ-cm in bulk single crystals to 1–5 μΩ-cm in ~200 nm nanoribbons [27]. For this reason, a better understanding of electron transport phenomena in Weyl semimetals can have an immediate practical significance for interconnect applications [28, 29].

In this chapter, we discuss on the low-frequency current fluctuations, *i.e.*, low-frequency electronic noise, also referred to as *excess* noise, in $(TaSe_4)_2I$ nanoribbons. The low-frequency noise includes the $1/f$ and generation-recombination (G-R) noise with a Lorentzian type spectrum, which comes on top of the thermal and shot noise background (f is the frequency). It is known that $1/f$ noise can provide information on the electron transport and charge carrier recombination in a given material, as well as serve as an early indicator of electromigration damage [30-35]. We have previously used low-frequency noise measurements for monitoring phase transition in various materials [36-39] as well as for assessing the material quality and device reliability [40-42]. In this work, we are primarily motivated by the following questions. Is electron transport in the topological Weyl semimetals characterized by inherently lower noise owing to the suppression of certain electron scattering channels? Can one use the excess noise data to verify the CDW transitions in the topological Weyl semimetals? We are also interested in assessing if Weyl semimetals are acceptable for interconnect applications in terms of their electronic noise level.

5.2 Growth and Characterization of Bulk Materials

The bulk material was provided by Prof. Tina T. Salguero's research group from the University of Georgia. The crystal structure of quasi-1D $(TaSe_4)_2I$ above T_P is illustrated in Figure 5-1 (a) with a view showing $(TaSe_4)_n$ chains aligned along the *c*-axis, within an

iodide lattice [43]. The view of a single $(TaSe_4)_n$ chain highlights several key features, including the coordination of each Ta center to eight selenium atoms in rectangular anti-prismatic geometry, the equidistant Ta centers at ~3.2 Å that support metallic bonding, the slightly asymmetric bridging of Se_2^{2-} pairs between Ta centers, in part due to interactions with iodide, and most notably, the rotating pattern of Se_2^{2-} about the chain axis that generates axial chirality. Single crystal $(TaSe_4)_2I$ source materials were synthesized by the chemical vapor transport (CVT) method from stoichiometric amounts of tantalum and selenium, and an excess of iodine that serves as both reactant and transport agent. For the crystal synthesis, 0.3188 g (2.512 mmol) of I_2 crystals (JT Baker, 99.9%) were placed at the bottom of a ~18 × 1 cm nitric acid-cleaned and dried fused quartz ampule (10 mm inner diameter, 14 mm outer diameter, volume of ~13 cm^3) placed on the benchtop. This was followed by a mixture of 0.6468 g (3.575 mmol) Ta (Strem, 99.98%) and 1.1361 g (14.388 mmol) Se (Strem, 99.99%), gently pre-ground in an agate mortar; clean transfer was assisted by a glass funnel and anti-static brush. While submerged in an acetonitrile/dry ice bath, the ampule was evacuated four times with Ar backfilling on a Schlenk line before being sealed under vacuum. The ampule was placed in a two-zone horizontal tube furnace and the temperature was ramped over 6 h to establish a gradient of 590 °C (source zone) — 530 °C (growth zone). After maintaining this gradient for 240 h, the ampule was cooled to room temperature over 12 h. It was opened in an Ar-filled glovebox. This reaction provided 1.2604 g of gray, prismatic crystals (62.93 % isolated yield) recovered from the growth zone, which were subsequently stored within the glovebox. In this way, by using a
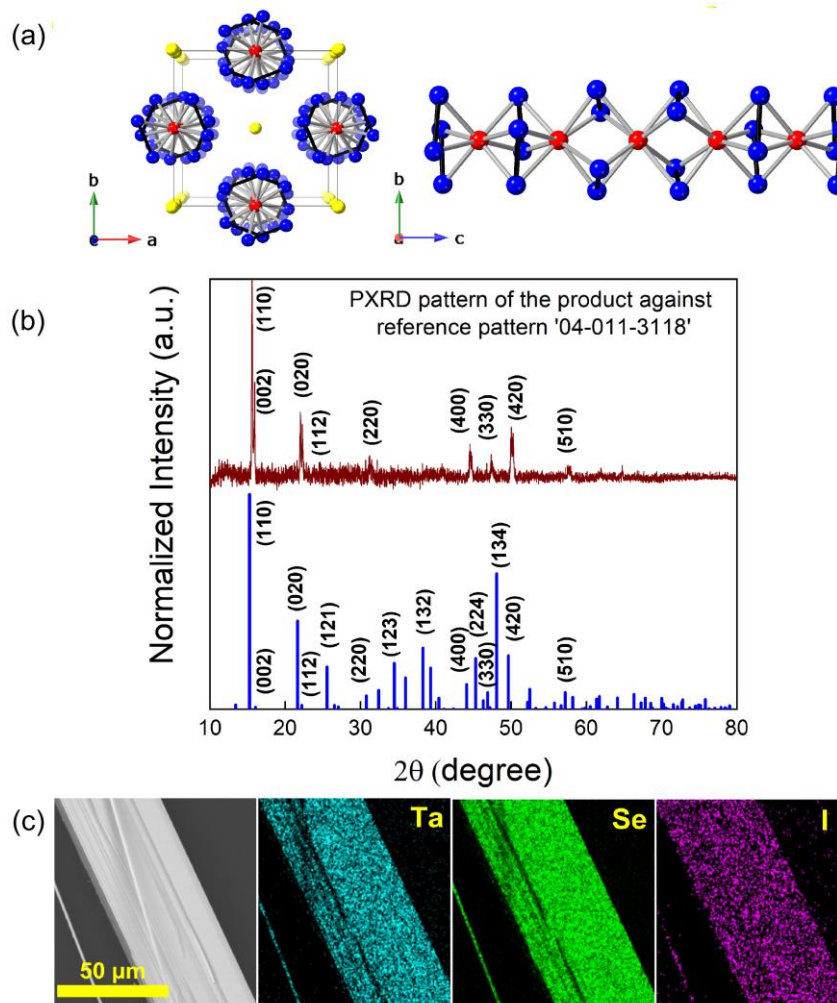
Figure 5-1: (a) Crystal structure of $(TaSe_4)_2I$ viewed down the *c*-axis (left panel) and *a*-axis (right panel), with atoms corresponding to Ta (red), Se (blue), and I (yellow). (b) Powder x-ray diffraction pattern of the CVT-grown crystals; experimental (top) and reference card 04-011-3118 (bottom pattern). (c) Scanning electron microscopy image of a mechanically exfoliated $(TaSe_4)_2I$ crystal surface and corresponding energy dispersive spectroscopy elemental mapping.

temperature gradient of 590–530 °C for 10 d, mm- to cm-sized $(TaSe_4)_2I$ crystals in good yield were produced [44, 45]. The quality of this material was examined using several methods (see Figure 5-1 (b-c)). Scanning electron microscopy (SEM) reveals features

exhibited by many 1D van der Waals materials, such as growth striations and facile cleavage along the van der Waals gap. Powder x-ray diffraction (XRD) confirms the expected structure of $(TaSe_4)_2I$. Energy dispersive x-ray spectroscopy (EDS) demonstrates homogeneity and provides a composition of $(TaSe_{3.4})_2I_{0.8}$; selenium and iodide deficiencies are well-known for metal chalcogenide compounds and expected here [46, 47]. The EDS data of the grown crystal is provided in table 5-1.

Table 5-1: EDS Characterization of the CVT-grown $(TaSe_4)_2I$ Crystal Samples

EDS Results				
	Ta at %	**Se at %**	**I at %**	**Formula** (normalized to Ta)
Theoretical	18.2	72.7	9.1	Ta_2Se_8I
Experimental (average of 14 areas across 5 crystals)	20.67	71.18	8.14	$Ta_2Se_{6.9}I_{0.8}$

5.3 Quasi 1D Nanoribbon Fabricated Devices

The quasi-1D nanoribbons of $(TaSe_4)_2I$ were prepared using a mechanical exfoliation technique on top of clean Si/SiO_2 substrates (University Wafer, p-type Si/SiO_2, <100>). Here, we use the term nanoribbon rather than nanowire to describe these structures owing to the fact that the width of the selected structures was substantially wider than the

thickness. This allowed for more accurate nanofabrication, testing, and comparison with quasi-2D materials. The exfoliated $(TaSe_4)_2I$ nanoribbons had a length of a few micrometers, a width on the scale of hundred nanometers, and a thickness in the range of 10 nm – 100 nm as confirmed by atomic force microscopy (AFM). The AFM images for two exfoliated nanoribbons with different thicknesses are shown in Figure 5-2 (a). A
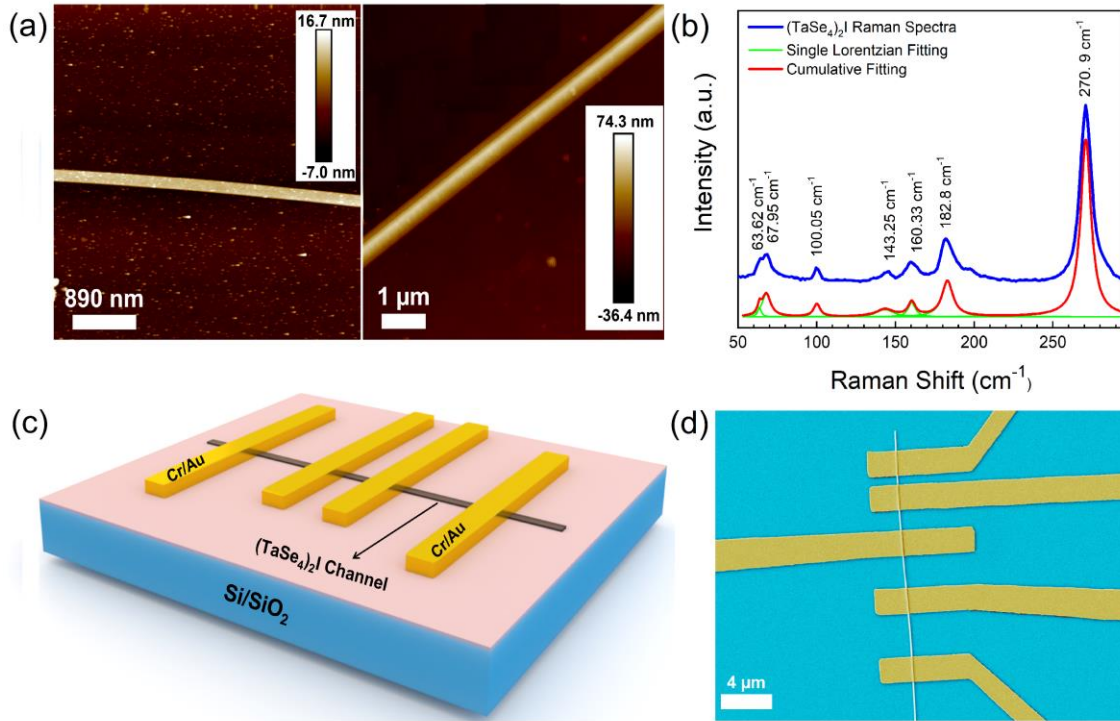
Figure 5-2: Characterization of the exfoliated quasi-one-dimensional $(TaSe_4)_2I$ nanoribbons. (a) Atomic force microscopy images of two exfoliated nanoribbons with different thicknesses and widths. The studied nanoribbons had thicknesses in the range of 10 nm to 100 nm. (b) Raman spectrum of a $(TaSe_4)_2I$ nanoribbon at room temperature. (c) Schematic of a $(TaSe_4)_2I$ nanoribbon test structure on Si/SiO_2 substrate. (d) Scanning electron microscopy image of a $(TaSe_4)_2I$ nanoribbon test structure with varying channel lengths from 1 µm to 4 µm. Pseudo-colors are used for clarity.

representative Raman spectrum of the exfoliated nanoribbons is provided in Figure 5-2 (b).

One can clearly see seven Raman peaks at the frequencies of 63.9 cm^{-1}, 67.9 cm^{-1}, 100.1

cm^{-1}, 143.3 cm^{-1}, 160.3 cm^{-1}, 182.8 cm^{-1}, and 270.9 cm^{-1}, in line with prior reports on bulk

$(TaSe_4)_2I$ crystals [48-51]. All observed Raman frequencies belong to the A_1 vibrational

mode type, except the peak at 67.9 cm^{-1} which belongs to the B_2 symmetry group [49]. The

test structures with multiple electrodes were prepared using electron-beam lithography

(EBL) to define the contacts on the same nanoribbon. Electron beam evaporation (EBE)

was used to deposit Cr/Au metals (10 nm / 100 nm) to form the contacts for measurements.

Figure 5-2 (c) shows a schematic diagram of the test structure, containing several metal

contacts and pads on the Si/SiO_2 substrate. The channel lengths of the individual devices,

i.e., the distance between two contacts, were in the range of 1 μm to 6 μm. The quality of

the contacts and the nanoribbon channels was verified with SEM. A colored SEM image

of a representative $(TaSe_4)_2I$ nanoribbon test structure is provided in Figure 5-2 (d).

5.4 Electrical and Noise Measurements of Nanoribbon Devices

The temperature-dependent current-voltage (I-V) measurements of the fabricated

nanoribbon test structures were carried out inside a cryogenic probe station (Lakeshore

TTPX) under vacuum using a semiconductor analyzer (Agilent B1500). The low-

frequency noise measurements were performed using an in-house built system. The noise

measurement circuit consists of a low-noise DC battery, a potentiometer (POT), and a

load resistor connected in series to the device under test (DUT) kept inside the probe

station chamber. The POT controls the voltage drops between the load and the DUT of the voltage divider noise circuit. The load resistor was kept grounded in this configuration. During the noise measurements, the voltage fluctuations at the output were transferred to a low noise preamplifier (SR-560) which amplified the signal and sent it to a signal analyzer. The signal analyzer transformed the time domain signal to its corresponding frequency domain. In our noise calculations, the voltage spectral density, S_V, was recalculated to its equivalent current spectral density, S_I, and normalized by the corresponding current squared, I^2. Further details of our noise measurement systems and procedures can be found in the in the prior reports for other materials and devices [39, 40, 52, 53].

To study the electrical characteristics of low-dimensional materials, which reveal phase transitions, it is important to verify the quality of the electrical contacts. Figure 5-3 (a) presents the low-bias I-V characteristics of one of the $(TaSe_4)_2I$ test structures for several channel lengths, *i.e.*, I-Vs measured between different pairs of contacts. The I-Vs show linear behavior across the measured bias ranges confirming high-quality Ohmic contacts. The contact resistance of $(TaSe_4)_2I$ nanoribbon was determined using the conventional transmission line measurement (TLM) technique (see Figure 5-3 (b). The contact resistance value for this representative device is $2R_C$=440 Ω, which is an order of magnitude lower than any of the channel resistances, R. The latter further confirms the quality of the fabricated contacts. The fact that R_C<<R is beneficial for the interpretation

84
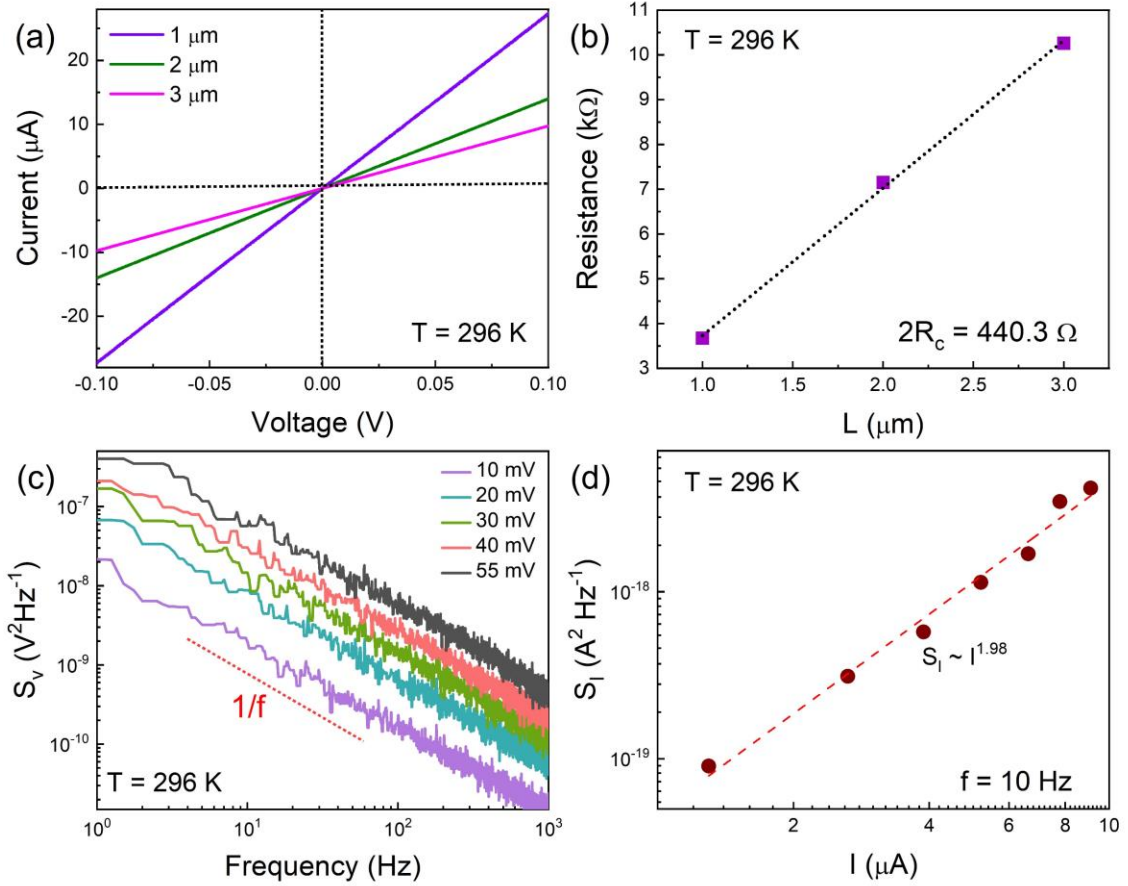
Figure 5-3: Electrical and low-frequency noise characteristics of a $(TaSe_4)_2I$ nanoribbons at room temperature. (a) Current-voltage characteristics for nanoribbon devices with different channel lengths. (b) Resistance of the nanoribbon devices as a function of the channel lengths. (c) Voltage noise spectral density, S_V, as a function of frequency for a $(TaSe_4)_2I$ nanoribbon device at different source-drain biases. (d) Current noise spectral density, S_I, as a function of the device current.

of the noise measurements as well.

The as-measured low-frequency voltage noise spectral density, S_V, is shown in Figure 5-3 (c). The room-temperature data are presented for a $(TaSe_4)_2I$ nanoribbon device with the 2-µm channel length measured for the source-drain bias, V_D, ranging from 10 mV to 60

mV. The noise spectra for all bias voltages are of $1/f^{\gamma}$ ($\gamma \approx 1$) flicker noise type, which is typical for both semiconductor and metallic materials [30, 38, 39, 54]. The noise levels measured at the lowest bias point is at least an order of magnitude higher than the background noise of the measurement system, confirming that the flicker $1/f$ noise is intrinsic to the DUT and not from any other source. The corresponding current spectral density, S_I, as a function of the source-drain current, I, at a fixed frequency of f=10 Hz is presented in Figure 5-3 (d). The S_I vs. I behavior is quadratic, *i.e.*, $S_I \sim I^2$, with the exact slope of 1.98. The quadratic scaling of the noise spectral density, S_I, with the source-drain current is expected for any linear resistor. Thus, we verified the accuracy of the noise measurement procedures and the fact that the $(TaSe_4)_2I$ nanoribbons act as passive linear resistors.

The temperature-dependent I-Vs and noise data for a $(TaSe_4)_2I$ device with a 2-μm channel length are presented in Figure 5-4 (a-d). Figure 5-4 (a) shows the device resistance in a logarithmic scale normalized by the resistance of the channel at 300 K, *i.e.* $log[R/R_{300}]$, as a function of the inverse temperature, *i.e.* $10^3/T$. The I-V measurements were conducted both in the heating and cooling cycles. Overall, the dependence of the $log[R/R_{300}]$ on inverse temperature is consistent with prior reports for bulk $(TaSe_4)_2I$ samples [4, 5, 8-13]. There is an abrupt change in the slope of the resistance below RT. This slope change is more clearly observed in the plot of the derivative characteristics presented in Figure 5-4 (b). In our case, we observed the transition at T=235 K for both cooling and heating cycle measurements. Previous reports attributed the change in the

resistivity slope to the Peierls transition, *i.e.*, CDW phase transition, observed mostly at T_P=260 - 263 K [4, 8, 9]. However, some reports indicated this transition at a temperature as low as T_P=235 - 240 K [55, 56]. It is known from experience with other CDW materials, that the temperature of the CDW phase transition may depend on the sample thickness [57, 58]. In addition, some data scatter for the transition temperature can be due to small stoichiometric variations, *e.g.*, the loss of iodine.

It has been stated that the Peierls transition in $(TaSe_4)_2I$ is accompanied by opening a CDW energy bandgap of ~0.2 eV [4, 12, 59, 60]. There is an unusual feature of the phase transition in $(TaSe_4)_2I$, which was noticed and discussed in the original studies of bulk crystals [8-10]. The material reveals a non-metallic *R(T)* dependence both below and *above T_P*. This issue was addressed in detail in a report that described $(TaSe_4)_2I$ as the zero-bandgap semiconductor and introduced a notion of the semiconductor-semiconductor phase transition [59]. In our measurements with $(TaSe_4)_2I$ nanoribbons, the resistance change near T_P is consistently observed but it is somewhat more gradual than in the case of bulk samples. We speculate that this can be related to the strain induced by the lattice mismatch between the material and Si/SiO_2 substrate. The latter is supported by our experiments with Al_2O_3 and other substrates and prior reports on the effect of the substrate-induced strain on resistive switching in nanowires [13, 61 - 63]. Based on the above considerations, we can conclude that our measured resistivity data are in line with previous reports [8-11, 13], and focus on the current fluctuations in $(TaSe_4)_2I$ nanoribbons.
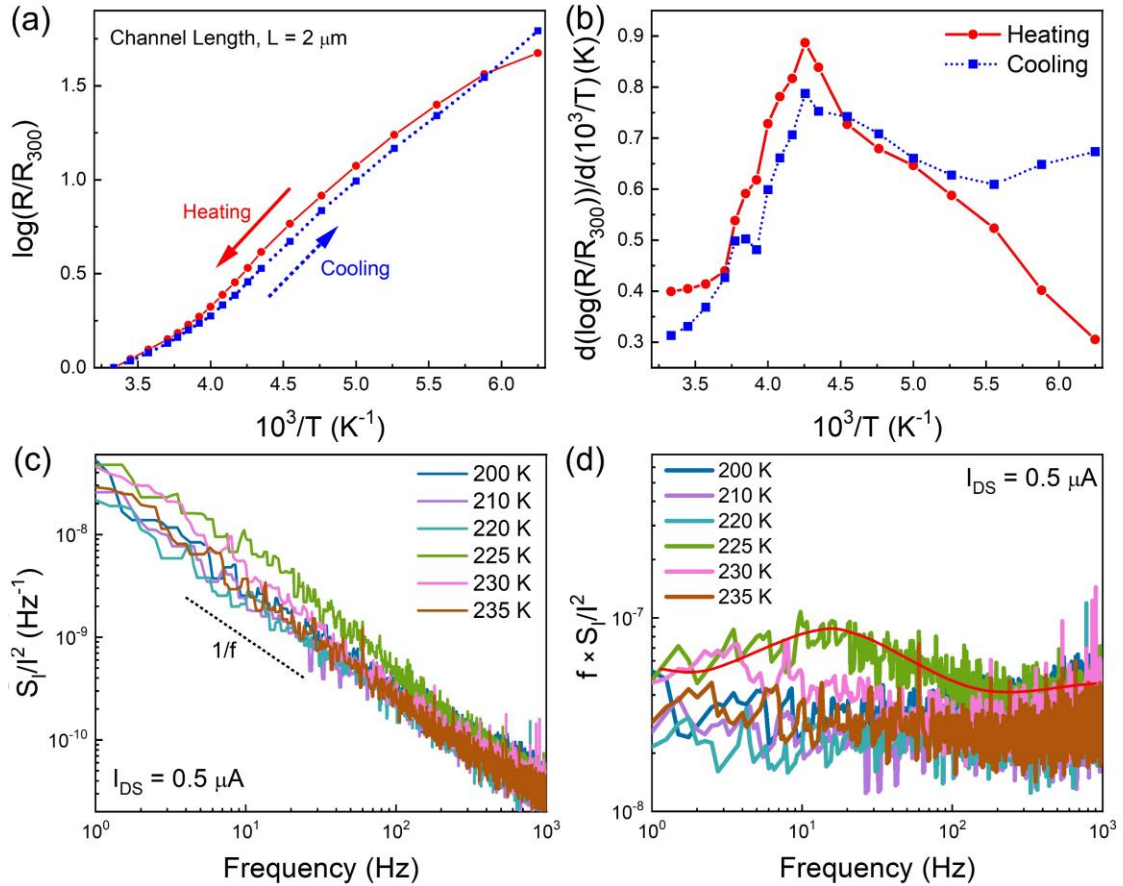
Figure 5-4: Temperature-dependent electrical and low-frequency noise characteristics of a $(TaSe_4)_2I$ nanoribbon device. (a) Logarithmic normalized resistance, $log([R/R_{300}]$, as a function of inverse temperature, $10^3/T$, for a $(TaSe_4)_2I$ nanoribbon device with a 2-µm channel length. (b) Logarithmic derivative, $d(log([R/R_{300}])/d(10^3/T)$, *vs* inverse temperature of the same device. (c) Normalized noise current spectral density, S_I/I^2, as a function of frequency at temperatures near the transition temperature measured at a constant device current of 0.5 µA. The noise behavior is of *1/f* type, except at $T \sim 225$ K, where the noise becomes Lorentzian type. (d) Normalized noise spectral density multiplied by the frequency, $f \times S_I/I^2$, as a function of frequency at different temperatures.

Figure 5-4 (c) shows the normalized noise current spectral density, S_I/I^2, as a function of frequency, f, at temperatures near T_P for the same device. The noise measurements were conducted between 200 K – 235 K to capture the Peierls transition from a possible change in the noise spectrum. One can notice an evolution of the $1/f$ spectrum to Lorentzian bulge near the Peierls transition temperature. To clarify the trend, we plotted $f \times S_I/I^2$ vs. f, which removes the $1/f$ background. One can see that at T=225 K, the noise spectral density reaches a maximum and develops a Lorentzian bulge. As the temperature increases further the noise becomes $1/f$ again, and its level decreases. We argue that the noise increase and Lorentzian feature are signatures of the Peierls transition, which we observed in the resistivity behavior in Figures 5-4 (a) and (b). The same trend – noise increases and Lorentzian – type bulges near the CDW phase transitions have been reported previously for different materials [36-39]. Some differences in temperature T_P extracted from the resistivity and noise data can be explained by a difference in the rate at which the temperature was changed in the probe station during these two independent measurements. In addition, there is a possibility of a temperature drift during the noise measurements. Generally, the Lorentzian noise spectrum is a signature of a two-level system [64, 65]. In the case of a phase transition, the material state and its resistance can switch between the two phases until the material system is driven further away from the transition point T_P. We observed a similar behavior in 1T-TaS$_2$, another CDW material [36, 37]. It is unlikely that the Lorentzian bulges which we see in the noise spectrum of (TaSe$_4$)$_2$I are due to the generation-recombination (G-R) noise that originates from high
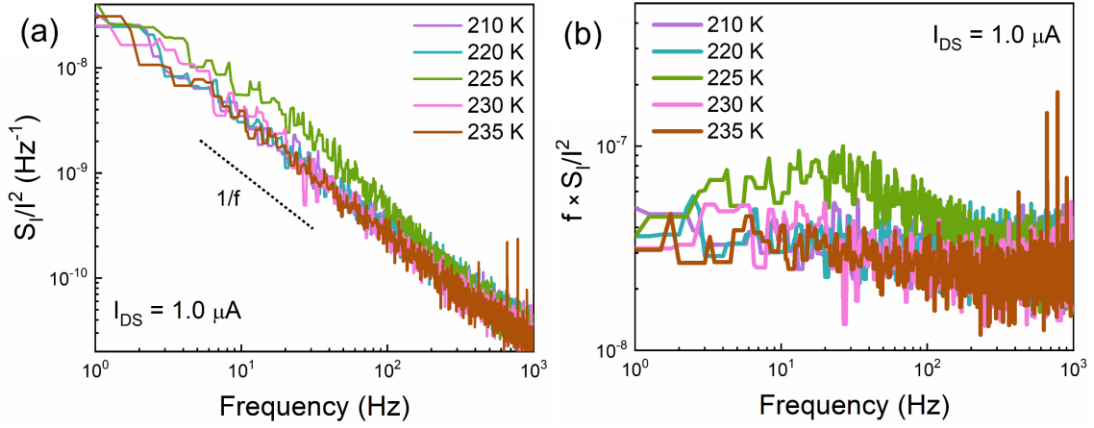
Figure 5-5: (a) Normalized noise current spectral density, S_I/I^2, as a function of frequency at temperatures near the transition temperature measured at another constant device current of 1.0 µA. The noise behavior shows *1/f* nature except at $T \sim 225$ K, where the noise is of Lorentzian type. (b) The normalized noise spectral density multiplied by the frequency, $f \times S_I/I^2$, as a function of frequency at different temperatures.

concentrations of one type of defects with particular time constants since it is observed only at one temperature and the noise spectrum returns to its original $1/f$ type. The noise behavior follows a similar trend range as measured at a different device current (refer to Figure 5-5(a-b)).

In Figure 5-6, we plot the noise spectral density normalized for the channel area, $\beta = S_I/I^2 \times (W \times L)$, at a fixed frequency $f = 10$ Hz and two representative values of the current. We have previously introduced the β parameter in order to compare low-frequency noise levels in two-dimensional (2D) materials such as graphene and MoS_2 [66, 67]. One can see that the noise spectral density increases by an order of magnitude near T_P proving that the noise level is a suitable indicator of the phase transition. Figure 6 attests to the low
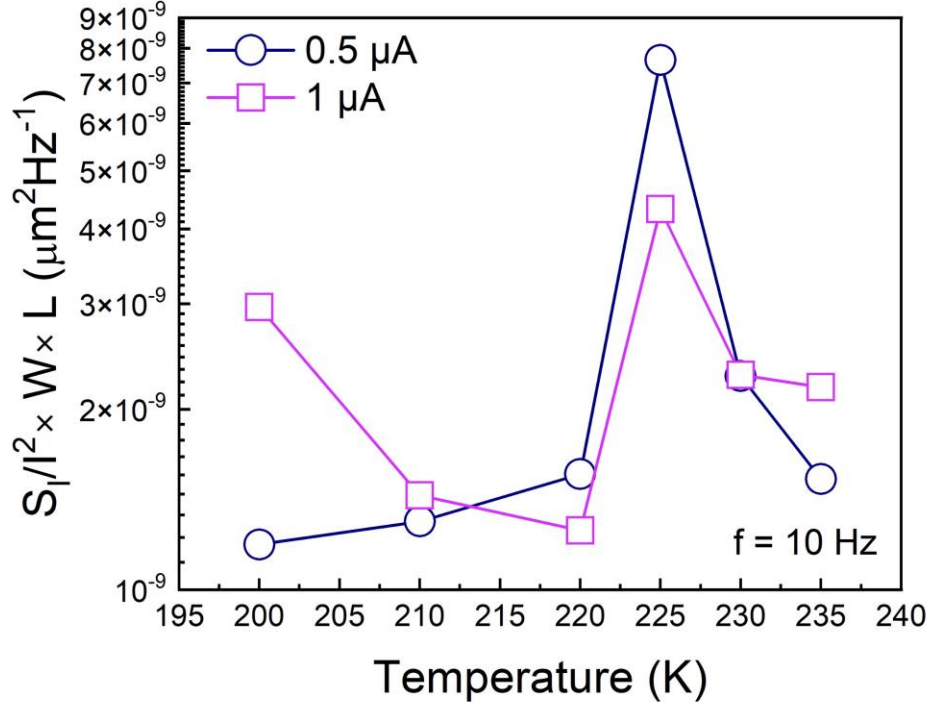
Figure 5-6: Evolution of the noise spectral density with temperature. The noise spectral density normalized by device current and channel area, $S_I/I^2 \times W \times L$, measured at $f = 10$ Hz, at the constant currents of $I_{DS} = 0.5\ \mu A$ and $1.0\ \mu A$. The noise level increases substantially near $T \sim 225$ K.

noise level, normalized by the channel area, compared to 2D materials. The nanoribbon shape of the $(TaSe_4)_2I$ channels, with the width much larger than the thickness, makes the comparison with 2D materials meaningful. The value of the β parameter away from the phase transition is below $2 \times 10^{-9}\ \mu m^2 Hz^{-1}$. For comparison, the area-normalized noise level in graphene is $\beta = 10^{-8}\ \mu m^2 Hz^{-1}$ while that in thin MoS_2 is $\beta = 10^{-5}\ \mu m^2 Hz^{-1}$ [60]. The noise level, S_I/I^2, without surface normalization, is also rather low, below $4 \times 10^{-9}\ Hz^{-1}$, away from the phase transition point, both in the low and high-temperature regions.

It is not possible to state at this point if the low level of the low-frequency noise in $(TaSe_4)_2I$ nanoribbons is due to the current fluctuation suppression in the topologically protected conductive channels of the Weyl semimetal [68, 69]. The latter would require a dedicated theoretical study allowing to connect the electron scattering and capture rates with the fluctuations in the number of electrons and their mobility. The experimental data reported in this study indicates an unexpectedly low noise level and motivates future studies. One should also note that the noise level measured in this Weyl semimetal nanoribbons is sufficiently low for interconnect applications. The resistivity extracted for these nanoribbons was similar to the values reported for bulk $(TaSe_4)_2I$, on the order of 10^{-3} Ω-cm [9, 11]. This material may not be the optimum one for interconnect applications in terms of its resistivity, but the low noise level for topological Weyl semimetals is a promising feature. It is known that low-frequency noise can be an early indicator of damage to materials and devices [70-73]. With the device degradation, the noise increases at a much faster rate than the changes in the averaged characteristics such as I-Vs. The latter makes the noise a sensitive predictor of a lifetime. The results obtained in this work can be used for developing assessment methodologies for the reliability of topological semimetals.

5.5 Conclusions

In conclusion, we describe low-frequency current fluctuations in quasi-1D (TaSe$_4$)$_2$I Weyl semimetal nanoribbons. The noise spectral density increases by almost an order of magnitude and develops Lorentzian features near the temperature $T \sim 225$ K. These spectral changes were attributed to the CDW phase transition even though the temperature of the noise maximum deviates from the reported Peierls transition temperature in bulk crystals. The noise level normalized to the device area in the Weyl semimetal nanowires is surprisingly low, $S_I/I^2 \times (W \times L) \sim 10^{-9}$ Hz^{-1} at f=10 Hz, when measured below and above the Peierls transition temperature. This value is an order of magnitude lower than that in graphene and other quasi-2D materials. These results shed light on the specifics of electron transport in quasi-1D topological Weyl semimetals and can be important for their proposed applications as downscaled interconnects.

References

1.   Y. Yuan, W. Wang, Y. Zhou, X. Chen, C. Gu, C. An, Y. Zhou, B. Zhang, C. Chen, R. Zhang, Z. Yang, *Advanced Electronic Materials* **2020**, *6*, 1901260.

2.   O. F. Shoron, M. Goyal, B. Guo, D. A. Kealhofer, T. Schumann, S. Stemmer, *Advanced Electronic Materials* **2020**, *6*, 2000676.

3.   I. D. Bernardo, J. Hellerstedt, C. Liu, G. Akhgar, W. Wu, S. A. Yang, D. Culcer, S. K. Mo, S. Adam, M. T. Edmonds, M. S. Fuhrer, *Advanced Materials* **2021**, *33*, 2005897.

4.   J. Gooth, B. Bradlyn, S. Honnali, C. Schindler, N. Kumar, J. Noky, Y. Qi, C. Shekhar, Y. Sun, Z. Wang, B. A. Bernevig, C. Felser, *Nature* **2019**, *575*, 315.

5.   A. A. Sinchenko, R. Ballou, J. E. Lorenzo, T. Grenet, P. Monceau, *Applied Physics Letters* **2022**, *120*, 063102.

6.   W. Shi, B. J. Wieder, H. L. Meyerheim, Y. Sun, Y. Zhang, Y. Li, L. Shen, Y. Qi, L. Yang, J. Jena, P. Werner, K. Koepernik, S. Parkin, Y. Chen, C. Felser, B. A. Bernevig, Z. Wang, *Nature Physics* **2021**, *17*, 381.

7.   T. Konstantinova, L. Wu, W. G. Yin, J. Tao, G. D. Gu, X. J. Wang, J. Yang, I. A. Zaliznyak, Y. Zhu, *npj Quantum Materials* **2020**, *5*, 1.

8.   M. Maki, M. Kaiser, A. Zettl, G. Grüner, *Solid State Communications* **1983**, *46*, 497.

9.   Z. Z. Wang, M. C. Saint-Lager, P. Monceau, M. Renard, P. Gressier, A. Meerschaut, L. Guemas, J. Rouxel, *Solid State Communications* **1983**, *46*, 325.

10.   H. Fujishita, M. Sato, S. Hoshino, *Solid State Communications* **1984**, *49*, 313.

11.   I. A. Cohn, S. G. Zybtsev, A. P. Orlov, S. v. Zaitsev-Zotov, *JETP Letters* **2020**, *112*, 88.

12.   X. P. Li, K. Deng, B. Fu, Y. K. Li, D. S. Ma, J. F. Han, J. Zhou, S. Zhou, Y. Yao, *Physical Review B* **2021**, *103*, L081402.

13.   Q. G. Mu, D. Nenno, Y. P. Qi, F. R. Fan, C. Pei, M. Elghazali, J. Gooth, C. Felser, P. Narang, S. Medvedev, *Physical Review Materials* **2021**, *5*, 084201.

14.   G. Grüner, *Reviews of Modern Physics* **1988**, *60*, 1129.

15. S. v Zaitsev-Zotov, *Physics-Uspekhi* **2004**, *47*, 533.

16. P. Monceau, *Advances in Physics* **2012**, *61*, 325.

17. A. A. Balandin, S. v. Zaitsev-Zotov, G. Grüner, *Applied Physics Letters* **2021**, *119*, 170401.

18. V. Favre-Nicolin, S. Bos, J. E. Lorenzo, J.-L. Hodeau, J.-F. Berar, P. Monceau, R. Currat, F. Levy, H. Berger, *APS* 2001, *87*, 015502.

19. Y. Shi, Q. Li, J. Yu, al -, S. Onishi, M. Jamei, A. Zettl -, S. van Smaalen, E. J. Lam, *Journal of Physics: Condensed Matter* 2001, *13*, 9923.

20. A. A. Balandin, F. Kargar, T. T. Salguero, R. K. Lake, *Materials Today* **2022**, *55*, 74.

21. Z. Chen, N. Boyajian, Z. Lin, R. T. Yin, S. N. Obaid, J. Tian, J. A. Brennan, S. W. Chen, A. N. Miniovich, L. Lin, Y. Qi, X. Liu, I. R. Efimov, L. Lu, *Advanced Materials Technologies* **2021**, *6*, 2100225.

22. A. Ruiz-Clavijo, O. Caballero-Calero, D. Navas, A. A. Ordoñez-Cencerrado, J. Blanco-Portals, F. Peiró, R. Sanz, M. Martín-González, *Advanced Electronic Materials* **2022**, 2200342.

23. W. Steinhögl, G. Schindler, G. Steinlesberger, M. Engelhardt, *Physical Review B* **2002**, *66*, 075414.

24. D. Josell, S. H. Brongersma, Z. Tokei, *Annual Review of Materials* **2009**, *39*, 231.

25. M. A. Stolyarov, G. Liu, M. A. Bloodgood, E. Aytan, C. Jiang, R. Samnakay, T. T. Salguero, D. L. Nika, S. L. Rumyantsev, M. S. Shur, K. N. Bozhilov, A. A. Balandin, *Nanoscale* **2016**, *8*, 15774.

26. T. A. Empante, A. Martinez, M. Wurch, Y. Zhu, A. K. Geremew, K. Yamaguchi, M. Isarraraz, S. Rumyantsev, E. J. Reed, A. A. Balandin, L. Bartels, *Nano Letters* **2019**, *19*, 4355.

27. C. Zhang, Z. Ni, J. Zhang, X. Yuan, Y. Liu, Y. Zou, Z. Liao, Y. Du, A. Narayan, H. Zhang, T. Gu, X. Zhu, L. Pi, S. Sanvito, X. Han, J. Zou, Y. Shi, X. Wan, S. Y. Savrasov, F. Xiu, *Nature Materials* **2019**, *18*, 482.

28. C. T. Chen, U. Bajpai, N. A. Lanzillo, C. H. Hsu, H. Lin, G. Liang, *Technical Digest - International Electron Devices Meeting, IEDM* **2020**, 32.4.1.

29. D. Gall, J. J. Cha, Z. Chen, H. J. Han, C. Hinkle, J. A. Robinson, R. Sundararaman, R. Torsi, *MRS Bulletin* **2021**, *46*, 959.

30. G. Liu, S. Rumyantsev, M. A. Bloodgood, T. T. Salguero, M. Shur, A. A. Balandin, *Nano Letters* **2017**, *17*, 377.

31. S. Beyne, K. Croes, I. de Wolf, Z. Tokei, *Journal of Applied Physics* **2016**, *119*, 184302.

32. T. M. Chen, A. M. Yassine, *IEEE Transactions on Electron Devices* **1994**, *41*, 2165.

33. B. Neri, A. Diligenti, P. E. Bagnoli, *IEEE Transactions on Electron Devices* **1987**, *34*, 2317.

34. P. Dutta, P. M. Horn, *Reviews of Modern Physics* **1981**, *53*, 497.

35. W. Yang, Z. Çelik-Butler, *Solid-State Electronics* **1991**, *34*, 911.

36. G. Liu, S. Rumyantsev, M. A. Bloodgood, T. T. Salguero, A. A. Balandin, *Nano Letters* **2018**, *18*, 3630.

37. R. Salgado, A. Mohammadzadeh, F. Kargar, A. Geremew, C. Y. Huang, M. A. Bloodgood, S. Rumyantsev, T. T. Salguero, A. A. Balandin, *Applied Physics Express* **2019**, *12*, 037001.

38. A. K. Geremew, S. Rumyantsev, F. Kargar, B. Debnath, A. Nosek, M. A. Bloodgood, M. Bockrath, T. T. Salguero, R. K. Lake, A. A. Balandin, *ACS Nano* **2019**, *13*, 7231.

39. S. Ghosh, F. Kargar, A. Mohammadzadeh, S. Rumyantsev, A. A. Balandin, *Advanced Electronic Materials* **2021**, *7*, 2100408.

40. S. Ghosh, K. Fu, F. Kargar, S. Rumyantsev, Y. Zhao, A. A. Balandin, *Applied Physics Letters* **2021**, *119*, 243505.

41. S. Ghosh, H. Surdi, F. Kargar, F. A. Koeck, S. Rumyantsev, S. Goodnick, R. J. Nemanich, A. A. Balandin, *Applied Physics Letters* **2022**, *120*, 062103.

42. R. Samnakay, A. A. Balandin, P. Srinivasan, *Solid-State Electronics* **2017**, *135*, 37.

43. P. Gressier, L. Guemas, A. Meerschaut, *Acta Cryst*. 1982, *38*, 2877.

44. P. Gressier, A. Meerschaut, L. Guemas, J. Rouxel, P. Monceau, *Journal of Solid State Chemistry* 1984, *51*, 141.

45. Y. Shi, Q. Li, J. Yu, al -, S. Onishi, M. Jamei, A. Zettl -, S. van Smaalen, E. J. Lam, Journal of Physics: Condensed Matter 2001, 13, 9923.I. Ohana, D. Schmeltzer, D. Shaltiel, Y. Yacoby, A. Mustachi, *Solid State Communications* **1985**, *54*, 747.

46. H. Yi, Z. Huang, W. Shi, L. Min, R. Wu, C. M. Polley, R. Zhang, Y. F. Zhao, L. J. Zhou, J. Adell, X. Gui, W. Xie, M. H. W. Chan, Z. Mao, Z. Wang, W. Wu, C. Z. Chang, *Physical Review Research* **2021**, *3*, 013271.

47. F. Kargar, A. Krayev, M. Wurch, Y. Ghafouri, T. Debnath, D. Wickramaratne, T. T. Salguero, R. K. Lake, L. Bartels, A. A. Balandin, *Nanoscale* **2022**, *14*, 6133.

48. I. Ohana, D. Schmeltzer, D. Shaltiel, Y. Yacoby, A. Mustachi, *Solid State Communications* **1985**, 54, 747.

49. A. Zwick, M. A. Renucci, P. Gressier, A. Meerschaut, *Solid State Communications* **1985**, *56*, 947.

50. S. Sugai, M. Sato, S. Kurihara, *Physical Review B* **1985**, *32*, 6809.

51. T. Sekine, T. Seino, M. Izumi, E. Matsuura, *Solid State Communications* **1985**, *53*, 767.

52. A. K. Geremew, S. Rumyantsev, M. A. Bloodgood, T. T. Salguero, A. A. Balandin, *Nanoscale* **2018**, *10*, 19749.

53. A. Geremew, C. Qian, A. Abelson, S. Rumyantsev, F. Kargar, M. Law, A. A. Balandin, *Nanoscale* **2019**, *11*, 20171.

54. A. A. Balandin, *Nature Nanotechnology* **2013**, *8*, 549.

55. S. M. Shapiro, M. Sato, S. Hoshino, *Journal of Physics C: Solid State Physics* **1986**, *19*, 3049.

56. M. Saint-Paul, P. Monceau, F. Lévy, *Solid State Communications* **1988**, *67*, 581.

57. P. Goli, J. Khan, D. Wickramaratne, R. K. Lake, A. A. Balandin, *Nano Letters* **2012**, *12*, 5941.

58. R. Samnakay, D. Wickramaratne, T. R. Pope, R. K. Lake, T. T. Salguero, A. A. Balandin, Nano Letters **2015**, *15*, 2965.

59. C. Tournier-Colletta, L. Moreschini, G. Autès, S. Moser, A. Crepaldi, H. Berger, A. L. Walter, K. S. Kim, A. Bostwick, P. Monceau, E. Rotenberg, O. v. Yazyev, M. Grioni, *Physical Review Letters* **2013**, *110*, 236401.

60. Z. Huang, H. Yi, L. Min, Z. Mao, C. Z. Chang, W. Wu, *Physical Review B* **2021**, *104*, 205138.

61. J. Wu, Q. Gu, B. S. Guiton, N. P. de Leon, L. Ouyang, H. Park, *Nano Letters* **2006**, *6*, 2313.

62. H. M. Lefcochilos-Fogelquist, O. R. Albertini, A. Y. Liu, *Physical Review B* **2019**, *99*, 174113.

63. M. K. Lin, J. A. Hlevyack, P. Chen, R. Y. Liu, S. K. Mo, T. C. Chiang, *Physical Review Letters* **2020**, *125*, 176405.

64. D. J. Ulness, A. C. Albrecht, *Physical Review A* **1996**, *53*, 1081.

65. T. Grasser, *Springer Nature* **2020**.

66. S. L. Rumyantsev, C. Jiang, R. Samnakay, M. S. Shur, A. A. Balandin, *IEEE Electron Device Letters* **2015**, *36*, 517.

67. M. A. Stolyarov, G. Liu, S. L. Rumyantsev, M. Shur, A. A. Balandin, *Applied Physics Letters* **2015**, *107*, 023106.

68. S. Y. Xu, N. Alidoust, I. Belopolski, Z. Yuan, G. Bian, T. R. Chang, H. Zheng, V. N. Strocov, D. S. Sanchez, G. Chang, C. Zhang, D. Mou, Y. Wu, L. Huang, C. C. Lee, S. M. Huang, B. Wang, A. Bansil, H. T. Jeng, T. Neupert, A. Kaminski, H. Lin, S. Jia, M. Z. Hasan, *Nature Physics* **2015**, *11*, 748.

69. M. Z. Hasan, G. Chang, I. Belopolski, G. Bian, S. Y. Xu, J. X. Yin, *Nature Reviews Materials* **2021**, *6*, 784.

70. L. K. J. Vandamme, *IEEE Transactions on Electron Devices* **1994**, *41*, 2176.

71. J. Xu, D. Abbott, Y. Dai, *Microelectronics Reliability* **2000**, *40*, 171.

72. Z. Gingl, C. Pennetta, L. B. Kiss, L. Reggiani, *Semiconductor Science and Technology* **1996**, *11*, 1770.

73. A. A. Balandin, *American Scientific Publishers* **2002**, 258.